Technical Physics Letters, Vol. 30, No. 1, 2004, pp. 1–3. Translated from Pis'ma v Zhurnal Tekhnicheskoĭ Fiziki, Vol. 30, No. 1, 2004, pp. 3–10.

The Effect of Fluctuations in the Lateral Period of a Multilayer Grating on the Scattering of Hard Synchrotron Radiation

V. I. Punegov

Syktyvkar State University, Syktyvkar, Komi Republic, Russia
e-mail: punegov@syktsu.ru

Received June 5, 2003

Abstract—The effect of fluctuations in the lateral period of a nonideal multilayer grating on the scattering of hard synchrotron radiation (X-ray frequency range) was studied. Maps of the angular distribution of the coherent and diffuse scattering intensity in the reciprocal space are constructed. Theoretical diffraction curves calculated for a Ni/C multilayer grating are compared to the experimental data obtained by high-resolution triple-axis diffractometry. It is shown that good agreement between theory and experiment is observed for a fluctuation dispersion within 3% of the average lateral period of the grating. *© 2004 MAIK "Nauka/Interperiodica".*

Increasing interest in multilayer gratings (MGs) is related to the possibility of using such gratings as dispersive elements for X-ray and near UV optics. Various theoretical methods and numerical codes have been developed for describing X-ray scattering from MGs (see, e.g., [1] and references therein). However, all these methods refer to the ideal lateral periodic structures. Unfortunately, existing technologies do not allow such perfect MGs to be obtained. Various disturbances in the MG structure introduce different peculiarities into the angular distribution of the scattered X-ray (synchrotron) radiation intensity.

Since MGs are based on a multilayer X-ray mirror, the structure under consideration is characterized by periodicity in both the vertical and lateral directions with the corresponding periods of d and T, respectively (Fig. 1). The effect of fluctuations in the vertical period d of semiconductor superlattices and multilayer X-ray mirrors on the formation of diffraction reflection curves was studied in [2–4]. To our knowledge, the influence of fluctuations in the lateral period T on the scattering of hard synchrotron radiation remains unstudied. This paper is aimed at filling that gap.

Let us consider the scattering of X-ray radiation from an MG representing a system of X-ray mirrors (laminar bars) periodic (quasiperiodic) in the lateral direction (Fig. 1). The grooves between laminar bars (grating lines) are usually obtained by methods of lithography or ion beam etching. Since none of the available methods allow perfect atomically smooth surface relief to be obtained, real MGs exhibit structural disturbances. These include roughness of the side walls of the laminar X-ray mirrors, random variations of the bar shape and dimensions from preset geometry, and fluctuations of the lateral grating period. The lateral size of the mirror (bar width) is determined as $l_x = \Gamma T$ ($0 < \Gamma < 1$), while $T(1 - \Gamma)$ is the spacing between bars (groove width). The diffraction reflection from such an MG takes place in the angular range of Bragg's reflection of the X-ray mirror.

Let A_n denote the amplitude of scattering from an arbitrary (nth) mirror in the grating structure. This amplitude can be calculated using the statistical dynamical theory of reflection from a multilayer X-ray mirror [5]. However, the aforementioned defects, as well as peculiarities in the internal structure of separate laminar bars (e.g., nonplanar layers, smeared interfaces, layer roughness, etc.), result in that the reflection efficiency may vary from one mirror to another. For this reason, the amplitude of a wave reflected from each multilayer mirror can be written as a sum of the average and fluctuating components: $A_n = \langle A \rangle + \delta A_n$, where $\langle \ldots \rangle$ denotes statistical averaging. We assume that the distance in the lateral direction from the first to the nth mirror is $\sum_{s=1}^{n-1} T_s$, where T_s is the fluctuating period

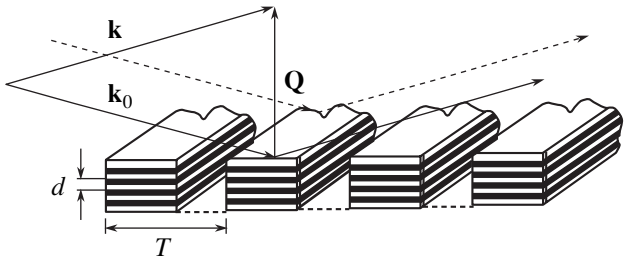

Fig. 1. Schematic diagram of the model MG structure and the synchrotron radiation scattering geometry: $\mathbf{k}_0$ and $\mathbf{k}$ are the wave vectors of the incident and diffracted waves; $\mathbf{Q}$ is the scattering vector.

1063-7850/04/3001-0001$26.00 © 2004 MAIK "Nauka/Interperiodica"

(a sum of the sth bar width and the spacing between sth and (s + 1)th bars). Denoting by $\langle T\rangle$ the average period of the MG under consideration, we can write $T_s = \langle T\rangle + \Delta T_s$, where ΔT_s are random deviations from the average period.

Theoretical description will be performed within the framework of the high-resolution triple-axis X-ray diffractometry. This method offers the most informative approach to the analysis of structural disorder. According to this, angular positions of the sample (ω) and analyzer (ε) relative to the Bragg angle ϑ_B are expressed in terms of the variables $q_x = \frac{2\pi}{\lambda}\sin(\vartheta_B)\{2\omega - \varepsilon\}$ and $q_z = -\frac{2\pi}{\lambda}\cos(\vartheta_B)\varepsilon$ in the reciprocal space. The intensity of scattering from an MG in the Fraunhofer approximation is expressed as

$$I_{\mathrm{MG}}(q_x, q_z) = \sum_{n=1}^{N}\sum_{m=1}^{N}(\langle A\rangle + \delta A_n)(\langle A^*\rangle + \delta A_m^*) \times \exp\left(iq_x\left(\sum_{s=1}^{n-1}T_s - \sum_{s=1}^{m-1}T_s\right)\right), \quad (1)$$

where N is the number of bars in the grating exposed to the incident X-ray beam.

We assume that fluctuations in the reflection efficiency and period of the grating are independent and can be averaged separately. Since $\langle \delta A_n\rangle = 0$ for any n, a solution of Eq. (1) can be represented as a sum of two terms:

$$I_{\mathrm{MG}}(q_x, q_z) = I^{(1)}_{\mathrm{MG}}(q_x, q_z) + I^{(2)}_{\mathrm{MG}}(q_x, q_z).$$

Here, the first term describes the coherent scattering of waves on a grating with the averaged diffraction efficiency of bars,

$$I^{(1)}_{\mathrm{MG}}(q_x, q_z) = |\langle A\rangle|^2\sum_{n=1}^{N}\sum_{m=1}^{N}\exp\left(iq_x\left(\sum_{s=1}^{n-1}T_s - \sum_{s=1}^{m-1}T_s\right)\right), \quad (2)$$

and the second term describes the incoherent (diffuse) scattering of waves on the grating, related to the aforementioned structural imperfections,

$$I^{(2)}_{\mathrm{MG}}(q_x, q_z) = \sum_{n=1}^{N}\sum_{m=1}^{N}\langle \delta A_n \delta A_m^*\rangle \exp\left(iq_x\left(\sum_{s=1}^{n-1}T_s - \sum_{s=1}^{m-1}T_s\right)\right). \quad (3)$$

Let $A = A(q_x, q_z)$ be the amplitude of scattering from a separate bar in the ideal MG structure, in which for any n the fluctuation is zero ($\delta A_n = 0$). Then, the amplitude of scattering from an "averaged" grating can be written in the form $\langle A\rangle = Af_{\mathrm{MG}}$, where f_{MG} is the statistical Debye–Waller factor of the MG. After simple transformations in expression (2), we obtain

$$I^{(1)}_{\mathrm{MG}}(q_x, q_z) = |A|^2 f^2_{\mathrm{MG}} \times\left\{N + 2\mathrm{Re}\left(\sum_{n=1}^{N}\sum_{m=1}^{n-1}\exp(-iq_x\langle T\rangle(n-m)) \times\exp\left(-\frac{q_x^2\sigma_T^2}{2}(n-m)\right)\right)\right\}, \quad (4)$$

where $\sigma_T = \sqrt{\langle \Delta T^2\rangle}$ is the variance of fluctuations in the lateral period T of the MG.

Let us consider the diffuse component of the intensity of scattering from the MG. Expression (3) can be transformed as follows:

$$I^{(2)}_{\mathrm{MG}}(q_x, q_z) = |\Delta A|^2(1 - f^2_{\mathrm{MG}})N \times\sum_{p=-\infty}^{\infty}G_p\exp(-iq_x\langle T\rangle p)\exp\left(-\frac{q_x^2\sigma_T^2}{2}p\right), \quad (5)$$

where G_p is the correlation function of the lateral periodicity and ΔA is the diffraction efficiency of the MG in the diffuse channel. For various diffraction conditions, this correlation function can either monotonically decrease with increasing p or exhibit periodic variations (with the period T).

The numerical modeling of X-ray scattering was performed for a Ni/C multilayer structure with the mirror period d = 4 nm and relative nickel layer thickness $d_{\mathrm{Ni}}/d = \gamma = 0.4$. The mirror height was l_z = 0.2 μm, which corresponded to 50 Ni/C bilayers. The MG period was T = 2 μm, the ratio of the average bar width l_x to the period was $\Gamma = l_x/T = 0.4$, and the total number of bars (i.e., grating lines) was N = 100.

The calculation was performed for X-ray radiation with a wavelength of 0.154 nm. The grating lines were X-ray mirrors with a perfect internal structure sharply bounded in the lateral direction. However, the cross-sectional shape and dimensions of the bars exhibited random deviations from the perfect relief, so that the static factor was $f_{\mathrm{MG}} = 0.7$.

The diffuse scattering was considered for a lateral-mosaic model. In contrast to the case of crystalline mosaicity [6], this model ignored angular disorientation of the mosaic blocks. The behavior of the correlation function depends on the cross-sectional dimensions of the bar and on the lateral period of the MG.

Figure 2 presents theoretical maps of the angular distribution of the intensity of scattering from the model MG and the diffraction curves simulated in the q_x scan mode for a grating with the ideal periodicity (Figs. 2a and 2c) and with a period fluctuating within σ_T = 0.1 μm (Figs. 2b and 2d). As can be seen, the pres-

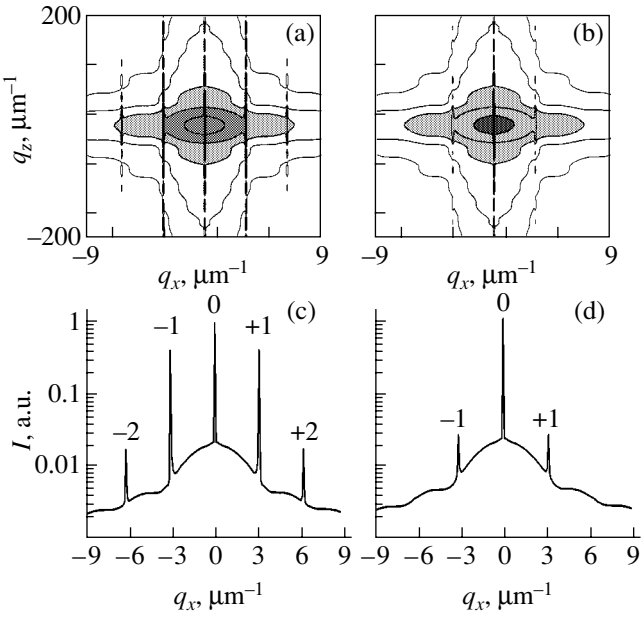

Fig. 2. The results of numerical modeling of the X-ray scattering from an MG (a, c) with the ideal period and (b, d) with a period fluctuating within $\sigma_T = 0.1$ μm.

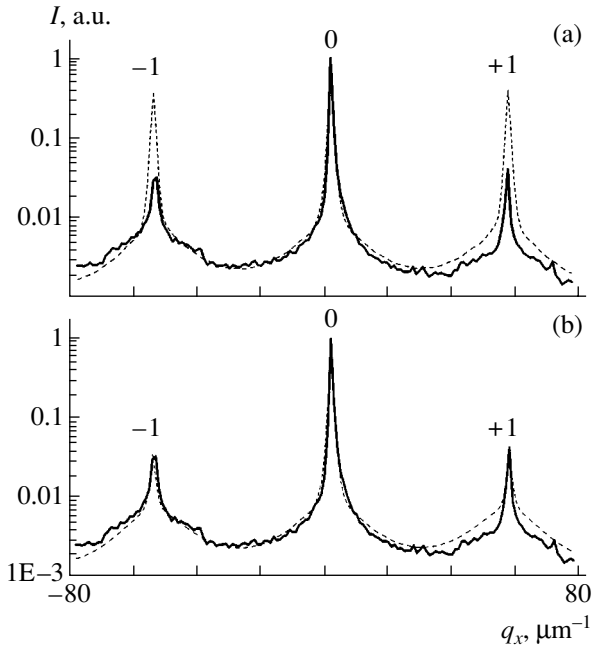

Fig. 3. A comparison between (solid line) the experimental diffraction curve and (dashed line) the results of theoretical calculations for the synchrotron radiation scattering in the q_x scan mode on a Ni/C multilayer grating with (a) the ideal and (b) a fluctuating lateral period.

ence of fluctuations leads to a decrease in the intensity of satellite peaks, leaving the main diffraction order peak intensity unchanged. For MG period fluctuations on the order of ten percent, $\sigma_T = 0.1\langle T\rangle = 0.2$ μm, the satellite structure almost completely disappears.

Figure 3 shows a comparison between the experimental scattering curve for the synchrotron radiation on a Ni/C multilayer grating and the results of theoretical calculations. The measurements were performed in a tricrystal diffraction scheme on a high-resolution diffractometer of the Anomalous Scattering SR Station of the VEPP-3 storage ring (Siberian SR Research Center, Budker Institute of Nuclear Physics, Novosibirsk). The experimental setup provided for an angular resolution of 18″ at a wavelength of 0.154 nm (8.048 keV). The average period of the laminar mirrors was $\langle d\rangle = 3.9$ nm, the relative nickel layer thickness was $\langle d_1\rangle/\langle d\rangle = \gamma = 0.37$, the MG period was $T = 0.8$ μm, and the total number of grating lines was $N = 35$.

In contrast to the model calculations described above, this calculation was performed for a periodic correlation function [7] because the diffuse scattering concentrates both in the region of the main peak and around the satellites (static factor, $f_{MG} = 0.7$; correlation length, $\tau_{MG} = 0.7$ μm). For the model of a lattice with the ideal periodicity, the theoretical curve significantly deviates from experimental data in the vicinity of satellite peaks (Fig. 3a). Allowance for the MG period fluctuations with a variance of $\sigma_T = 0.03\langle T\rangle = 0.024$ μm provides for satisfactory agreement between theory and experiment (Fig. 3b). Thus, a comparison of the calculated and measured intensities of the satellite peaks can serve as a diagnostic method for estimation of the lateral period fluctuations in multilayer gratings.

Acknowledgments. The author is grateful to S.V. Mytnichenko, N.V. Kovalenko, and V.A. Chernov (Siberian SR Research Center, Budker Institute of Nuclear Physics, Novosibirsk) for kindly providing the experimental data. Special thanks to S.V. Mytnichenko for fruitful discussions.

This study was supported in part by the Ministry of Education of the Russian Federation (project no. E02-3.4-302) and the Russian Foundation for Basic Research (project no. 03-02-16239).

REFERENCES

1. A. Sammar and J.-M. Andre, Opt. Commun. **149**, 348 (1998).
2. Ya. I. Nesterets and V. I. Punegov, Kristallografiya **44**, 980 (1999) [Crystallogr. Rep. **44**, 913 (1999)].
3. B. M. Clemens and J. G. Gay, Phys. Rev. B **35**, 9337 (1987).
4. A. V. Andreev and I. R. Prudnikov, Surf. Investig. **12**, 421 (1997).
5. V. I. Punegov, Poverkhnost': Rentgenovskie, Sinkhrotronnye, Neĭtronnye Issled., No. 2, 19 (2003).
6. Ya. I. Nesterets and V. I. Punegov, Acta Crystallogr. A **56**, 540 (2000).
7. Q. Shen, C. C. Umbach, B. Weselak, and J. M. Blakely, Phys. Rev. B **53**, R4237 (1996).

Translated by P. Pozdeev

Technical Physics Letters, Vol. 30, No. 1, 2004, pp. 12–14. Translated from Pis'ma v Zhurnal Tekhnicheskoĭ Fiziki, Vol. 30, No. 1, 2004, pp. 28–34.

Texture Formation on the Friction Surface in Transformation-Toughened Ceramics

P. V. Korolev, N. L. Savchenko, and S. N. Kul'kov*

Institute of Strength Physics and Materials Science, Siberian Division, Russian Academy of Sciences, Tomsk, 634055 Russia

** e-mail: kulkov@ms.tsc.ru*

Received June 24, 2003

Abstract—The surface of Y-TZP ceramics after dry friction on steel in a wide range of relative sliding velocities (0.2–11.1 m/s) was studied by X-ray diffraction. An analysis of the surface structure showed that the texture state of the friction surface is similar to that observed for analogous materials upon rough grinding. The main trends in the $I_{(002)}/I_{(200)}$ intensity ratio characterizing the tetragonal ZrO_2 phase as a function of the sliding velocity and the ceramic grain size are established. The mechanisms of lattice reorientation operative at various sliding velocities are discussed. © *2004 MAIK "Nauka/Interperiodica".*

High-strength yttria-stabilized tetragonal zirconia polycrystalline (Y-TZP) ceramics are promising materials for technological applications involving friction. The tribological properties and wear mechanisms of these ceramics have been extensively studied [1–6]. Realization of a particular mechanism of wear is determined by processes of the material surface straining under the conditions of friction. In this context, investigation into the mechanisms of surface straining during friction is very important, especially for Y-TZP ceramics susceptible to stress-induced structural transformations.

As is known, the stress-induced martensitic transformation from a metastable tetragonal (T) to the stable monoclinic (M) phase, on the one hand, and the twinning process, on the other hand, are the two competing mechanisms involved in Y-TZP material straining [7, 8]. At room temperature, the stress-induced T–M transformation is more probable. At elevated temperatures (where the thermodynamic stimuli for this transition are less effective), another mechanism of toughening, called ferroelasticity and based on the reorientation of coherent mechanical twins in the field of applied stresses, begins to operate [8]. The role of the T–M transformation in the wear of Y-TZP ceramics has already been generally established [1–3]. However, almost no data were reported concerning the mechanism of ferroelasticity in Y-TZP ceramics under the conditions of friction. This situation is probably explained by the fact that the main results were obtained for low-velocity friction, whereby the sliding velocities fall in the range from 0.01 to 1 m/s and the contact temperatures are relatively low. We believe that ferroelasticity manifestations have to be expected at elevated temperatures in the friction contact zone, in particular, under conditions of high-velocity or high-temperature friction.

Reorientation of the crystal lattice according to the mechanism of ferroelasticity is usually accompanied by the formation of a texture that can be revealed by X-ray diffraction [8, 9]. The texture is manifested by a change in the relative intensity of diffraction lines in the (002)–(200), (202)–(220), (113)–(311), (004)–(400), and other doublets of the T phase [8, 9]. Unfortunately, ferroelasticity of the T phase of zirconium dioxide is not the only factor responsible for the texture formation. For example, the grinding texture in Ce-TZP ceramics was explained [10] by reorientation of the crystal lattice due to a reversible martensitic transformation caused by the surface heating. According to Annamalai *et al.* [11], these two straining mechanisms can be distinguished by simultaneously monitoring the behavior of the M phase content on the friction surface and in the wear products, the latter usually occurring in the structural state realized on the friction surface at the moment of fracture.

This study was aimed at the X-ray diffraction analysis of the friction surface and wear products of Y-TZP ceramics after friction tests in a broad range of sliding velocities.

The experiments were performed on samples of Y-TZP ceramics with the composition 97 mol % ZrO_2 + 3 mol % Y_2O_3 obtained by sintering in vacuum at 1600 K for various times. Variation of the sintering time allowed the samples to be obtained with variable grain size and, hence, with different contributions of the transformation mechanism of toughening to the properties of ceramics [7]. In the initial (as-fired) state, all Y-TZP ceramics represented a mixture of tetragonal and cubic phases.

The friction tests were performed in a UMT-1 testing machine using the disk-on-rod scheme without lubricant, with stepwise increase in the relative veloc-

1063-7850/04/3001-0012$26.00 © 2004 MAIK "Nauka/Interperiodica"

ity. The counterbody was a disk, made of a cast high-speed steel (HRC 60), rotating in the vertical plane. The X-ray diffraction investigation of the wear products and the ceramic sample surface in the initial state and after friction testing was performed on a DRON-UM1 diffractometer using CuK_α radiation. The X-ray tube was operated at an accelerating voltage of 40 kV and a current of 22 μA. The measurements were performed in the angular interval $2\theta = 26°–38°$. The diffraction patterns were processed using the Renex program package (developed at the Institute of Strength Physics and Materials Science, Novosibirsk). We analyzed the relative intensities (I) of the (002) and (200) reflections corresponding to the tetragonal modification and determined the $I_{(002)}/I_{(200)}$ ratio for each friction regime. The content of a monoclinic phase on the friction surface was determined using the ratio of integral intensities of the {111} lines corresponding to the T and M phases [12].

The results of our investigation showed that a texture is formed on the Y-TZP sample surface upon friction in all regimes. The $I_{(002)}/I_{(200)}$ ratio upon friction is always greater than the initial value of about 0.5 corresponding to a random orientation of the crystal lattice on the polished surface before test (Fig. 1). The maximum value $I_{(002)}/I_{(200)} = 2.2$ was observed after friction at a sliding velocity of 0.2 m/s. As the velocity is increased to 0.9 m/s, the $I_{(002)}/I_{(200)}$ ratio significantly decreases but does not reach the initial level. Subsequent increase in the sliding velocity leads to new growth in the $I_{(002)}/I_{(200)}$ ratio up to a value of about 1.4 (Fig. 1). This behavior was observed for all samples irrespective of the initial grain size. In addition, the $I_{(002)}/I_{(200)}$ ratio exhibited an increase with the grain size (Fig. 2). These changes in the relative line intensities in the (002)–(200) doublets of the tetragonal phase upon friction indicate that the crystal lattice in most grains is oriented relative to the friction direction, so that the *c* axis is perpendicular to the friction surface. The X-ray diffractograms measured without sample rotation, under the conditions of beam diffraction along and across the friction direction, showed no differences in relative line intensities of the same doublet. This result indicates that the *a* and *b* axes are randomly oriented in the friction plane.

The amount of monoclinic phase in the wear products, as well as that on the friction surface, sharply decreases with an increase in the sliding velocity (see table). Above 3 m/s, no traces of the martensitic transformation (i.e., of the M phase) are found on the friction surface and in the wear products. In cases when the monoclinic phase is present, its amount is always higher in the wear products than on the friction surface (see table).

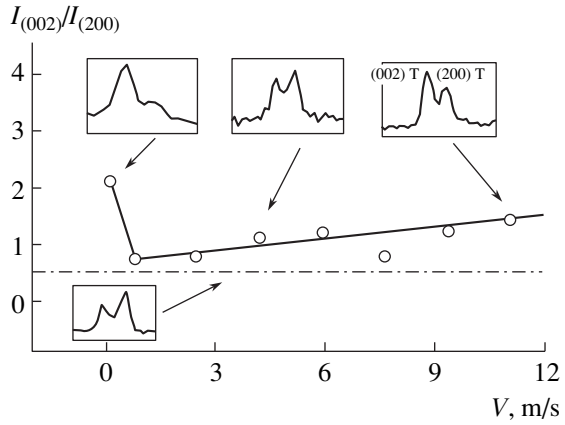

Fig. 1. Typical plot of the $I_{(002)}/I_{(200)}$ ratio versus sliding velocity for Y-TZP ceramics with an average grain size of 1.7 μm. The insets show the corresponding patterns X-ray diffraction patterns. The dashed line shows the $I_{(002)}/I_{(200)}$ ratio in the initial state (polished Y-TZP ceramics).

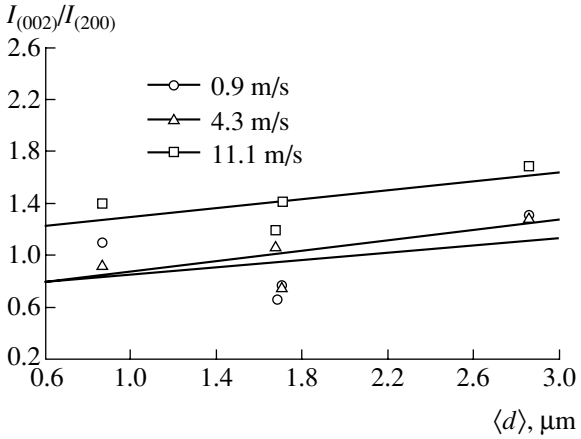

Fig. 2. Plots of the $I_{(002)}/I_{(200)}$ ratio versus grain size of Y-TZP ceramics friction tested at various sliding velocities.

During friction at a minimum sliding velocity, the temperature ion the friction contact zone and the lattice probably reoriented via the martensitic transformation. It appears, this process takes place during friction at

Content of the M phase (vol %) on the friction surface and in the wear products at various sliding velocities V in Y-TZP ceramics with an average grain size of 1.7 μm

	V, m/s							
	0.2	0.9	2.6	4.3	6	7.7	9.4	11.1
Friction surface	10	<5	0	0	0	0	0	0
Wear products	23	15	<5	0	0	0	0	0

0.2 m/s, as is indirectly confirmed by the X-ray diffraction data for the Y-TZP sample surface displaying the lines due to the M phase and showing the most pronounced inversion of the (002)–(200) peaks corresponding to the T phase (see Fig. 1 and the table). In this case, the irreversible oriented T–M transformation under the action of contact stresses is prevailing. As can be seen from data in the table, the martensitic transformation in the course of friction at a sliding velocity of 0.9 m/s becomes reversible to a considerable extent, which accounts for the decrease in the content of the M phase in the wear products and its almost complete absence on the friction surface. In this case, reorientation of the lattice can proceed by the following scheme: T–M (under the action of contact stresses) and M–T (under the action of heating).

Our estimates of the flash temperature according to [13] showed that, as the sliding velocity increases from 2.6 to 11.1 m/s, the contact temperature first increases to reach a temperature of stability of the tetragonal phase (>1000°C) and then grows within the limits of a two-phase tetragonal–cubic region on the phase diagram of the ZrO_2–Y_2O_3 system (1500–2000°C). In the latter temperature interval, reorientation of the lattice via martensite phase becomes impossible and, hence, the observed texture can form by the mechanism of ferroelasticity. In addition, it is well known that the force of resistance to the ferroelastic switching of domains in ferroelastic materials (analogous to the coercive force for ferromagnetic materials) usually decreases with increasing temperature in the interval below the critical temperature (an analog of the Curie temperature). In the case under consideration, the critical temperature is about 2100°C and corresponds to the temperature of transition to a single-phase cubic region [9]. Therefore, the observed increase in the $I_{(002)}/I_{(200)}$ ratio with the gliding velocity in the interval from 2.6 to 11.1 m/s (and, hence, with increasing temperature in the friction contact zone) can be due to an increase in the number of reoriented ferroelastic domains achieved at the expense of a decrease in the "coercive" force. Similar temperature dependences of the $I_{(002)}/I_{(200)}$ ratio were observed in the course of "hot" grinding of Y-TZP ceramics [9].

The increase in the $I_{(002)}/I_{(200)}$ ratio with the ceramic grain size observed during the tests at various velocities (Fig. 2) can also be explained within the framework of the above mechanism of texture formation. Apparently, there is a direct analogy with the well-known Hall–Petch relationship in strained polycrystalline materials, according to which the greater the grain size, the higher the mobility of dislocations. In our case, the grain size determines the mobility of martensite and twinned boundaries. Plastic straining via both the martensitic mechanism (based on the motion of martensite plates) and the mechanism of twin reorientation more readily proceeds in coarse-grained ceramics (Fig. 2). In the case of martensitic transformation, an increase in the degree of surface texturing with the grain size is also favored by the growing thermodynamic stimulus for the T–M transformation [7].

To summarize, we have demonstrated that reorientation of the crystal lattice of phases present in the surface layer of Y-TZP ceramics takes place in the entire range of sliding velocities in the friction contact. The observed texture is related to both the martensitic transformation and the ferroelastic switching of domains in the tetragonal phase. At high velocities and/or high contact temperatures, the martensitic mechanism can be excluded and only the ferroelastic mechanism is operative. At low velocities and/or low contact temperatures, the martensitic mechanism predominates, but the ferroelastic mechanism of the crystal lattice may contribute as well.

REFERENCES

1. T. E. Fischer, M. P. Anderson, and S. Jahanmir, J. Am. Ceram. Soc. **72**, 252 (1989).
2. Y. J. He, A. J. A. Winnubst, A. J. Burggraaf, *et al.*, J. Am. Ceram. Soc. **79**, 3090 (1996).
3. S. W. Lee, S. H. Hsu, and M. C. Shen, J. Am. Ceram. Soc. **76**, 1937 (1993).
4. Li Bo, Sun Yan, Wang Tianmin, *et al.*, J. Mater. Sci. Lett. **16**, 1333 (1997).
5. Sun Yan, Li Bo, De-Quan Yang, *et al.*, Wear **215**, 232 (1998).
6. N. L. Savchenko, P. V. Korolev, A. G. Mel'nikov, *et al.*, Trenie Iznos **22**, 322 (2001).
7. L. Nettleship and R. Stevens, Int. J. High Technol. Ceram. **3**, 1 (1987).
8. A. V. Virkar and R. L. K. Matsumoto, Adv. Ceram. **24**, 653 (1988).
9. K. Mehta, J. F. Jue, and A. V. Virkar, J. Am. Ceram. Soc. **73**, 1777 (1990).
10. M. V. Swain and R. H. J. Hannik, J. Am. Ceram. Soc. **72**, 1358 (1989).
11. V. E. Annamalai, T. Sornakumar, C. V. Gokularathnam, and R. Krishnamurthy, J. Am. Ceram. Soc. **75**, 2559 (1992).
12. R. C. Garvie and P. S. Nicholson, J. Am. Ceram. Soc. **55**, 303 (1972).
13. S. C. Lim and M. F. Ashby, Acta Metall. **35**, 1 (1987).

Translated by P. Pozdeev

Technical Physics Letters, Vol. 30, No. 1, 2004, pp. 15–18. Translated from Pis'ma v Zhurnal Tekhnicheskoĭ Fiziki, Vol. 30, No. 1, 2004, pp. 35–42.

Strongly Compensated InAs Obtained by Proton Irradiation

N. V. Zotova, S. A. Karandashev, B. A. Matveev*, M. A. Remennyĭ, N. M. Stus', N. A. Voronova, G. M. Gusinskiĭ, and V. O. Naĭdenov

Ioffe Physicotechnical Institute, Russian Academy of Sciences, St. Petersburg, 194021 Russia

**e-mail: bmat@iropt3.ioffe.rssi.ru*

Received June 19, 2003

Abstract—Proton irradiation of undoped *n*-InAs allowed a compensated material to be obtained with the degree of compensation $K \sim 0.6$. A regime of irradiation was selected to provide for a uniform distribution of radiation defects in depth of the semiconductor plate. The free electron density in irradiated InAs reaches up to 1×10^{18} cm^{-3}, which corresponds to the Fermi level fixed in the region of allowed states with a wave vector of $\kappa = 0$ in the conduction band (in contrast to other $A^{III}B^{V}$ semiconductor compounds, in which the Fermi level of a material with radiation defects occurs in the middle of the bandgap). The obtained results confirm the model of Brudnyi *et al.* [1]. © *2004 MAIK "Nauka/Interperiodica".*

Introduction. Semiconductor lasers, LEDs, and photodetectors operating in the middle IR spectral range have found wide application, for example, in gas sensors for detecting harmful industrial gases such as methane, hydrogen sulfide, carbon oxide and dioxide, etc. The most widely used semiconductor materials for these devices are indium arsenide (InAs) and related solid solutions. However, InAs (in contrast to other $A^{III}B^{V}$ semiconductor compounds) is still insufficiently studied as an object of irradiation.

According to some data [1–3], irradiation of InAs with protons, high-energy electrons, and neutrons leads to the formation of radiation defects of both donor and acceptor type. The density of these radiation defects depends on the Fermi level position in the initial material and on the regime of irradiation. The balance between charged defects of the donor and acceptor types leads to pinning of the Fermi level in the irradiated crystal. Recently [1], it was convincingly demonstrated that the Fermi level in irradiated InAs is shifted toward allowed states in the conduction band (in contrast to the situation in other $A^{III}B^{V}$ semiconductor compounds with radiation defects, in which the Fermi level is fixed in the middle of the bandgap). For this reason, the irradiation of InAs results in the formation of an n^+-type material.

It was established that the radiation defects formed in InAs represent deep strongly localized states situated in the middle of the bandgap. The bandgap width $\langle E_g \rangle$ in InAs, calculated as the energy difference between the conduction band bottom and the valence band top averaged over the entire Brillouin zone, amounts to ~1 eV [1]. The minimum bandgap width observed at Γ_{6C} for $\kappa = 0$ amounts (due to the presence of heavy In cations) to ~0.4 eV (at 77 K). Thus, the Fermi level in an irradiated crystal occurs above the conduction band bottom for $\kappa = 0$, falling in the interval of allowed states and accounting for the n^+ type of conductivity. It was shown that, when the Fermi level attains the limiting level, the densities of the radiation-induced donors and acceptors are close to each other and the irradiated crystal can be considered as a strongly compensated material.

The aim of this study was to obtain compensated InAs, required for applications in optoelectronics, by irradiating the initial material with protons. We have selected the regime of irradiation so as to provide for a uniform distribution of radiation defects in depth of the semiconductor plate. The results are used to verify a model according to which the Fermi level in the irradiated InAs is fixed in the region of allowed states with a wave vector of $\kappa = 0$ in the conduction band.

Method of proton irradiation. Radiation defects were introduced into InAs crystals by irradiating the samples with a beam of protons accelerated in the cyclotron of the Ioffe Physicotechnical Institute (St. Petersburg). As is well known, the density of radiation defects formed along a proton track in the target crystal gradually increases with decreasing energy of the penetrating particle, with a sharp increase at the end of the stopping range. For this reason, the task of obtaining a constant density of radiation defects through the entire target thickness (~100 μm) at a minimum level of induced radioactivity is by no means trivial. The problem is especially complicated when the irradiation is effected in cyclotrons, which are difficult to readjust with respect to the energy of accelerated particles.

1063-7850/04/3001-0015$26.00 © 2004 MAIK "Nauka/Interperiodica"

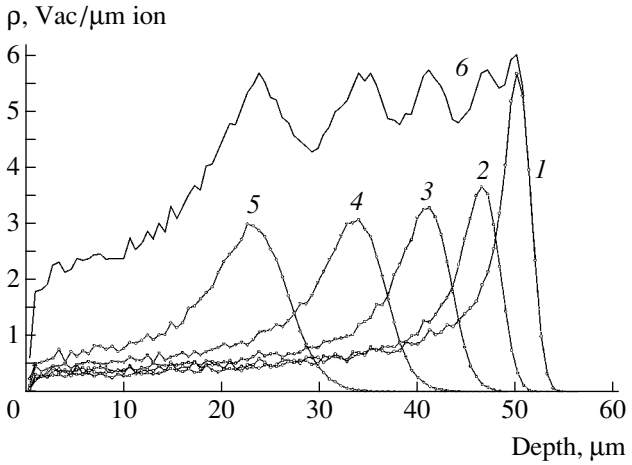

Fig. 1. Vacancy depth-concentration profiles in an *n*-InAs crystal upon irradiation with 2.8-MeV protons at various angles (SRIM code calculation): 0° (*1*), 22° (*2*); 35° (*3*); 47° (*4*); 61° (*5*). Curve *6* shows the total density of vacancies due to all exposures.

Calculations using the SRIM code showed that a 100-μm-thick InAs crystal irradiated from both sides with protons at a primary energy of E_p = 5 MeV (ion range, ~130 μm) is characterized by a virtually constant density of vacancies in depth of the sample. The Coulomb barrier for the proton irradiation of As and In nuclei is 6 and 8 MeV, respectively. However, the contribution due to the subbarrier reactions induced by 5-MeV protons on these nuclei is also significant, so that the samples irradiated to high doses have to be kept for up to half a year until the radioactivity will drop to a level acceptable for the measurement of parameters [1].

A significant decrease in the level of induced radioactivity upon irradiation can be provided by reducing the initial proton energy E_p. The results of calculations using the SRIM code for a 100-μm-thick InAs crystal irradiated from both sides show that a maximum density of vacancies (ρ_{max}) at a depth of 50 μm is reached at a primary proton energy of E_p = 2.8 MeV, the value of ρ_{max} being about 15 times the average vacancy density ρ obtained under the conditions used in [1].

In order to create a constant density of radiation defects in depth of the target, it is necessary to provide for the appropriate depth profile of ions with the range corresponding to ρ_{max}. This distribution was provided by varying the angle of irradiation α relative to the target surface normal. Figure 1 presents the initial fragment of calculation, with curves *1–5* showing the profiles of radiation defects calculated by the SRIM code for protons with a primary energy of 2.78 MeV incident at α = 0°, 22°, 35°, 47°, and 61°. This set of angles provides for the displacement of ρ_{max} in depth by the value equal to the full width at half maximum (FWHM) of the defect profile. The relative doses of radiation absorbed at these angles were calculated taking into account the contributions from vacancies created by all exposures at a given depth (Fig. 1, curve *6*). Further increase in the homogeneity of the distribution of radiation defects can be achieved by slightly varying the angles of exposure and increasing their number.

For creating a homogeneous density of defects in the entire sample cross section, 100-μm-thick plates were irradiated from two sides with protons at E_p = 2.8, 1.8, and 1.1 MeV with the corresponding angles and doses of exposure ensuring the formation of vacancies with a density of $\rho \simeq 18 \times 10^{19}$ cm^{-3}. According to these calculations, the density of radiation defects was homogeneous in depth to within ±10%. It should be noted that the method of irradiation considered above cannot provide for a highly homogeneous distribution of defects in the surface layers of the target without further decrease in E_p. In the case under consideration, the calculated density of defects within a depth of ≤4 μm amounted to ~60% of the value at greater depths. In order to increase the density of defects in the surface layers, the samples were additionally irradiated with protons at E_p = 1.1 MeV through an aluminum foil of appropriate thickness. For providing uniform irradiation of the sample area, the target was scanned with the proton beam in two directions. The beam current density did not exceed 10^{-7} A/cm^2. No induced radioactivity was detected in the targets upon exposure.

Sample characterization techniques. The proton-irradiated samples were characterized by galvanomagnetic techniques and photoluminescence (PL) spectroscopy. The Hall constant *R* and conductivity ω measured at 77 and 300 K were used to calculate the charge carrier density *n* and mobility μ.

The integral concentration of impurity ions (N_I), the densities of acceptors (N_A) and donors (N_D), and the

Table 1. Galvanomagnetic parameters of *n*-InAs before and after proton irradiation

	77 K				300 K			
	R, cm^3 s^{-1}	n, cm^{-3}	σ, Ω^{-1} cm^{-1}	μ, cm^2 V^{-1} s^{-1}	R, cm^3 s^{-1}	n, cm^{-3}	σ, Ω^{-1} cm^{-1}	μ, cm^2 V^{-1} s^{-1}
Initial crystal	–300.8	2.08×10^{16}	139.6	4.2×10^4	–273	2.3×10^{16}	83.2	2.27×10^4
Irradiated crystal	–5.45	1.0×10^{18}	560	3.0×10^3	–5.44	1.05×10^{18}	484	2.6×10^3

degree of compensation (K) were calculated by conventional methods using the formulas [4]

$$\begin{cases} N_{\rm I}^{77} = 2N_{\rm A} + n^{77} \\ N_{\rm I}^{300} = N_{\rm A} + n^{300} \end{cases}, \quad N_{\rm I}^{77} = \frac{\mu_{th}^{77}}{\mu_{\rm exp}^{77}} n^{77};$$

$$N_{\rm A} = \frac{N_{\rm I}^{77} - n^{77}}{2}; \quad N_{\rm D} = n^{300}; \quad K = \frac{N_{\rm A}}{N_{\rm D}}.$$

The PL spectra were excited by a GaAs laser (LPI-14, $\lambda = 0.9$ μm) and measured in the reflection mode with an InSb photodetector cooled to 77 K. The measurements were performed using an IKS-21 monochromator and a lock-in detection scheme.

Results and discussion. the initial material was undoped single crystal indium arsenide of the *n* type in the form of 100-μm-thick plates. The galvanomagnetic properties of the initial sample are presented in Table 1 in comparison to the characteristics of samples upon irradiation. Theoretical values of the electron mobility at 77 K, μ_{th}^{77} (for the scattering from impurity ions), were taken from [4].

As can be seen from the data in Table 1, the free electron density in the irradiated sample increases up to 1×10^{18} cm^{-3} (which corresponds to the Fermi energy ~490 meV at 77 K [5]), while the electron mobility decreases to 3000 cm^2/(V s). The integral impurity ion concentrations $N_{\rm I}$, the densities of acceptors ($N_{\rm A}$) and donors ($N_{\rm D}$), and the degree of compensation K determined as described in [4] are presented in Table 2. As expected according to the model proposed in [1], the proton irradiation results in a strong compensation of the material up to $K \sim 0.6$, whereby the Fermi level is fixed ~90 meV above the conduction band bottom.

Figure 2 shows the PL spectra of the InAs crystal before (curve *1*) and after (curve *2*) irradiation. In the initial material, the PL peak position (~408 meV, 77 K) and width (FWHM ~ 20 meV) correspond to direct transitions between the conduction band bottom and the valence band top at $\kappa = 0$ for an electron density of ~2×10^{16} cm^{-3} [5]. The pattern dramatically changes upon irradiation. The PL intensity exhibits a sharp drop, the position of the maximum significantly shifts toward shorter wavelengths (~490 meV), and the PL band width increases to reach FWHM ~ 90 meV. This is evidence of an increase in the free electron concentration (up to ~1×10^{-18} cm^{-3}), a degeneracy of the electron gas, and a shift of the Fermi level to ~90 meV above the conduction band bottom [5]. The decrease in the PL intensity is explained by the increase in the contribution of nonradiative recombination channels related to the appearance of radiation defects and the enhanced Auger recombination (caused by the growth in the free electron density).

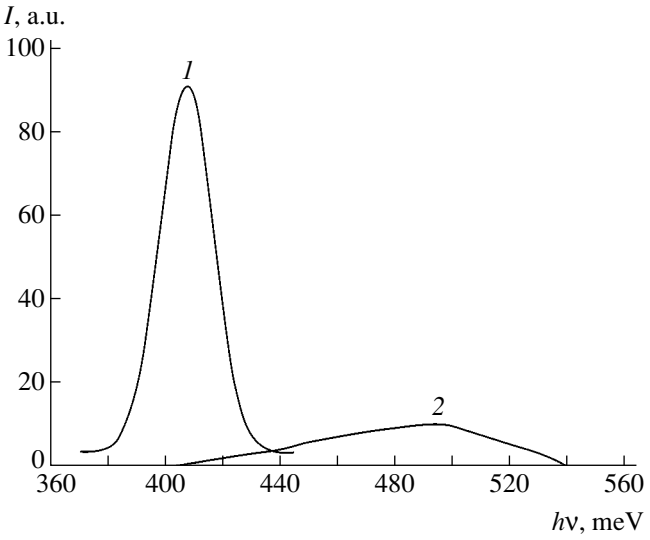

Fig. 2. PL spectra of the (*1*) initial and (*2*) proton-irradiated *n*-InAs crystals measured at 77 K.

The galvanomagnetic and luminescent properties of the irradiated crystal did not change in the course of layer-by-layer etching of the sample. This confirmed the homogeneity of the material along the entire sample plate thickness.

In conclusion, proton irradiation of the initial undoped *n*-InAs crystal allowed us to obtain a compensated material with a free electron density of ~1×10^{18} cm^{-3} and the degree of compensation $K = 0.6$. A specially selected regime of irradiation ensured homogeneous distribution of radiation defects in the sample cross section. The results confirmed a model of the Fermi level pinning in the region of allowed states with $\kappa = 0$ in the conduction band of InAs with radiation-induced defects.

Table 2. Experimental data on the integral impurity ion concentration ($N_{\rm I}$), the densities of acceptors ($N_{\rm A}$) and donors ($N_{\rm D}$), and the degree of compensation K for *n*-InAs crystals before and after proton irradiation

	$N_{\rm I}$, cm^{-3}	$N_{\rm A}$, cm^{-3}	$N_{\rm D}$, cm^{-3}	K
Initial crystal	3.47×10^{16}	6.9×10^{15}	2.99×10^{16}	0.23
Irradiated crystal	4.05×10^{18}	1.5×10^{18}	2.55×10^{18}	0.6

Acknowledgments. The authors are grateful to T.S. Lagunova for her help in conducting galvanomagnetic measurements.

This study was supported by the Ministry of Science and Technology of the Russian Federation within the framework of the Program "Development of the Basic Principles and Technology for the Creation of Novel Nanostructures for Electronics and Optoelectronics."

REFERENCES

1. V. N. Brudnyĭ, N. G. Kolin, and A. I. Potapov, Fiz. Tekh. Poluprovodn. (St. Petersburg) **37**, 408 (2003) [Semiconductors **37**, 390 (2003)].
2. N. G. Kolin, V. B. Osvenskiĭ, N. S. Rytova, and E. S. Yurova, Fiz. Tekh. Poluprovodn. (Leningrad) **21**, 521 (1987) [Sov. Phys. Semicond. **21**, 320 (1987)].
3. V. N. Brudnyi, S. A. Vorobiev, and A. A. Tsoi, Phys. Status Solidi A **72**, 529 (1982).
4. A. N. Baranov, T. I. Voronina, T. S. Lagunova, *et al.*, Fiz. Tekh. Poluprovodn. (St. Petersburg) **27**, 421 (1993) [Semiconductors **27**, 236 (1993)].
5. O. A. Allaberov, N. V. Zotova, D. N. Nasledov, and L. D. Neuĭmina, Fiz. Tekh. Poluprovodn. (Leningrad) **4**, 1936 (1970) [Sov. Phys. Semicond. **4**, 1659 (1970)].

Translated by P. Pozdeev

Technical Physics Letters, Vol. 30, No. 1, 2004, pp. 19–22. Translated from Pis'ma v Zhurnal Tekhnicheskoĭ Fiziki, Vol. 30, No. 1, 2004, pp. 43–50.

The Effect of a Space Charge on the Operation of a High-Power Semiconductor Current Interrupter

S. N. Rukin* and S. N. Tsyranov

Institute of Electrophysics, Ural Division, Russian Academy of Sciences, Yekaterinburg, Russia

** e-mail: rukin@iep.uran.ru*

Received June 11, 2003

Abstract—A theoretical model has been developed that describes operation of a high-power semiconductor current interrupter (SOS diode) with allowance for the space charge formation. According to this model, as well as to the models based on the quasineutral approximation, the process of current breakage in a semiconductor structure of the SOS diode is related to the formation of strong field regions in highly doped parts of the structure. The space charge decreases the role of avalanche multiplication, thus providing for higher switching characteristics of the diode. © *2004 MAIK "Nauka/Interperiodica".*

Introduction. The phenomenon of nanosecond breakage of a high-density current in semiconductors, known as the SOS effect, is observed in structures of the p^+–p–n–n^+ type for a pumping time on the order of 10^{-7}–10^{-6} s and a reverse current density of 1–60 kA/cm^2 [1]. The time of current breakage under these conditions falls within the interval from a few fractions of a nanosecond to dozens of nanoseconds. Special semiconductor current interrupters (SOS diodes) based on this effect are capable of switching pulsed signals on a gigawatt power level and can operate at voltages of up to 1 MV [2].

Theoretical investigations performed within the framework of the quasineutral approximation showed that the SOS effect is related to the formation of rapidly expanding strong field regions (SFRs) situated in highly doped parts of the semiconductor diode structure [3]. The quasineutral model also successfully explained the main parameters of the SOS effect [4–6]. However, this approximation fails to be valid in the regions of a strong gradient of the electric field. Such regions appear, in particular, in the stage of current breakage.

The aim of this study was to develop a refined model of the SOS effect taking into account the influence of a space charge and to use this model for description of the process of current breakage in an SOS diode structure. The results will be compared to those obtained using the quasineutral approximation.

Description of the model. A model taking into account the space charge was constructed by jointly solving the Kirchhoff equations, describing operation of an electric circuit with the SOS diode, and an equation describing the dynamics of electrons and holes in the diode structure. Calculations were conducted for an SOS diode comprising 160 serially connected unit elements, each with a thickness of W = 320 μm and an area of S = 0.36 cm^2. The base was n-Si with an initial carrier density of 10^{14} cm^{-3}; the p^+ region was formed by boron diffusion (impurity density, 10^{21} cm^{-3}, penetration depth, 85 μm); the p region was obtained by aluminum diffusion (10^{17} cm^{-3}, 165 μm); and the n^+ region was obtained by phosphorus diffusion (5×10^{19} cm^{-3}; 90 μm).

The scheme of pumping is described elsewhere [4]. After switching on the direct pump capacitor, a dc current of up to 300 A passed through the SOS diode elements over a time period of 355 ns. During the subsequent switching on of the reverse pump capacitor, the system conducted a reverse current that increased to 1.5 kA within a time period of 35 ns (by the moment of current breakage).

The dynamics of electrons and holes in the SOS diode structure was calculated using a basic system of equations including the equations of continuity for electrons and holes and the Poisson equation for the electric field:

$$\frac{\partial n}{\partial t} = \frac{1}{e}\frac{\partial J_n}{\partial x} + GR, \quad \frac{\partial p}{\partial t} = -\frac{1}{e}\frac{\partial J_p}{\partial x} + GR,$$

$$J_n = eD_n\frac{\partial n}{\partial x} + eV_n(E)n, \quad J_p = -eD_p\frac{\partial p}{\partial x} + eV_p(E)p, \quad (1)$$

$$\frac{\partial E}{\partial x} = \frac{e}{\varepsilon}[p(x) - n(x) + N_d(x) - N_a(x)].$$

Here, n and p are the densities, V_n and V_p are the velocities, J_n and J_p are the component current densities, and D_n and D_p are the diffusion coefficients of electrons and

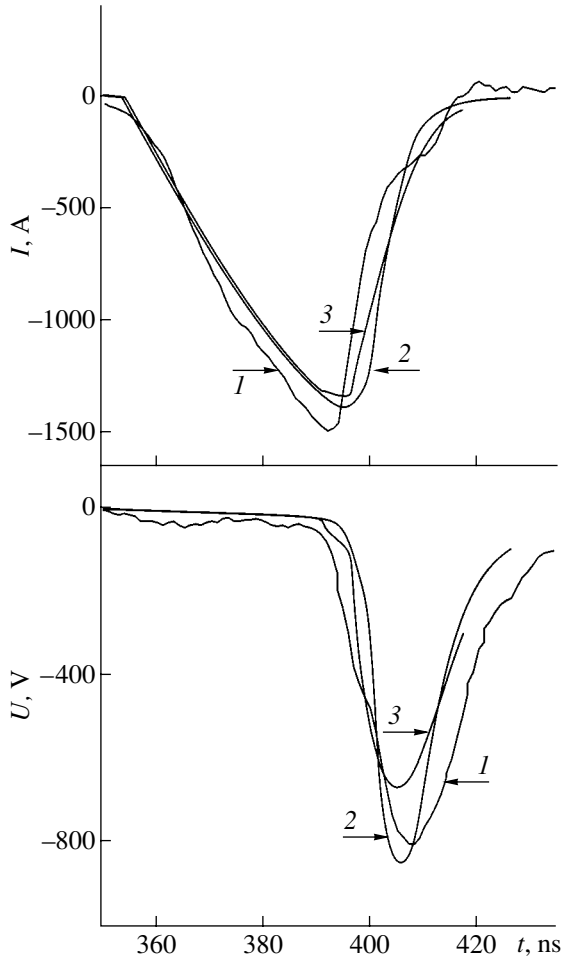

Fig. 1. Time variation of the current and voltage in the SOS diode structure in the stage of current breakage: (*1*) experiment; (*2*) calculation using the model taking into account the space charge formation; (*3*) calculation in the quasineutral approximation.

holes, respectively; N_d and N_a are the donor and acceptor concentrations, respectively; E is the electric field strength; GR is the term describing the bulk rate of the electron–hole pair generation and recombination; and e is the electron charge. The kinetic coefficients for Eq. (1) were taken from [4]. The boundary conditions were selected in the following form:

$$\begin{aligned} x = 0: &\quad J_p = J, \quad J_n = 0, \quad E = 0, \\ x = W: &\quad J_p = 0, \quad J_n = J. \end{aligned} \tag{2}$$

By jointly solving equations describing the conditions of equilibrium ($np = N_i^2$) and quasineutrality ($n - N_d = p - N_a$), it is possible to determine the initial distribution of the electron and hole densities. For numerical solution, system (1) was transformed as follows. First, the quantities J_n and J_p were replaced by their discrete analogs using an exponential approximation suggested in [7]. This substitution renders the numerical scheme unconditionally monotonic. Then, the system was linearized and a linear system of algebraic equations was written with respect to small increments in the electron and hole densities and in the electric field strength. This system was solved by the method of matrix trials. Calculations in the quasineutral approximation were performed using a model described in [3].

Results and discussion. Analysis of the results of numerical calculations showed the following. In the stage of direct pumping, the curves of the current passing through the SOS diode and the voltage drop across the diode obtained in the model taking into account the space charge virtually coincide with the results of calculations according to the quasineutral model, both models fitting to the experimental dependences. In the initial stage of the *p*–*n* junction filling with charge carriers, the charge density distributions predicted by the two models differ slightly. However, this period is very short (the *p*–*n* junction is completely filled with charge carriers 0.5 ns after the onset of direct pumping) and the differences vanish within 1 ns.

A significant difference between the two models is manifested only in the stage of current breakage (Fig. 1). According to the model taking into account the space charge, as well as to the quasineutral approximation, the process of current breakage in a semiconductor structure of the SOS diode is related to the formation of SFRs in highly doped *p*- and *n*-type parts of the structure. The SFR formation begins at the moment when the major carrier velocities in the regions outside the plasma concentration fronts exhibit saturation: $J = eN_aV_{ps}$ (in the *p*-type region) and $J = eN_dV_{ns}$ (in the *n*-type region), where J is the current density and V_{ns} and V_{ps} are the saturation velocities of electrons and holes, respectively. As the concentration fronts move toward the *p*–*n* junction, the SFRs expand, the voltage drop across the structure increases, and the current accordingly decreases. In both models, the SFR in the *p* region possesses a greater (more than threefold) expansion velocity and features a higher (one and a half times) electric field strength than does the SFR in the *n* region. As a result, the main (up to 82%) voltage drop in the SOS diode structure in the stage of current breakage takes place in the *p* region.

However, the SFR dynamics in the *p* region in the model taking into account the space charge differs from that according to the quasineutral model, which accounts for the different characteristics of current breakage. The maximum difference in the distribution of excess hole density and the electric field strength is reached at the moment of maximum voltage drop across the structure, which corresponds to the maximum SFR size: 40 and 32 μm for the model taking into account the space charge and the quasineutral model, respectively (Fig. 2).

In the quasineutral model, the current passage after saturation of the major carrier velocity outside the concentration fronts requires excess carriers that can appear only as a result of avalanche multiplication. This factor leads to the formation of SFRs in which the field strength is determined by the density of excess carriers necessary for the current passage [4].

A different situation takes place in the model taking into account the space charge formation. As long as the electric field strength outside the concentration front is small (below 10^4 V/cm), the major carrier density smoothly decreases from maximum (at the front) to equilibrium (corresponding to the classical regime of operation of a high-current diode [8]). When the major carrier velocities in the regions outside the concentration front (where $E \sim 3 \times 10^4$ V/cm) exhibit saturation, the major carrier density reaches a constant level determined by the formulas $p = J/(eV_{ps})$ and $n = J/(eV_{ns})$ for the p and n regions, respectively. The field strength distribution is determined, according to the Poisson equation, by the difference between the major carrier density and the impurity concentration. As the concentration front moves toward the p–n junction, the SFR expands and, hence, the electric field strength increases until reaching a level sufficient for the onset of avalanche multiplication (~2×10^5 V/cm in the p region and ~1.4×10^5 V/cm in the n region). By this time, the SFR width reaches 20 μm and 6 μm in the p and n regions, respectively, and the voltage across the diode structure is 530 V.

Then, avalanche multiplication takes place in the region of maximum field strength, where the electron–hole pairs are generated and dissociated. The rate of SFR expansion in the p region is proportional to the concentration front velocity. This velocity can be expressed as [4]

$$V_p = \frac{J}{e\Delta p}\left(\frac{b}{b+1} - \frac{J_n}{J}\right), \quad (3)$$

where Δp is the excess hole density in the concentration front, J_n is the electron current density in the SFR, and $b \sim 3$ is the ratio of electron and hole mobilities. As can be seen from formula (3), the electron current induces retardation of the concentration front. The J_n/J ratio reaches 0.2 in the model taking into account the space charge and 0.4 in the quasineutral model. For the same Δp, this implies that the concentration front velocity in the p region in the former model is 1.5 times that in the latter case. The higher velocity of the concentration front decreases the time of the SFR formation in the model taking into account the space charge and increases the maximum width of this region (40 versus 32 μm) and the maximum voltage drop across the structure (847 versus 667 V), thus resulting in a greater rate of current breakage (1.38×10^{11} versus 0.9×10^{11} A/s) as compared to the quasineutral approximation.

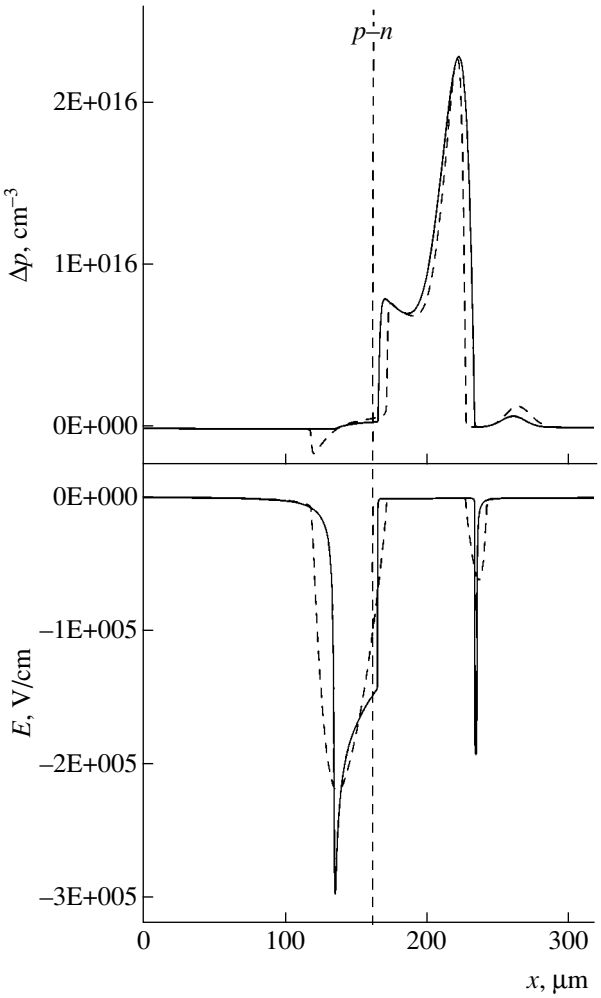

Fig. 2. Excess hole density (Δp) distributions and the electric field strength (E) profiles in the SOS diode structure at the moment of maximum voltage drop across the diode, calculated using the model taking into account the space charge formation (dashed curves) and in the quasineutral approximation (solid curves).

Conclusions. Our analysis of the results of modeling showed that (i) the current breakage both in the model taking into account the space charge and in the quasineutral approximation is related to the formation of strong field regions in highly doped p- and n-type parts of the structure and (ii) the dynamics of excess carriers in the SFR according to these models is different. The presence of a distributed space charge decreases the role of avalanche multiplication, thus providing for the higher commutation characteristics: the rate of current switching grows and the voltage drop increases.

REFERENCES

1. S. N. Rukin, Prib. Tekh. Éksp., No. 4, 5 (1999).
2. S. A. Darznek, S. K. Lyubutin, S. N. Rukin, *et al.*, Élektrotekhnika, No. 4, 20 (1999).
3. S. A. Darznek, G. A. Mesyats, and S. N. Rukin, Zh. Tekh. Fiz. **67** (10), 64 (1997) [Tech. Phys. **42**, 1170 (1997)].
4. S. A. Darznek, S. N. Rukin, and S. N. Tsyranov, Zh. Tekh. Fiz. **70** (4), 56 (2000) [Tech. Phys. **45**, 436 (2000)].
5. S. N. Rukin and S. N. Tsyranov, Pis'ma Zh. Tekh. Fiz. **26** (18), 41 (2000) [Tech. Phys. Lett. **26**, 824 (2000)].
6. A. V. Ponomarev, S. N. Rukin, and S. N. Tsyranov, Pis'ma Zh. Tekh. Fiz. **27** (20), 29 (2001) [Tech. Phys. Lett. **27**, 857 (2001)].
7. D. L. Scharfetter and H. K. Gummel, IEEE Trans. Electron Devices **ED-16**, 64 (1969).
8. H. Benda and E. Spenke, Proc. IEEE **55**, 1331 (1967).

Translated by P. Pozdeev

Technical Physics Letters, Vol. 30, No. 1, 2004, pp. 23–25. Translated from Pis'ma v Zhurnal Tekhnicheskoĭ Fiziki, Vol. 30, No. 1, 2004, pp. 51–55.

An Analysis of the Equilibrium Configurations of Charged Cylindrical Jets of a Conducting Liquid

N. M. Zubarev and O. V. Zubareva

Institute of Electrophysics, Ural Division, Russian Academy of Sciences, Yekaterinburg, Russia

e-mail: nick@ami.uran.ru

Received June 2, 2003

Abstract—A region of physical parameters is found where the equilibrium configurations of charged cylindrical jets of a conducting liquid can exist; these configurations correspond to the azimuthal mode $n = 2$ of the surface deformations of a round jet. A critical value of the jet linear charge is determined for which the jet splits into two. It is shown that such instability is excited in a soft regime. *© 2004 MAIK "Nauka/Interperiodica".*

Jets are known to be unstable with respect to small perturbations of the surface because of the development of the Rayleigh instability caused by capillary effects. For charged jets, electrostatic forces are an additional factor that determines the system behavior. In this paper, we restrict our consideration to the azimuthal perturbation modes of the jet surface. In this case, the instability is induced by Coulomb forces, while capillary forces play a stabilizing role. In order to understand the main laws governing the behavior of a charged jet, we should determine conditions when the mutual compensation of these forces is possible, as well as the conditions when such compensation is principally impossible. In other words, we should determine the region of existence of stable solutions for the problem of the equilibrium configurations of charged jets of a conducting liquid.

In previous papers [1, 2], exact solutions of the problem were found for an arbitrary azimuthal mode number n and various possible stationary profiles of the charged surface of a conducting liquid in the plane geometry. It should be noted that a mathematically similar problem related to an analysis of the stationary profile of a two-dimensional air bubble in the ideal liquid was independently solved for $n = 2$ [3] and $n = 3, 4, 5 \ldots$ [4]. All the cited papers gave expressions for the surface shape only in terms of quadratures. For this reason, it is impossible to analyze the solutions in detail, in particular, to formulate the conditions of the jet (or bubble [3, 4]) splitting. In order to study the properties of solutions more effectively, it is necessary to transform them to a more suitable form, that is, to express them in terms of elementary functions. In this paper, the corresponding expressions are presented and analyzed for the simple case when the deformation of a round jet is related to the excitation of a large-scale azimuthal mode with $n = 2$.

Let us write the equations of electrostatics that describe a stationary profile of the jet surface in a conducting liquid for the problem of plane symmetry, when the cross section of the jet is constant in the direction of motion. The two-dimensional Laplace equation

$$\varphi_{xx} + \varphi_{yy} = 0$$

determines the distribution of the electric field potential φ over the jet cross section plane $\{x, y\}$. This equation should be solved together with the equipotential condition $\varphi = 0$ on the conductor surface. Another boundary condition is that the field of the charged conductor should coincide at infinity with the field of a uniformly charged filament:

$$\varphi \longrightarrow -Q\ln(x^2 + y^2), \quad x^2 + y^2 \longrightarrow \infty,$$

where Q is the specific linear electric charge density of the conductor. The equilibrium surface relief is determined by the balance condition for the forces acting on the charged surface of a conducting liquid,

$$(8\pi)^{-1}(\nabla\varphi)^2_{\varphi = 0} + \alpha K + p = 0,$$

where the first term describes the electrostatic pressure on the liquid boundary and the second term describes the surface pressure (α is the surface tension coefficient and K is the local curvature of the surface). The constant p is expressed in terms of the jet velocity (v), liquid density (ρ), and external (p_e) and internal (p_i) pressures:

$$p = p_i - p_e - \rho v^2/2.$$

The integral relations obtained in [1, 2] make it possible to find the solution to the above equations in terms of the elementary functions. In the most important case of $n = 2$ (corresponding to a minimum value of the

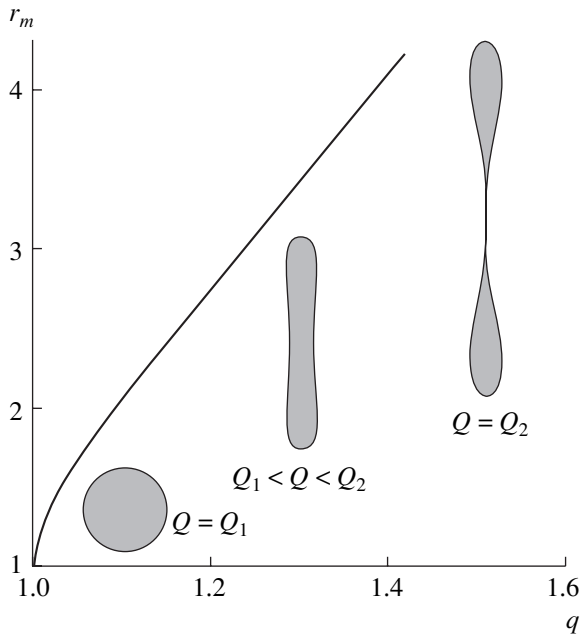

The dependence of the maximum distance between the jet axis and its surface r_m (the radius of the unperturbed jet is normalized to unity) on the reduced charge $q = Q/Q_1$. The insets show the cross sections of the charged jet in a conducting liquid for $l = l_1 = 2$, $l = 1.9$, and $l = l_2 \approx 1.86$.

charge Q required to induce a linear instability of the round jet), we arrive at the following parametric equations for the jet configurations:

$$y = \frac{Q^2}{2\pi\alpha} \times \frac{(9\sqrt{4-l^2} + 2\sqrt{3}(4-l))\cos\psi + \sqrt{4-l^2}\cos(3\psi)}{\sqrt{3}(l-1)(4+l+\sqrt{3(4-l^2)}\cos(2\psi))}, \quad (1)$$

$$x = \frac{Q^2}{2\pi\alpha} \times \frac{(9\sqrt{4-l^2} - 2\sqrt{3}(4-l))\sin\psi - \sqrt{4-l^2}\sin(3\psi)}{\sqrt{3}(l-1)(4+l+\sqrt{3(4-l^2)}\cos(2\psi))}, \quad (2)$$

where $l = (1 - 2Q^2p/(\pi\alpha^2))^{1/2}$; the closed surface corresponds to the change of the parameter ψ by 2π. To the best of our knowledge, such solutions have not been obtained and studied so far.

Let us consider conditions for the jet splitting. For $l = l_1 = 2$, expressions (1) and (2) determine circles, which corresponds to the unperturbed state of the jet, namely, to the jet with a round cross section. With decreasing l, the jet is deformed. At a certain value l_2 of the parameter l, the volume occupied by the jet loses connectivity and splits into two (see figure). The value l_2 is determined by the condition of the surface self-intersection: $x = 0$ at $\psi = \pi/2$, which gives $l_2 = 13/7$.

Let us determine the values of the charge for a jet with the given cross section area S, which correspond to the threshold values of the auxiliary parameter l (l_1 and l_2). Using the Green's formula, the area can be expressed as

$$S = \int_0^\pi (y_\psi x - x_\psi y)d\psi = \frac{Q^4(l^2+2l-7)}{\pi\alpha^2(l^2-1)^2}.$$

Solving this relation with respect to Q, we arrive at the dependence of the charge on the surface tension α, area S, and parameter l:

$$Q = \left[\frac{\pi\alpha^2 S(l^2-1)^2}{l^2+2l-7}\right]^{1/4}. \quad (3)$$

In the problem under consideration, we can define two critical charge values. The first critical value corresponds to $l = l_1 = 2$ in formula (3):

$$Q_1 = (9\pi\alpha^2 S)^{1/4} \approx 2.31\alpha^{1/2}S^{1/4}.$$

If the linear charge Q of the jet exceeds this value, the jet with the round cross section becomes unstable with respect to surface perturbations corresponding to the azimuthal mode with $n = 2$. The second critical charge value corresponds to $l = l_2 = 13/7$, for which formula (3) yields

$$Q_2 = (1800\pi\alpha^2 S/49)^{1/4} \approx 3.28\alpha^{1/2}S^{1/4}.$$

For this charge, the jet splits into two. This means that solutions described by expressions (1) and (2) exist only under the condition that $Q_1 \le Q \le Q_2$.

Let us study the regime of excitation of the instability, which results in the jet splitting. For this purpose, it is convenient to consider the dependence of the jet surface perturbation amplitude on the charge The reduced charge q is defined as the ratio of the charge Q to the first critical value:

$$q = \frac{Q}{Q_1} = \left[\frac{(l^2-1)^2}{9(l^2+2l-7)}\right]^{1/4}. \quad (4)$$

The dimensionless perturbation amplitude of the jet boundary is defined as the ratio of the maximum distance between the jet axis and its surface to the unperturbed jet radius $\sqrt{S/\pi}$:

$$r_m = \frac{2\sqrt{4-l^2} + \sqrt{3}(l-1)}{\sqrt{3}(l^2+2l-7)}. \quad (5)$$

The value of r_m as a function of the reduced charge q, determined parametrically by Eqs. (4) and (5), is pre-

sented in the figure. As can be seen from this plot, the perturbation amplitude monotonically increases with the charge. Such a dependence of the perturbation amplitude on the control parameter (electric charge) indicates that the azimuthal mode $n = 2$ of the surface perturbation of the cylindrical jet with a round cross section is excited in a soft regime. As a result, the solutions considered above can be stable with respect to perturbations that do not violate the problem symmetry.

Acknowledgments. This study was supported by the Ural Branch of the Russian Academy of Sciences, the Foundation for Support of Russian Science, the "Dynasty" Foundation, and the International Center for Basic Physics (Moscow).

REFERENCES

1. N. M. Zubarev, Pis'ma Zh. Tekh. Fiz. **25** (23), 55 (1999) [Tech. Phys. Lett. **25**, 950 (1999)].
2. N. M. Zubarev, Zh. Éksp. Teor. Fiz. **116**, 1990 (1999) [JETP **89**, 1078 (1999)].
3. D. Crowdy, Phys. Fluids **11**, 2836 (1999).
4. R. Wegmann and D. Crowdy, Nonlinearity **13**, 2131 (2000).

Translated by M. Kobrinskiĭ

Technical Physics Letters, Vol. 30, No. 1, 2004, pp. 26–29. Translated from Pis'ma v Zhurnal Tekhnicheskoĭ Fiziki, Vol. 30, No. 1, 2004, pp. 56–64.

The Main Feature of the Guide Structures Described by Non-Self-Conjugate Electrodynamic Operators

A. S. Raevskiĭ, S. B. Raevskiĭ, and A. A. Titarenko

Nizhni Novgorod State Technical University, Nizhni Novgorod, Russia

e-mail: raevsky@nntu.sci-nnov.ru

Received June 18, 2003

Abstract—A solution of the boundary problem for a two-layer round shielded waveguide leads to the conclusion that the main feature of the guide structures described by the non-self-conjugate operators is the mandatory presence of complex waves in their spectra. The pair excitation of these waves results in the appearance of the complex resonance phenomenon. *© 2004 MAIK "Nauka/Interperiodica".*

A homogeneous boundary value problem is formulated as the *n*th-order differential equation

$$L(u) = \sum_{\nu=0}^{n} f_\nu u^{(\nu)} = 0 \quad (1)$$

with the set of boundary conditions

$$U_m = 0; \quad m = 1, 2, \ldots, N. \quad (2)$$

The conjugate boundary value problem is written [1] as the differential equation

$$L^*(u) = \sum_{\nu=0}^{n} (-1)^\nu (f_\nu u)^{(\nu)} = 0 \quad (3)$$

with the corresponding set of boundary conditions

$$U_k = 0; \quad k = 1.2, \ldots, N^*, \quad N^* = 2qn - N, \quad (4)$$

where the domain of definition of the function U is divided into q intervals [2].

A homogeneous boundary value problem describing a guide structure is formulated in terms of an electrodynamic operator. Problems of the type (1), (2) are usually obtained upon separating variables in the general boundary value problem based on the Helmholtz equation. According to [1], an operator is self-conjugate if and only if it originates from the corresponding self-conjugate differential equation with self-conjugate boundary conditions. Accordingly, a boundary value problem is self-conjugate only when two conditions are satisfied: (i) $L(u) = L^*(u)$ and (ii) the boundary conditions (2) and (4) are equivalent.

When the field in a nondissipative guide structure is described by a homogeneous Helmholtz equation (i.e., by an even-order equation), the first self-conjugation condition is usually satisfied. The second condition is satisfied [2, 3] only when $N^* = N$. Therefore, the inequality

$$N^* \neq N \quad (5)$$

can be considered as a sufficient condition for the electrodynamic operator to be non-self-conjugate.

The eigenvalues of the non-self-conjugate boundary value problems in the general case are known [1] to be complex values. As a result, the spectra of the guide structures described by non-self-conjugate boundary value problems contain complex waves (CWs) [2–4]—that is, the waves with complex wavenumbers—even despite the absence of energy dissipation in the media forming these structures. It was shown rather long ago [5] that such complex waves exist in a two-layer round shielded waveguide with $\varepsilon_1/\varepsilon_2 > 1$, where $\varepsilon_{1,2}$ are the permittivities of the internal and the external layers, respectively. Until now, it was believed [2] that the character of the diffraction phenomena resulting in the appearance of opposite power fluxes in a two-layer waveguide, which provide for the existence of CWs, prevents their existence for $\varepsilon_1/\varepsilon_2 < 1$. This assumption contradicts the notion that the eigenvalues of the non-self-conjugate boundary problems (in the case under consideration, the boundary value problem for hybrid waves is non-self-conjugate for any ε_1 and ε_2) are, in the general case, complex values.

Detailed numerical investigations performed recently showed that the CWs in a two-layer round shielded waveguide can also exist at $\varepsilon_2 > \varepsilon_1$, which is in agreement with the general statements of the theory of linear differential operators [1].

Figure 1 shows the dispersion characteristics of the waves HE_{11}, EH_{11}, and HE_{12} in a waveguide with the relative permittivity $\tilde{\varepsilon} = \varepsilon_2/\varepsilon_1 = 90$, obtained as solutions of the dispersion equation for the waves in the

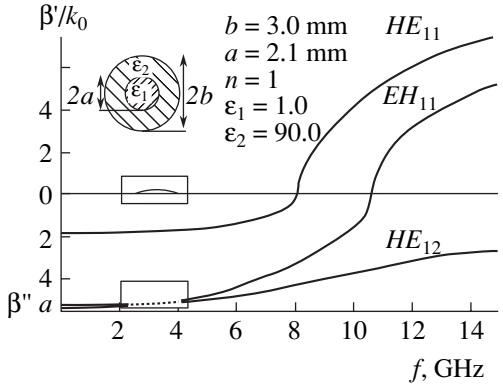

Fig. 1. The dispersion characteristics of waves in a two-layer round shielded waveguide (with the structure and parameters indicated in the inset).

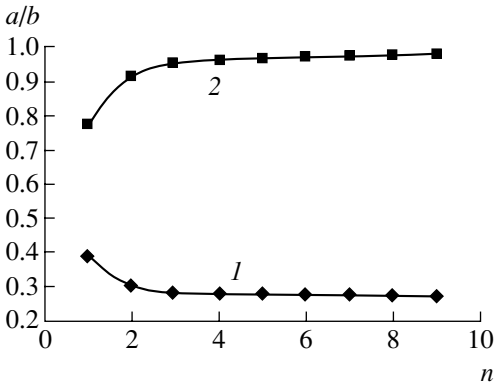

Fig. 2. Plots of the filling factor a/b versus n, describing the (*1*) appearance and (*2*) disappearance of CWs in a two-layer round shielded waveguide with the dielectric rod.

two-layer round shielded waveguide [5]. It can be seen that branches of the complex solutions of the equation corresponding to the CWs appear at the Jordan multiplicity point of the normal waves [6]. If $\varepsilon_2 > \varepsilon_1$ (a waveguide with the dielectric sleeve), the branch of the complex solution appears at the junction point of the dispersion characteristics of the waves EH_{11} and HE_{12}, rather than at the junction point of the dispersion characteristics of the first two waves HE_{11} and EH_{11} as in the case when $\varepsilon_1 > \varepsilon_2$ (a waveguide with the dielectric rod [7]). This peculiarity is just what hampered to a certain extent the search for the CWs in the waveguides with $\tilde{\varepsilon} = \varepsilon_2/\varepsilon_1 > 1$.

Tables 1 and 2 present the values of the filling factor a/b (a and b are the radii of the internal and the external layers, respectively) corresponding to the appearance and disappearance of the complex waves HE_{nm}, EH_{nm} (n is the azimuthal index) in waveguides with a dielectric rod (Table 1) and dielectric sleeve (Table 2). Figures 2 and 3 illustrate the results presented in Tables 1 and 2, respectively. It is clear from these data that the intervals of the filling factors for which the CWs exist expands with increasing azimuthal index n for the two-layer waveguide with the dielectric rod and shrinks for the waveguide with the dielectric sleeve.

On the whole, the results presented in Table 2 and Fig. 3 show that the higher the CW azimuthal index (at a constant radial index) is, the thinner the dielectric sleeve ensuring the existence of this complex wave should be. The intrinsic complex waves exist [2] owing to the formation of opposite power fluxes in the guide structures. Figure 4 shows a distribution of the real part of the complex Poynting vector in the cross section of a two-layer shielded waveguide. It can be seen that power fluxes in the central and peripheral parts of the cross section have opposite directions; as a result, the integral flux equals zero [2].

Table 1. Critical filling factors a/b for a two-layer round shielded waveguide with a dielectric rod

N	Values of a/b for which	
	CWs appear	CWs disappear
1	0.38910301	0.77800264
2	0.29828910	0.91853133
3	0.28233333	0.94941078
4	0.27708631	0.96250251
5	0.27463791	0.97052311
6	0.27133333	0.97551344
7	0.26966667	0.97955086
8	0.26845031	0.98266667
9	0.26666667	0.98433333

Table 2. Critical filling factors a/b for a two-layer round shielded waveguide with a dielectric sleeve

N	Values of a/b for which	
	CWs appear	CWs disappear
1	0.67501047	0.84607483
2	0.73566667	0.87000000
3	0.77266667	0.88566667
4	0.79833333	0.89666667
5	0.81802031	0.90533333
6	0.83233333	0.91203762
7	0.84533333	0.91766667
8	0.85500725	0.92266667
9	0.86333333	0.92666667

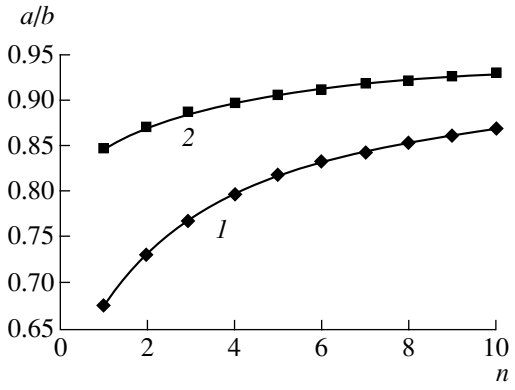

Fig. 3. Plots of the filling factor a/b versus n, describing the (*1*) appearance and (*2*) disappearance of CWs in a two-layer round shielded waveguide with the dielectric sleeve.

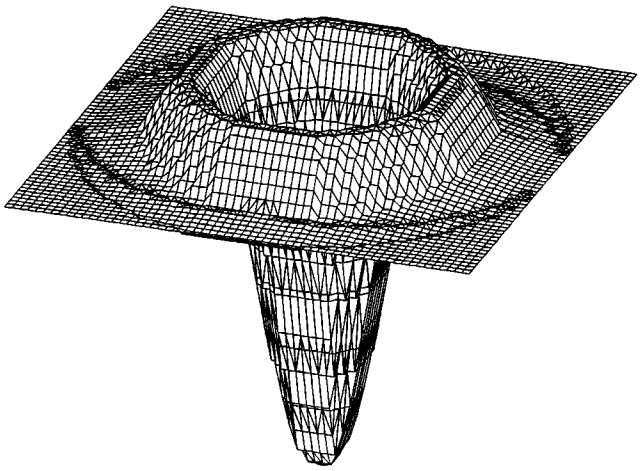

Fig. 4. Distribution of the real part of the complex Poynting vector in the cross section of a two-layer shielded waveguide.

Solutions of the dispersion equation corresponding to the CWs are situated on the complex planes of the transverse wavenumbers [2] and form complex-conjugate pairs; this indicates that two pairs of complex waves with oppositely directed phase velocities exist to the right and left of the source. The longitudinal dependences of their fields [2] assume the forms [2]

$$e^{-i(\beta' - i\beta'')z};\quad e^{i(\beta' + i\beta'')z}\quad \text{(waves I, II)};$$

$$e^{-i(\beta' + i\beta'')z};\quad e^{i(\beta' - i\beta'')z}\quad \text{(waves III and IV)}.$$

Waves I and II propagate to the right of the source, which is conditionally situated at $z = 0$, while waves III and IV propagate to the left of the source. It was shown [2] that the sources described by real functions of the coordinates excite the pairs of waves I, II and III, IV with complex-conjugate amplitudes. The coexistence of these pairs leads to the appearance of a stationary-wave field localized near the source in the infinite two-layer waveguide (in the segment of the two-layer waveguide matched at the ends) [2]. As a result, a phenomenon known as the complex resonance (CR) [2, 8] appears in the structures under consideration, because these structures act as a resonator connected according to "transmission" or "reflection" schemes. A specific feature of the CR is that, in contrast to the usual resonance, this resonance is manifested in the whole interval where the CW exists, so that the structure behaves as a band-pass filter [9].

A real construction of such a band-pass filter is a segment of a two-layer round shielded waveguide loaded at the ends $z = \pm l$ by homogeneously filled waveguides. Taking into account incomplete matching at the ends, the field in the segment of the two-layer round shielded waveguide can be represented in the region $z \in [0–l]$ by the longitudinal components of the Hertz vectors of the form

$$\Pi^e_{z_1} = \psi^e_1(r, \varphi)e^{-i(\beta' - i\beta'')z} + \bar{\psi}^e_1(r, \varphi)e^{i(\beta' + i\beta'')z} + \psi^e_{-1}(r, \varphi)e^{i(\beta' - i\beta'')(z-1)} + \bar{\psi}^e_{-1}(r, \varphi)e^{-i(\beta' + i\beta'')(z-1)} + \sum_{m=1}^{\infty} \psi^e_m(r, \varphi)e^{i\beta_m(z-1)},$$

$$\Pi^h_z = \psi^h_1(r, \varphi)e^{-i(\beta' - i\beta'')z} + \bar{\psi}^h_1(r, \varphi)e^{i(\beta' + i\beta'')z} + \psi^h_{-1}(r, \varphi)e^{i(\beta' - i\beta'')(z-1)} + \bar{\psi}^h_{-1}(r, \varphi)e^{-i(\beta' + i\beta'')(z-1)} + \sum_{m=1}^{\infty} \psi^h_m(r, \varphi)e^{i\beta_m(z-1)}. \quad (6)$$

The first terms in Eqs. (6) with the membrane functions $\psi^e_{\pm 1}(r, \varphi)$; $\psi^h_{\pm 1}(r, \varphi)$ and $\bar{\psi}^e_{\pm 1}(r, \varphi)$; $\bar{\psi}^h_{\pm 1}(r, \varphi)$ describe, respectively, complex waves I and II (plus sign) and III and IV (minus sign). The sums in Eqs. (6) correspond to the usual waves exhibiting reactance damping in the domain of existence of the main CW. Similar representation is valid for the field in the region of $z \in [–l–0]$. The field in the domains of homogeneously filled waveguides is represented by infinite sets of the usual propagating and reactance-damped waves.

Realization of the boundary conditions on the planes $z = 0; \pm l$ with neglected weak interaction at $z = 0$ of the reactance-damped below-cutoff waves appearing at the junctions $z = \pm l$ (we assume that the segment of the two-layer waveguide is sufficiently long) leads, under the condition of orthogonality of the eigenfunctions, to a characteristic equation with respect to the resonance frequencies of the structure under consider-

ation. This equation has, in the general case, the form of the infinite-order determinant:

$$\det[a_{ik}] = 0. \quad (7)$$

The components of the CW fields with the complex-conjugate amplitudes in the planes $z = 0; \pm l$ assume the form

$$\begin{aligned} E_{r_k} &= [\xi_1(r)A_1' - \zeta_1(r)A_1'' - \xi_1(r)C_1' + \zeta_1(r)C_1'']\cos n\varphi, \\ E_{\varphi_k} &= [\xi_2(r)A_1' - \zeta_2(r)A_1'' - \xi_2(r)C_1' + \zeta_2(r)C_1'']\sin n\varphi, \\ H_{r_k} &= [\xi_3(r)A_1' - \zeta_3(r)A_1'' - \xi_3(r)C_1' + \zeta_3(r)C_1'']\sin n\varphi, \\ H_{\varphi_k} &= [\xi_4(r)A_1' - \zeta_4(r)A_1'' - \xi_4(r)C_1' + \zeta_4(r)C_1'']\cos n\varphi, \end{aligned} \quad (8)$$

where subscript "*k*" indicates the complex character of the wave. In the domain of existence of the complex waves, the first column of determinant (7) coincides with the third one and the second column coincides with the fourth one; in other words, $a_{1i} = a_{3i}$, $a_{2i} = a_{4i}$. As a result, the matrix of the characteristic equation (7) is singular in the whole frequency domain of the CWs. The consequence of this singularity is the appearance of the resonance properties of the segment of a two-layer shielded waveguide (loaded on the and by the infinite matched homogeneously filled waveguides) in the whole band of the CW existence rather than at individual frequencies as it takes place in the usual resonance.

In conclusion, we showed that the main feature of the guide structures described by non-self-conjugate operators is the existence of CWs in these structures. Pair excitation of such waves by a single source results in singularity of the matrix of the characteristic equation and, as a consequence, in the appearance of the CR in the whole domain of existence of the CWs. The necessary and sufficient condition for the existence of CWs in a guide structure is the non-self-conjugate character of the boundary problem that describes the structure.

REFERENCES

1. M. A. Naĭmark, *Linear Differential Operators*, 2nd ed. (Nauka, Moscow, 1969; Ungar, New York, 1967).
2. G. I. Veselov and S. B. Raevskiĭ, *Laminar Metal-Dielectric Waveguide* (Radio i Svyaz', Moscow, 1988).
3. G. I. Veselov and S. B. Raevskiĭ, Radiotekhnika **42** (8), 64 (1987).
4. V. A. Neganov, S. B. Raevskiĭ, and G. P. Yarovoĭ, *Linear Macroscopic Electrodynamics* (Radio i Svyaz', 2001), Vol. 2.
5. S. B. Raevskiĭ, Izv. Vyssh. Uchebn. Zaved. Radiofiz. **15**, 112 (1972).
6. P. E. Krasnushkin and E. N. Fedorov, Radiotekh. Élektron. (Moscow) **17**, 1129 (1972).
7. G. I. Veselov and L. A. Lyubimov, Radiotekh. Élektron. (Moscow) **8**, 1530 (1963).
8. G. I. Veselov, S. B. Raevskiĭ, and V. A. Kalmyk, Radiotekhnika (Moscow) **36** (9), 59 (1980).
9. G. I. Veselov, V. A. Kalmyk, and S. B. Raevskiĭ, Izv. Vyssh. Uchebn. Zaved. Radiofiz. **26**, 900 (1983).

Translated by M. Kobrinskiĭ

Technical Physics Letters, Vol. 30, No. 1, 2004, pp. 30–32. Translated from Pis'ma v Zhurnal Tekhnicheskoĭ Fiziki, Vol. 30, No. 1, 2004, pp. 65–71.

A Multiplexer/Demultiplexer for Coarse Wavelength-Division Multiplexing

V. K. Sakharov, L. P. Prokof'eva, and V. V. Shcherbakov

Center-VOSPI Company, Moscow, Russia

e-mail: center-vospi@mtu-net.ru

Received April 16, 2003; in final form, July 7, 2003

Abstract—Increasing the transmission capacity of existing and newly developed optical communication lines and networks (data exchange systems) implies the use of wavelength-division multiplexing (WDM). Optical fiber multiplexers and demultiplexers are the WDM devices necessary for combining several carriers in a common optical tract and performing the inverse function. We propose a multiplexer/demultiplexer device based on fused single-mode fiber couplers. © *2004 MAIK "Nauka/Interperiodica".*

Introduction. The technology of single-mode fiber couplers is now well developed and allows fiber couplers to be manufactured for a large variety of applications [1, 2]. This Letter is devoted to the use of such couplers in the devices for wavelength-division multiplexing (WDM).

As is known, the most effective WDM in modern communication networks and data exchange systems employing single-mode optical fibers is provided by the so-called dense wavelength-division multiplexing (DWDM) technology that allows the channel separation to be reduced to 3.2, 1.6, and 0.8 nm (400, 200, and 100 GHz, respectively) or even lower. This technology is based on frequency-stabilized semiconductor lasers, optical fiber multiplexers and demultiplexers, switches, cross-connectors, circulators, and many other devices; long lines require the use of optical amplifiers of the fiber, semiconductor, and Raman types. The development of DWDM is hindered by complexity of the device technology and accordingly high cost.

An alternative to DWDM is offered by the coarse WDM (CWDM) technology. In this case, the channel separation (typically, 20 nm) is greater and the transmission capacity is accordingly lower as compared to DWDM. The technical requirements for the CWDM system elements can be also significantly reduced: for example, simpler and cheaper semiconductor lasers can be employed.

This paper is devoted to multiplexers and demultiplexers for CWDM—devices necessary for combining several carriers in a common optical tract and performing the inverse function of carrier extraction and separation.

Optical multiplexers/demultiplexers can be created [3] based on various devices such as thin-film interference filters, gratings, Bragg grating fibers, arrayed waveguide gratings, etc. In general, the possibility of using single-mode fiber couplers for combining or separating more than two wavelengths was considered in [4], but we believe that this problem requires more detailed analysis.

Fiber coupler multiplexer. Fused single-mode fiber couplers of the 2×2 type are obtained by drawing and fusing two heated quartz fibers. This results in the formation of a working region that is a common narrow portion of fibers with smooth cone-shaped junctions on both ends. The working region is "packed" into a protective case, with input/output fibers on the two sides used for the radiation entrance and exit.

The manufacture of a simple coupler, intended to perform the function of optical power division or summation, is monitored by feeding laser radiation with a preset wavelength into one of the input fibers and by measuring the output power in the two exit fibers. The fusion process is terminated when the output power ratio reaches a desired level. The coupling coefficients weakly depend on the wavelength, being virtually constant in the 30–40 nm interval.

If the drawing and fusion stage is continued, it is possible to observe the process of a periodic pumping of the optical output power from one exit fiber to another. The spectral properties of the coupler become more pronounced: the coupling coefficients are oscillating functions of the radiation wavelength. Such couplers are called multiplexers or WDM couplers. The mechanism of spectral oscillations and their period are determined by the coupling of propagating and interacting modes in the working region of the coupler [5].

The coupler multiplexers studied in this work were manufactured in a setup with a graphite heater [6] providing for a fusion temperature on the order of 1900°C. The spectral characteristics were monitored using an incandescent lamp as the wideband radiation source and an Anritsu 4008 optical spectrometer.

The technology of coupler multiplexers encounters certain difficulties related to the fact that the coupling

1063-7850/04/3001-0030$26.00 © 2004 MAIK "Nauka/Interperiodica"

coefficients do not always behave as oscillating functions with the peak values close to 0 and 1, corresponding to the complete pumping of radiation to one of the exit fibers. Figure 1a shows the spectrum of radiation measured at the output of a coupler based on a single-mode fiber of the SM-28 type, for which the jump of the refractive index at the core–shell interface is $\Delta n/n \approx 3 \times 10^{-3}$. For comparison, Fig. 1b presents the analogous spectrum of a coupler based on a special single-mode fiber with a jump of the refractive index on the order of $\Delta n/n \approx 10^{-2}$. As can be seen, a significant pumping of radiation from one exit fiber to another in the former case is possible only within certain narrow spectral regions, whereas the latter coupler allows complete pumping in the entire spectral interval from 1.2 to 1.7 μm.

The spectrum in Fig. 1a is a sinusoid with a small period ($\Delta\lambda \approx 24$ nm) modulated by a function of large period $\Delta\Lambda \approx 150$ nm. The resulting spectrum has the form of beats with a difference frequency corresponding to the latter period. This pattern can be interpreted [7] as a superposition of the spectra of two coupling coefficients corresponding to the pumping of waves possessing mutually orthogonal polarizations, related to a birefringence in the working region of the coupler.

The spectrum in Fig. 1b is virtually free of any additional modulation, so that the birefringence is not manifested. Therefore, it is recommended to make coupler multiplexers using special fibers with high values of the index jump $\Delta n/n$ rather than standard single-mode fibers.

An important feature of the nonstandard fibers intended for manufacturing couplers was their core diameter being smaller than that of the usual commercial fibers (7 versus 10 μm). This might lead to large additional optical losses when coupler multiplexers and related devices based on such fibers are connected to lines employing standard fibers. However, it will be shown below how to reduce the level of additional losses to an acceptably low level.

A special feature of the technology of coupler multiplexers is the need for precise adjustment of the period and phase of the spectra for a given set of wavelengths. For the four-channel multiplexer/demultiplexer considered below, the couplers have to possess oscillation periods of 40 and 80 nm, the positions of extrema for the given wavelengths deviating by no more than ±3 nm, the total losses within 0.2–0.5 dB, and an insulation between channels about 20–30 dB.

CWDM multiplexer/demultiplexer design. A four-channel multiplexer/demultiplexer with a channel separation of $\Delta\lambda = 20$ nm represents a cascade of three couplers with input/output fibers connected by welding. The device is arranged in a $10 \times 52 \times 112$ mm case filled with an elastomer. The nominal channel wavelengths were $\lambda_1 = 1510$ nm, $\lambda_2 = 1530$ nm, $\lambda_3 = 1550$ nm, and $\lambda_4 = 1570$ nm. An optical scheme of this device is depicted in Fig. 2a.

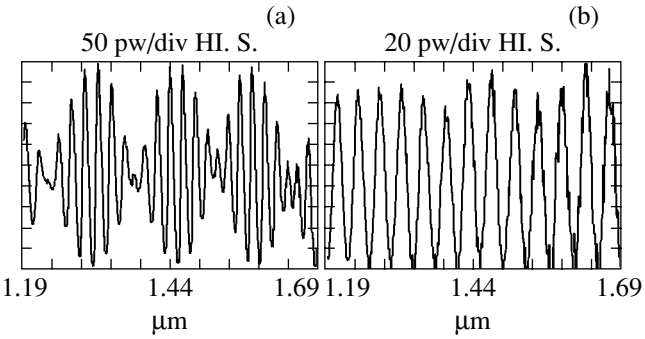

Fig. 1. Output spectra of the couplers made of (a) the standard fiber with $\Delta n/n \approx 3 \times 10^{-3}$ and (b) a special fiber with $\Delta n/n \approx 10^{-2}$.

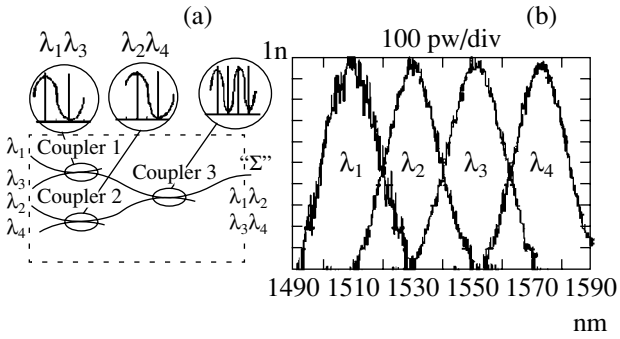

Fig. 2. A four-channel multiplexer/demultiplexer: (a) schematic diagram and (b) spectral characteristics.

The extrema in the spectra of coupling coefficients for coupler 1 correspond to λ_1 and λ_3, while those for coupler 2 correspond to λ_2 and λ_4 (see the insets in Fig. 2). As a result, the spectra of the transmission coefficients of these couplers possess the same period of oscillations but are shifted by a quarter period (20 nm) relative to each other. Coupler 3 possesses a half smaller period of oscillations and the extrema at λ_1, λ_2, λ_3, and λ_4.

Owing to the selected spectral characteristics of the component couplers, the disclosed device can perform the function of a multiplexer when waves λ_1 and λ_3 are fed to the inputs of coupler 1 and waves λ_3 and λ_4 are fed to the inputs of coupler 2. Then, the wave pairs $\{\lambda_1, \lambda_3\}$ and $\{\lambda_2, \lambda_4\}$ enter coupler 3 and all four waves appear on the device output Σ.

As can be seen, the same device used in the reverse direction performs the function of a demultiplexer, whereby four waves λ_1, λ_2, λ_3, and λ_4 fed to input Σ pass through coupler 3 to form pairs $\{\lambda_1, \lambda_3\}$ and $\{\lambda_2, \lambda_4\}$ at the corresponding outputs and then each individual wave is obtained on the corresponding outputs of couplers 1 and 2. Moreover, this device can

simultaneously operate as a multiplexer/demultiplexer: for example, waves λ_1 and λ_2 enter the line, while the two other waves, λ_3 and λ_4, coming from the line are separated and fed to photodetectors.

Figure 2b shows the spectral characteristics of this device operating in the demultiplexer mode, whereby broadband radiation is fed to input Σ and the partial optical spectra are sequentially measured on four outputs. According to the results of our measurements, deviations of the central wavelength in the channels from nominal values did not exceed 2–3 nm, the spectral channel width (on a 3 dB level) was about 20 nm, and the channel isolation was not less than 25 dB.

As was indicated above, the multiplexer/demultiplexer was implemented on special fibers with a smaller core diameter as compared to that of standard fibers. The intrinsic optical losses of a device based on fibers with a core diameter of $d = 7$ μm in both regimes for any of the four channels fall within 0.5–1 dB.

We have also estimated the optical losses arising during the passage of radiation through a junction between a standard fiber with $d_0 \approx 10$ μm and the special fiber with $d \approx 7$ μm: the losses amounted to about 2.5 dB. However, by slightly modifying the junction technology, whereby the usual welding was followed by local heating of the fiber with a greater core diameter d_0 near the junction with its drawing to 2–3 mm, the additional junction losses were significantly decreased to within 0.8–1.0 dB. The total losses in the multiplexer/demultiplexer used in the optical tracts made of standard fibers do not exceed 2.0 dB.

It should be noted that the number of stages in the proposed device can be readily increased. One additional channel can be obtained by introducing a new coupler with the corresponding spectral characteristic. For example, a channel operating at $\lambda_5 = 1590$ nm can be obtained by connecting a coupler with the spectral extrema at 1510 and 1590 nm to the λ_1 input. By the same token, adding three more couplers, we obtain an eight-channel multiplexer/demultiplexer with a channel separation of $\Delta\lambda = 20$ nm, operating at the set of wavelengths 1470, 1490, …, 1610 nm.

Conclusion. We have considered the manufacturing technology and spectral properties of fused single-mode fiber multiplexers and demultiplexers and the design and characteristics of optical multiplexer/demultiplexer devices for CWDM systems. Such devices can operate in both 1.3 and 1.55 μm wavelength ranges. The number of channels can be increased according to demands.

At present, there are good prospects for the use of CWDM technology by domestic network developers. This would allow a severalfold increase in the transmission capacity of existing lines without large expenditures, avoiding the need for running new optical cables and making a recourse for future developments.

REFERENCES

1. V. Trippe, Proc. SPIE **1085**, 75 (1990).
2. X. Daxhelet and F. Gonthier, Proc. SPIE **42161**, 67 (2001).
3. D. Anderson, WDM Solutions **3** (6), 97 (2001).
4. K. O. Hill, D. C. Johnson, and R. G. Lamont, in *Proceedings of the 5th International Conference on Integrated Optics and Optical Fiber Communication ICIO-OFC'85, Venezia, 1985*, Vol. 1, pp. 567–570.
5. A. Yariv, IEEE J. Quantum Electron. **9**, 919 (1973).
6. E. G. Gerasimov, L. N. Gnatyuk, and V. K. Sakharov, Elektron. Prom-st', No. 8, 59 (1987).
7. M. S. Yataki, D. N. Payne, and M. P. Varnham, in *Proceedings of the 3rd Optical Fiber Communication Conference OFC'85, San Diego, 1985*, pp. 108–110.

Translated by P. Pozdeev

Technical Physics Letters, Vol. 30, No. 1, 2004, pp. 33–35. Translated from Pis'ma v Zhurnal Tekhnicheskoĭ Fiziki, Vol. 30, No. 1, 2004, pp. 72–77.

Converging Shock Waves in Porous Media

A. A. Charakhch'yan[a], I. V. Lomonosov[b], V. V. Milyavskiĭ[b], V. E. Fortov[b], A. A. Frolova[b], K. V. Khishchenko[b], and L. V. Shurshalov[b]

[a] *Dorodnitsyn Computation Center, Russian Academy of Sciences, Moscow, Russia*
[b] *Institute for High Energy Densities, Associated Institute for High Temperatures, Russian Academy of Sciences, Moscow, Russia*
e-mail: chara@ccas.ru

Received June 30, 2003

Abstract—We have numerically solved several problems related to converging shock waves, including (i) one-dimensional spherical and cylindrical waves with cumulation limited to a ball or cylinder of small radius and (ii) shock-wave flow in a cone-shaped solid target. The passage from a continuous loaded substance to a porous medium in these problems leads to a significant increase in both temperature and pressure in the sample. This character of pressure variation depending on the porosity qualitatively differs from the case of plane waves of constant intensity, for which an increase in the sample porosity under otherwise equal conditions of loading always leads to a decrease in the pressure. © *2004 MAIK "Nauka/Interperiodica".*

Consider a flow by which a shock wave propagates in a substance (continuous or porous). The problem is formulated in a commonly accepted form [1]. The substance behind the wave is assumed to be nonporous and described using equations of the hydrodynamics of continuum and the equations of state, while the porosity is taken into account only by setting the initial density for the shock adiabat. Based on the laws of conservation, this approach provides a rather satisfactory description of experimental data on the compressibility of porous substances in many cases, although it fails to explain the results of some experiments showing anomalously high temperature behind the wave front [2].

A question naturally arises as to how the flow parameters vary behind the shock wave front as a result of the change in porosity when the other parameters of the problem remain unchanged. As is well known, the temperature behind the shock wave front increases with the degree of porosity. As for the pressure, the situation is not as evident. The parameters of a shock wave appearing in a porous substance are determined by solving the problem of a decay of discontinuity at the boundary with a medium from which the wave entered the substance. Omitting the details of an analysis of this problem, we can summarize the results as follows.

The derivative of pressure behind the shock wave front with respect to the density ρ_{00} before the front is positive, $\partial p/\partial\rho_{00} > 0$, if two conditions are satisfied: (i) $du/dp > 0$ (u is the velocity behind the front) and (ii) the thermodynamic derivative behind the front is also positive, $(\partial\varepsilon/\partial v)_p > 0$ (ε is the specific internal energy, $v = \rho^{-1}$ is the specific volume). Evidently, both these conditions are always satisfied. Therefore, an increase in the degree of porosity (i.e., a decrease in ρ_{00}) is practically always accompanied by a decrease in intensity of a shock wave entering into a substance. However, this by no means implies that the pressure behind the shock wave front propagating in a porous substance cannot exceed the value observed for a less porous or continuous medium.

Below, we present a numerical solution to the problem involving convergent shock waves in the presence of a certain mechanism of limitation of the cumulation. Under these conditions, the passage from continuous to porous medium leads to an increase in both temperature and pressure.

In our numerical calculation, the porous substance was graphite with as density of $\rho_{00} = 1.7$ g/cm^3 (the crystal density being $\rho_0 \approx 2.26$ g/cm^3). The equation of state for graphite is analogous to that used in [3], but the phase transition of graphite into diamond was not taken into account in this calculation.

The problem is formulated using a system of equations of nondissipative hydrodynamics of compressible media,

$$\frac{d\rho}{dt} + \rho\,\mathrm{div}\,\mathbf{u} = 0, \quad \rho\frac{d\mathbf{u}}{dt} + \nabla p = 0,$$
$$\rho\frac{d(\varepsilon + \mathbf{u}^2/2)}{dt} + \mathrm{div}\,p\mathbf{u} = 0, \tag{1}$$

closed by the equations of state,

$$p = p(\rho, T), \quad \varepsilon = \varepsilon(\rho, T). \tag{2}$$

Here, $\mathbf{u}$ is the velocity vector, $d/dt = \partial/\partial t + \mathbf{u}\nabla$ is the Lagrange derivative with respect to time, and T is the absolute temperature. At the initial time, we set the density ρ_{00}, the temperature T_0, and (for a porous sub-

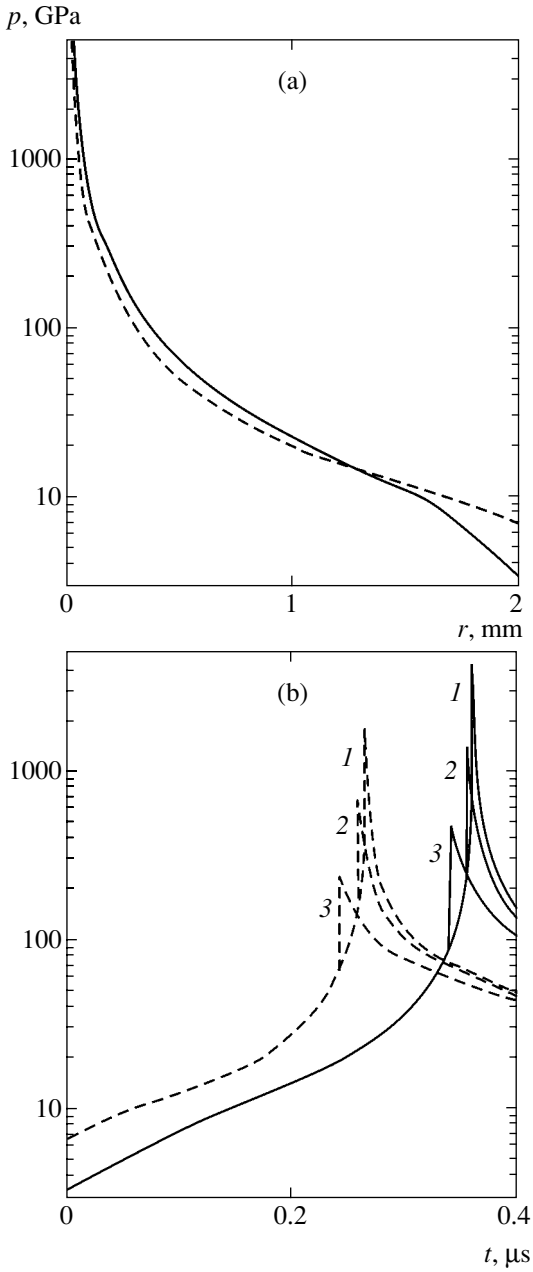

Fig. 1. Plots of the spherical shock wave intensity in a ball of porous (solid curves) and continuous (dashed curves) graphite: (a) pressure at the front versus the shock wave radius *r*; (b) pressure maximum (over space) versus time in the problem with cumulation limited to $r_0 = 0.1$ (*1*), 0.2 (*2*), and 0.4 mm (*3*).

stance) the crystal density $\rho_0 > \rho_{00}$. It is assumed that the porous substance begins to move after passage of the bow shock wave. The boundary condition on the wave is determined by the shock adiabat with the initial state parameters ρ_{00}, $p_0 = p(\rho_0, T_0)$, and $\varepsilon_0 = \varepsilon(\rho_0, T_0)$.

The problem was numerically solved using two methods of calculation through the bow shock wave. The first method is based on a simple model of pore kinetics (see, e.g., [4]). The second method is based on the model [3] of a two-phase (graphite–ideal gas) mixture. The results of control calculations using both methods showed good mutual agreement.

Consider a spherical shock wave in a graphite ball with a radius of 2 mm caused by the impact of an aluminum ball impinging at a velocity of 1 km/s. The calculations were performed to within the second order of accuracy on a Lagrange lattice with 100, 200, 400, or 800 intervals in graphite, which showed evidence of convergence of the numerical solution.

Figure 1a shows the calculated plots of the pressure *p* at the wave front versus the front radius *r.* Beginning with a certain radius *r,* the pressure in the porous graphite is significantly higher than that in the continuous graphite. Introducing limitations on the cumulation in the form of a ball of small radius r_0 [5], we obtain an analogous relationship for the maximum pressures in the system. This is illustrated in Fig. 1b, which shows the plots of maximum pressure versus time for three values of r_0. As can be seen, the passage from continuous to porous graphite leads to an almost twofold increase in the maximum pressure. For an analogous cylindrical wave, the maximum pressure increases upon passage from continuous to porous graphite by a factor of about 1.5.

Let us consider the shock compression of graphite in the case of cone-shaped solid targets [3]. The impinging body strikes a steel target containing a cone-shaped cavity filled with graphite. In this case, Eqs. (1) were solved using a scheme described in [3]. The main calculations were performed on a 25×50 lattice (the first is the number of intervals along the cone base and the second is that along the axis of symmetry). The control calculations were performed on a lattice of double density in both directions.

Figure 2 shows the families of isobars for the initial porous graphite for two successive moments of time, calculated using the following parameters: aluminum ball striker velocity, 2.5 km/s; cone angle, 75°; cone base radius, 2.5 mm; steel spacer width between graphite cone and striker, 8 mm. Figure 2a depicts the bow shock wave near the axis of symmetry and the pulse of compression from the side boundary of the cone. Exact calculation of the bow shock wave parameters based on the conservation laws gives ~9 GPa for the pressure behind the front. Numerical calculation gives approximately the same value, which is evidence of the adequacy of the employed scheme. In the case of continuous graphite, the pressure behind the shock wave front increases up to ~17 GPa. By the next time instant illustrated in Fig. 2b, a shock wave of nearly spherical shape is formed that converges to the cone vertex. The mechanism of limited cumulation in this wave corresponds to deformation of the cone wall.

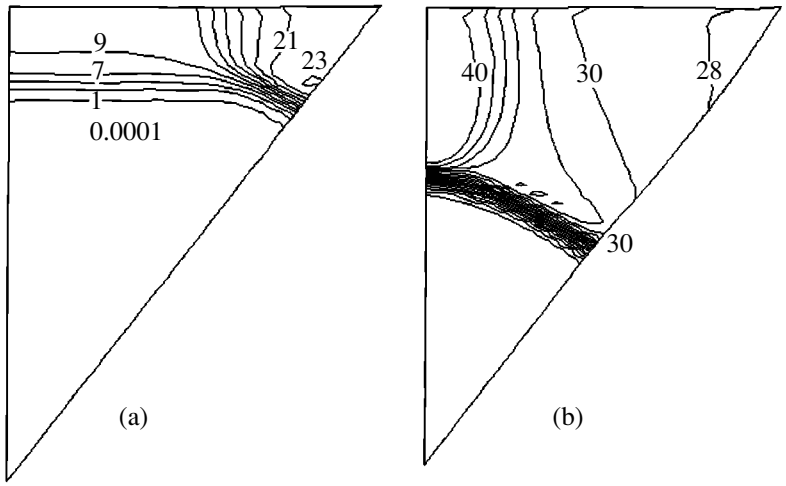

Fig. 2. The families of isobars (figures on the curves indicate pressures in GPa) plotted in cylindrical coordinates for a cone-shaped porous graphite target at $t = 1.6$ (a) and 1.8 μs (b) upon impact.

Time variation of the pressure within a certain Lagrangian particle situated at the cone vertex is qualitatively similar to the curves in Fig. 1b. The passage from continuous to porous graphite leads to an approximately threefold increase in the maximum pressure (reaching up to ~270 GPa). Calculations on a denser lattice give a somewhat higher value of the maximum pressure. The calculations were performed for various striker velocities, ranging from 3 km/s (aluminum) to 600 m/s (copper), and various parameters of the graphite cone geometry (including truncated cone). In all cases, the passage from continuous to porous graphite leads to approximately a threefold increase in the maximum pressure.

As is known, the main parameters determining the phase transition of graphite into diamond are the characteristic transformation time and the minimum (threshold) pressure above which this transition becomes possible. High maximum pressures observed for the porous graphite imply the remarkable possibility of providing conditions for the phase transition by means of impact using low-velocity strikers. By increasing the target size, it is possible to extend the period of high pressure holding in the sample.

REFERENCES

1. Ya. B. Zel'dovich and Yu. P. Raĭzer, *Physics of Shock Waves and High-Temperature Hydrodynamic Phenomena* (Nauka, Moscow, 1966; Academic Press, New York, 1967).
2. G. V. Belyakov, Dokl. Akad. Nauk SSSR **218**, 1280 (1974) [Sov. Phys. Dokl. **19**, 326 (1974)].
3. I. V. Lomonosov, V. E. Fortov, A. A. Frolova, *et al.*, Zh. Tekh. Fiz. **73** (6), 66 (2003) [Tech. Phys. **48**, 727 (2003)].
4. A. Z. Zhuk, A. V. Ivanov, and G. I. Kanel', Teplofiz. Vys. Temp. **29**, 486 (1991).
5. E. I. Zababakhin and I. E. Zababakhin, *Unbounded Cumulation Phenomena* (Nauka, Moscow, 1988).

Translated by P. Pozdeev

Technical Physics Letters, Vol. 30, No. 1, 2004, pp. 36–39. Translated from Pis'ma v Zhurnal Tekhnicheskoĭ Fiziki, Vol. 30, No. 1, 2004, pp. 78–87.

Study of the Dynamic Characteristics of Polymer-Dispersed Liquid Crystal Compositions: Prospects for Optoelectronic Applications of Fullerene Complexes with Phthalocyanine Nanocrystals

N. V. Kamanina and I. Yu. Denisyuk

Vavilov Optical Institute, State Scientific Center of the Russian Federation, St. Petersburg, Russia

e-mail: kamanin@ffm.ioffe.ru; denisiuk@mail.admiral.ru

Received April 24, 2003; in final form, August 5, 2003

Abstract—The switching and modulation characteristics of fullerene-containing polymer-dispersed liquid crystal structures involving fullerene complexes with magnesium phthalocyanine nanocrystals are studied for the first time. It is established that these systems are characterized by small switching times of the electrooptical response to pulsed drive voltage under the conditions of cw He–Ne laser irradiation. It is suggested that effective charge carrier production in the structures doped with pure phthalocyanine leads to frustration of a homogeneous orientation of the liquid crystal mesophase, which is restored upon adding C_{60} and/or C_{70} fullerenes. A possible reorientation mechanism is considered and it is shown that fullerene-containing polymer-dispersed liquid crystal systems with distributed orientation related to the presence of fullerene complexes with magnesium phthalocyanine can be used for the effective switching of electrooptical response and have good prospects for application in the systems of optical data processing and in display technologies. © *2004 MAIK "Nauka/Interperiodica".*

Introduction. The electrical and optical processes in liquid crystal mesophases are widely used for the development and verification of basic physical models for various mechanisms of laser–matter interaction. These processes are also promising for application in optoelectronics, including devices for data recording, processing, and storage, spatial light modulators (SLMs) [1–4], laser radiation limiters [5, 6], holographic elements [7, 8], reversible data recording media, etc. Among the electrically and optically controlled SLMs, a special place belongs to those based on polymer-dispersed liquid crystal (PDLC) structures [9].

Good prospects of the investigation and applications of thin films of PDLC compositions, representing liquid crystal (LC) droplets dispersed in a polymer matrix, are now commonly recognized. This is determined by the facts that, first, such systems retain some properties of the polymer matrix such as film-forming properties and high mechanical strength and, second, they acquire the unique electrical and optical properties inherent in the LC mesophase. PDLC-based systems can operate without polarization devices (which significantly increases the display brightness), exhibit small switching times, pose no special requirements related to aligning surfaces, and allow the threshold and hysteresis problems to be readily solved.

The principle of operation of PDLC-based cells, which is described in much detail elsewhere [9, 10], consists in leveling the refractive indices of the LC mesophase and the light-sensitive component under the action of a control signal.

In recent years, it has been established that the transmission of LC systems can be effectively controlled by introducing fullerene clusters. This doping allows the laser action threshold to be modified, makes possible effective optical data recording, and improves the operation speed of PDLC-based cells. Note that, in fullerene-containing LC systems without light-sensitive (polymeric or monomeric) base, the laser radiation limitation threshold is on a level of ≤ 0.09 J/cm^2 [5], while in systems using a resonance nonlinearity of chiral nematic LCs, this parameter amounts to $\sim 10^{-6}$ J/cm^2 [6]. The efficiency of recording amplitude-phase holograms and the process of optical data erasure in PDLCs were reported in [8, 11]. The dynamic characteristics of fullerene-containing PDLCs were studied in [11, 12]. It was established that the switching characteristics are significantly improved due to accelerated rotation of the anisotropic molecules in the presence of fullerenes, which is probably related to the high intrinsic rate of fullerene reorientation under the action of external factors. [13].

In this study, we have continued the search for photosensitive matrices admitting the introduction of fullerene clusters aimed at the optimization of the dynamic characteristics of electrically and optically controlled PDLC-based devices for real-time data display systems. In particular, fullerene-containing PDLC

structures involving fullerene complexes with magnesium phthalocyanine have been studied for the first time.

Experimental. The experiments were performed with PDLC-based cells of the *S* type with a layer thickness of 10 μm and the initial planar orientation. The light-sensitive component in the PDLC systems was represented by magnesium phthalocyanine (MgPc) nanocrystals in the *X* form. The synthesis of these nanocrystals is described elsewhere [14]. The process is based on the formation of a nanocrystalline MgPc hydrate as a result of the Pc solution precipitation with water in the presence of alcohols. The ratio of light-sensitive and LC components was 1/100. Finally, the PDLC structures were sensitized by adding 0.1–0.3 wt % C_{60} and/or C_{70} fullerenes. The electrooptical LC component was represented by the standard nematic LC systems with a positive optical and dielectric anisotropy: NZhK 1282 (Δn = 0.164, $\Delta\varepsilon$ = 9.9); NZhK 1289 (Δn = 0.168, $\Delta\varepsilon$ = 10); and E7 BDH (Δn = 0.224, $\Delta\varepsilon > 0$). The aligning films of 0.5 μm thickness, producing orientation of the electrooptical layer, were applied to glass substrates preliminarily coated with a transparent indium tin oxide (ITO) based conducting film. The aligning films were deposited in a centrifuge from 2.5–3% solutions of 81A and 81B polyimides in tetrachloroethane, dried for 8–12 h to complete evaporation of the solvent, and (immediately before LC application) rubbed with a flannel fabric.

The cells were driven by rectangular voltage pulses with an amplitude of A = 10–60 V, a duration of τ = 5–100 ms, and a repetition rate of $1/T$ = 0.2–100 Hz. Each cell was placed between crossed polarizers and exposed to the radiation of a He–Ne laser (λ = 633 nm) response. The cell design and the scheme of the transmission measurements were analogous to those described previously [15, 16]. We studied the electrooptical response buildup time with respect to the first transmission oscillation and detected a transition to the neighboring extremum of the *S* curve, which corresponded to a change in the phase shift by π. In addition, we measured the relaxation times, the modulation characteristics, and spectral features of the PDLC structures. The spectral measurements were performed on a Perkin-Elmer Model 555 spectrophotometer.

Results and discussion. Figure 1 shows the typical response oscillograms. Analysis of these data shows that the PDLC structures based on the MgPc–fullerene–LC system are characterized by extremely small switching times. For example, the switch-on time was 2, 1.7, 1.5, and 1 ms for a drive voltage pulse amplitude of 20, 30, 35, and 40 V, respectively, at a pulse repetition rate of 0.5 Hz and pulse duration of 30 ms. The switching characteristics of the fullerene-containing nanostructured PDLC medium studied are almost ten times better than those observed previously for PDLCs using a conjugated 2-cyclooctylamine-5-nitropyridine (COANP) system [11, 12]. It should be noted that a comparison of the characteristics of these two PDLC systems was performed for close values of the drive voltage and close cell thicknesses. An analogous situation was observed for the switch-off times, which were equal to 20, 15, and 10 ms for a drive voltage pulse amplitude of 30, 35, and 40 V, respectively, at the pulse repetition rate and pulse duration indicated above.

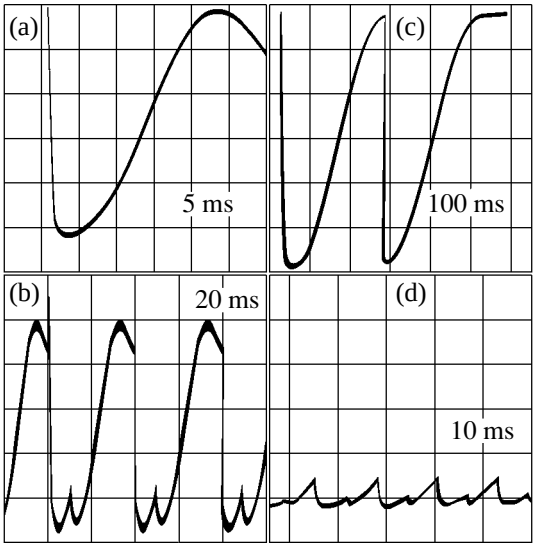

Fig. 1. The typical response oscillograms: (a, b) PDLC with C_{60}; (c, d) PDLC with C_{70}. Drive voltage pulse duration: 30 ms (a–c), 7.5 ms (d); drive voltage pulse amplitude: 35 V; drive voltage frequency: 0.5 (a), 25 (b), 10 (c), and 62 Hz (d). Sweep time indicated in the panels.

According to the published data [1, 9, 17], the complete reorientation of nematic LC into a position rotated by 90° in the case of the Fréedericksz effect under the action of a pulsed electric field takes about 20–30 ms for a drive voltage amplitude of ~25 V. Relaxation of the molecules to the initial state with θ = 0° (i.e., to a virtually planar orientation) is a much slower process, taking a time on the order of 100 ms and depending on the system temperature in the region of existence of the mesophase. Thus, a nanostructured medium with fullerene–MgPc complexes significantly accelerates the transition processes in PDLCs by facilitating reorientation of the LC mesophase within a shorter time period.

It should be recalled that previously, in studying the characteristics of PDLCs based on fullerene-COANP complexes, it was suggested that a decrease in the time of switching under the action of a drive voltage is explained by the accelerated rotation of fullerene molecules interacting with LC molecules [12]. In this context, it should be noted that some investigations of the rotation mobility of C_{60} and C_{70} molecules showed that their rotation rate is temperature-dependent and amounts to ~10^{12} s^{-1} at T = 300 K. Indeed, C_{60} molecules excited at 528 nm showed the following charac-

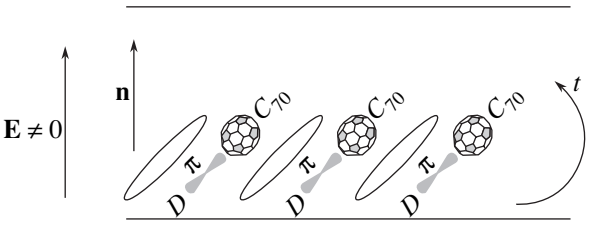

Fig. 2. Schematic diagram illustrating the possible mechanism of accelerated LC reorientation in a nanostructured system with fullerene–MgPc complexes (see the text for explanations).

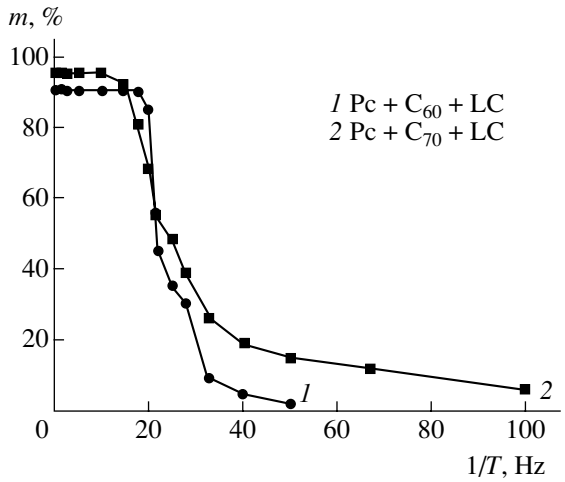

Fig. 3. Plots of the modulation depth versus drive voltage pulse repetition rate for PDLC structures sensitized with fullerenes (*1*) C_{60} and (*2*) C_{70}. Drive voltage pulse amplitude: 35 V.

teristic times of this process in various solvents: 7 ± 1.5 ps (toluene); 10.3 ± 1.5 ps (*o*-dichlorobenzene); 13 ± 2 ps (*o*-xylene); 3.5 ± 1.5 ps (decalin) [13]. Thus, the rate at which a fullerene molecule can follow a change in the electric field vector of the light wave is very high.

Under the experimental conditions studied in [12], excitation of the fullerene-containing structures with He–Ne laser radiation led to a sufficiently rapid change in the boundary conditions at the fullerene-containing aligning layer–electrooptical layer interface which, in turn, induced accelerated reorientation of the LC director under the action of a drive voltage pulse. It should be noted that this variation of the boundary conditions should probably be taken into account in the analysis of relations presented in [9, 17] for the energy of LC dipole binding to a substrate surface in the Rapini framework. This can be done, for example, by introducing an additional term more adequately describing the complicated character of the reorientation of molecules in LC compositions. In addition, accelerated reorientation was already manifested in the first stage (prior to switching on the pulsed drive voltage), leading to partial transmission laser radiation before arrival of the voltage pulse. This is direct evidence for the ability of a fullerene molecule to rapidly follow the light wave (or the electric field strength) in a fullerene-containing cell and in the electrooptical layer.

In this paper, we propose the following interpretation of the acceleration of dynamic processes in the Pc–fullerene–LC system. The basic idea is that an additional field gradient is created due to the effective charge transfer from the organic donor (Pc) and acceptor (fullerene), followed by the rotation of LC dipoles along the conjugated Pc–fullerene system. Therefore, the Ps–fullerene complex possesses an additional dipole moment accelerating reorientation processes in the system. The appearance of this additional moment is probably favored by the effective charge production in Pc nanocrystals [18] under the action of light. This factor enhances the effective charge separation between Pc and fullerene, leading to an increase in polarization of the whole system. Note that this process may be called "distributed nanostructured alignment factor," since the orientation of LC takes place upon adding a distributed Pc–fullerene system into the LC mesophase (the Pc–fullerene complex possesses increased polarization and the LC director is aligned along the dipole vector of this complex). This effect can be used as the new method of orientation of the LC compositions. This model is schematically depicted in Fig. 2, where fullerene C_{70} plays the role of the acceptor fragment in the proposed composite.

It should also be noted that, in the experiments with PDLCs based on the MgPc–LC system (not containing fullerenes in volume of the mesophase), the system exhibited disordering after switching on the drive voltage pulse, which was manifested by scattering of the transmitted laser radiation.

Figure 3 shows the modulation characteristics of the new PDLC mixtures. As can be seen, PDLCs containing anisotropic molecules of fullerene C_{70} modulate laser radiation at drive voltage frequencies significantly (almost fourfold) higher than the standard TV frame frequency (25 Hz): the modulation efficiency is sufficiently high up to 100 Hz. Therefore, the newly synthesized compositions and related fullerene-containing PDLC-based SLMs can be used as high-speed optical switches and diffraction elements in systems with direct electrical or optical control. In addition, these materials can be promising 3D-recording media for writing amplitude-phase holograms.

Conclusions. (1) The switching and modulation characteristics of PDLCs based on the MgPc–fullerene–LC system have been studied for the first time. Adding C_{60} and/or C_{70} fullerenes significantly reduces the switching time of PDLC-based cells.

(2) It is demonstrated that fullerenes significantly influence the process of LC reorientation on the volume of mesophase. A possible mechanism of reorientation is proposed that is based on the appearance of an addi-

tional field gradient due to the effective charge transfer from an organic donor (Pc) and acceptor (fullerene), followed by the accelerated rotation of LC dipoles along the conjugated Pc–fullerene system.

(3) The results of this study can be used for the development of novel LC-based devices operating on a real time scale. These data are also useful for the development of technological processes for the synthesis of new highly sensitive fullerene-containing compositions for display devices.

(4) The results of this investigation can be used for the development of a new method of the alignment of LC dipoles based on the use of additional field gradient created due to the effective charge transfer from the organic donor (e.g., Pc) and acceptor (e.g., fullerene).

Acknowledgments. The authors are grateful to T.I. Vasil'eva (Vavilov Optical Institute, St. Petersburg) for depositing transparent conducting ITO films and to O.D. Lavrentovich (Kent State University, USA) for kindly providing E7 (BDH) composition.

REFERENCES

1. A. A. Vasil'ev, D. Kasasent, I. N. Kompanets, and A. V. Parfenov, *Spatial Light Modulators* (Radio i Svyaz', Moscow, 1987).
2. R. S. McEwen, J. Phys. E: Sci. Instrum. **20**, 364 (1987).
3. N. V. Kamanina and N. A. Vasilenko, Electron. Lett. **31**, 394 (1995).
4. N. V. Kamanina and N. A. Vasilenko, Opt. Quantum Electron. **29**, 1 (1997).
5. I. C. Khoo and H. Li, Appl. Phys. B **59**, 573 (1994).
6. V. V. Danilov, A. G. Kalintsev, N. V. Kamanina, and S. A. Tul'skiĭ, Pis'ma Zh. Tekh. Fiz. **24** (9), 66 (1998) [Tech. Phys. Lett. **24**, 359 (1998)].
7. H. Ono and N. Kawatsuki, Jpn. J. Appl. Phys. **36**, 6444 (1997).
8. N. Kamanina, S. Putilin, and D. Stasel'ko, Synth. Met. **127**, 129 (2002).
9. G. M. Zharkova and A. S. Sonin, *Liquid Crystal Composites* (VO Nauka, Novosibirsk, 1994).
10. F. Simoni, G. Cipparrone, C. Umeton, *et al.*, Appl. Phys. Lett. **54**, 896 (1989).
11. N. V. Kamanina, Opt. Spektrosk. **93**, 639 (2002) [Opt. Spectrosc. **93**, 639 (2002)].
12. L. P. Rakcheeva and N. V. Kamanina, Pis'ma Zh. Tekh. Fiz. **28** (11), 28 (2002) [Tech. Phys. Lett. **28**, 457 (2002)].
13. I. V. Rubtsov, D. V. Khudiakov, V. A. Nadtochenko, *et al.*, Chem. Phys. Lett. **229**, 517 (1994).
14. I. A. Akimov, I. Yu. Denisyuk, A. M. Meshkov, and A. V. Gorelova, Opt. Zh. **70** (2), 3 (2003).
15. N. V. Kamanina and V. I. Beredyaev, Proc. SPIE **3292**, 154 (1998).
16. N. V. Kamanina and N. A. Vasilenko, RF Patent No. 2184988 (1999).
17. L. M. Blinov, *Electro-Optical and Magneto-Optical Properties of Liquid Crystals* (Nauka, Moscow, 1978; Wiley, New York, 1983).
18. I. A. Akimov, I. Yu. Denisyuk, and A. M. Meshkov, Opt. Spektrosk. **83**, 685 (1997) [Opt. Spectrosc. **83**, 634 (1997)].

Translated by P. Pozdeev

Technical Physics Letters, Vol. 30, No. 1, 2004, pp. 4–5. Translated from Pis'ma v Zhurnal Tekhnicheskoĭ Fiziki, Vol. 30, No. 1, 2004, pp. 11–14.

The Phenomenon of Decrease in the Friction Force upon Transition to the Superconducting State

S. Sh. Rekhviashvili

Kabardino-Balkarian State University, Nalchik, Kabardino-Balkaria, Russia

e-mail: rsergo@mail.ru

Received June 3, 2003; in final form, July 15, 2003

Abstract—A simple explanation is given to the phenomenon of decrease in the friction force between an adsorbed gas film and the surface of a metal, which is observed when the metal is cooled below the superconducting transition temperature. It is pointed out that, below the critical temperature, the friction force must exhibit a characteristic extremum corresponding to the equality of the heat capacities of superconducting and normal phases. © *2004 MAIK "Nauka/Interperiodica".*

Widom and Krim [1] originally showed that the quartz crystal microbalance (QCM) technique can be used for investigating the process of friction. Previously, this method was used for monitoring the growth of thin films and for measuring the atmospheric humidity. The basic idea of this microweighing technique is that, due to adsorption from the gas phase, the resonance frequency of a special quartz crystal resonator exhibits a shift dependent on the mass of the adsorbate. The possibility of applying the QCM technique for measuring the friction force is related to the fact that, along with the shift of the resonance frequency of a quartz crystal oscillating in a gas medium, the Q value (quality factor) of this resonator also changes because of the friction between the gas and the solid surface. The characteristic slip time and the tangent (shear) stress are defined by the following expressions:

$$t_0 = (4\pi\Delta f_0 \Delta Q)^{-1}, \quad \tau = \frac{\rho v}{t_0},$$

where Δf_0 is the frequency shift, ΔQ is the change in the Q value, ρ is the surface density (mass per unit area) of the adsorbate, and v is the slip velocity.

Using the QCM technique, Dayo *et al.* [2] measured the friction force that acts on the layer of N_2 molecules adsorbed on a clean lead surface when the temperature was decreased below the superconducting transition temperature, $T < T_c$ (for lead, $T_c = 7.2$ K). These experiments revealed a sharp decrease in the friction force. It was suggested [2] that this phenomenon is probably related to the electron–phonon interaction. Persson and Tosatti [3] considered the electronic contribution to friction and pointed out that, in the framework of the electronic mechanism, it is impossible to explain the observed jumplike decrease in the friction force because the number of electrons involved in the superconducting state varies continuously. Recently, Dedkov [4] suggested that the friction can be influenced by the structure of the adsorbed nitrogen film and by the fluctuational electromagnetic interactions. However, on the whole, no unambiguous physical interpretation of this phenomenon has been given so far.

The phenomenon of decrease in the friction force upon transition to the supeconducting state can be very readily explained within the framework of general thermodynamic reasoning. In the absence of an external magnetic field, a change in the Gibbs energy of a superconductor upon the transition is described by the Gorter–Casimir equation [5]:

$$G_n - G_s = \frac{VB_c^2}{2\mu_0}, \tag{1}$$

where the indices *n* and *s* denote the normal and superconducting states, respectively; V is the volume of the superconductor; B_c is the critical value of the modulus of the magnetic induction vector; and $\mu_0 = 12.57 \times 10^{-7}$ H/m is the permeability of vacuum. The corresponding change in the shear stress can be defined as a derivative of (1) with respect to the superconductor volume,

$$\tau_n - \tau_s = \frac{d}{dV}(G_n - G_s) = \frac{B_c^2}{2\mu_0} + \frac{VB_c}{\mu_0}\frac{dB_c}{dV} = \frac{B_c^2}{2\mu_0} + \frac{S_s + S_n}{\alpha_T^{(V)}V},$$
$$S_s - S_n = \frac{VB_c}{\mu_0}\frac{dB_c}{dT}, \quad \alpha_T^{(V)} = \frac{1}{V}\frac{dV}{dT}, \tag{2}$$

where $S_s - S_n$ is the change in entropy and $\alpha_T^{(V)}$ is the temperature coefficient of the volume expansion of the superconductor.

At the point of transition to the superconducting state, we have $T = T_c$, $B_c = 0$, and $S_s - S_n = 0$; therefore,

$\tau_n - \tau_s = 0$. A decrease in the shear stress at $T < T_c$ corresponds to the condition

$$\frac{dB_c}{dV} < -\frac{1}{2}\frac{B_c}{V}. \quad (3)$$

Integrating inequality (3) and taking into account the parabolic temperature dependence of B_c, we find

$$V_0 > 0, \quad (4)$$

where V_0 is the volume of the superconductor at $T = 0$.

Condition (4) is always valid; consequently, at any temperature below T_c, we have $\tau_n - \tau_s > 0$. These results are in good agreement with the experimental data [2]. In view of the Nernst theorem, the entropy difference at $T = 0$ is $S_s - S_n = 0$. This means that, in the interval between 0 and T_c, the difference in the shear stresses must exhibit a characteristic extremum. It is evident that the position of this extremum must correspond to a point at which the heat capacities of the superconducting and normal phases are equal to each other. The existence of such an extremum also follows from experiments [2], although the authors gave no explanation to this phenomenon. In order to provide for more reliable verification of this fact, it is necessary to perform measurements for different materials in a wide temperature interval.

Now, we will obtain some numerical estimates. From (2) (as $T \longrightarrow 0$), it follows that

$$\tau_n - \tau_s = \frac{B_0^2}{2\mu_0}, \quad (5)$$

where B_0 is the critical value of the modulus of the magnetic induction vector at $T = 0$. Let us define the friction force as a critical force required to break the contact over an area Ω. For a change in this force upon transition into the superconducting state, Eq. (5) yields the following expression:

$$\Delta F = F_n - F_s = \frac{B_0^2 \Omega}{2\mu_0}. \quad (6)$$

For a single atom on a lead surface ($\Omega \sim 0.01$ nm^2 and $B_0 = 8.03 \times 10^{-2}$ T [5]), we obtain $\Delta F \approx 0.3 \times 10^{-16}$ N. This estimate can be considered quite reliable, since it coincides (on the order of magnitude) with the experimental value of the friction force acting on an atom of an inert gas near the sample surface in the normal state [4]. As for the absolute values of the shear stress measured in [2], where a change from 0.5 to 0.2 Pa took place upon the transition from the normal state to the superconducting state, these data seem to be too small. In similar experiments on measuring the friction force with a scanning probe microscope, where a nanoprobe slips over the sample surface, the shear stresses from several units to several hundred MPa were observed [6]. Such a significant difference is probably related to the fact that different friction mechanisms operate in these experiments. At present, determination of these mechanisms is a topical theoretical problem [4]. In connection with this, measurements of the friction force on superconductors (in the presence and absence of an external magnetic field) with an ultra-high-vacuum low-temperature scanning probe microscope would be of considerable interest. As far as we know, no such measurements have been performed so far.

REFERENCES

1. A. Widom and J. Krim, Phys. Rev. B **34**, R3 (1986).
2. A. Dayo, W. Alnasrallah, and J. Krim, Phys. Rev. Lett. **80**, 1690 (1998).
3. B. N. J. Persson and E. Tosatti, Surf. Sci. **411**, 855 (1998).
4. G. V. Dedkov, Usp. Fiz. Nauk **170**, 585 (2000) [Phys. Usp. **43**, 541 (2000)].
5. E. Lynton, *Superconductivity* (Methuen, London, 1969; Mir, Moscow, 1971).
6. R. W. Carpick and M. Salmeron, Chem. Rev. **97**, 1163 (1997).

Translated by Yu. Vishnyakov

Technical Physics Letters, Vol. 30, No. 1, 2004, pp. 40–41. Translated from Pis'ma v Zhurnal Tekhnicheskoĭ Fiziki, Vol. 30, No. 2, 2004, pp. 1–5.

The Electroluminescence of SiO_2 Layers with Excess Silicon

A. P. Baraban, D. V. Egorov, Yu. V. Petrov, and L. V. Miloglyadova

Institute of Physics, St. Petersburg State University, St. Petersburg, Russia

Received July 4, 2003

Abstract—We have studied the electroluminescence (EL) from Si–SiO_2 structures containing excess ion-implanted silicon in the oxide layer. The implantation of 150-keV silicon ions to doses in the range from 5×10^{16} to 3×10^{17} cm^{-2} leads to the appearance of emission bands at 2.7 and 4.4 eV in the EL spectrum, which are usually assigned to the silylene centers. It is suggested that the formation of the corresponding emission centers is directly related to the ion implantation process, irrespective of the type of implanted ions.

An important feature of the Si–SiO_2 structure is the appearance of electroluminescence (EL) in the presence of a strong electric field in the volume of the dielectric (oxide) layer [1–3]. In addition to the intrinsic EL related to peculiarities in the silicon oxide structure and the character of electron processes in this oxide, it is possible to observe the phenomenon of induced EL upon intentional introduction of additional emission centers into the SiO_2 layer [1]. One possible method for the creation of such emission centers is ion implantation [4]. The Si–SiO_2 structures are the basis of modern microelectronics and, hence, obtaining stable EL in this system is of considerable importance for further development in this field and especially in optoelectronics.

Here, we report on the results of investigation of the EL from Si–SiO_2 structures with the oxide layer containing excess silicon introduced by ion implantation.

The SiO_2 layers with a thickness of 800 nm on *p*-Si substrates were obtained by thermal oxidation in oxygen at 1100°C. Then, silicon ions were implanted into the oxide layer at an energy of 150 keV to a dose in the range from 5×10^{16} to 3×10^{17} cm^{-2}. This dose range corresponds to an additional silicon content from 5 to 30% in the region of implant localization, with a maximum of the excess silicon content occurring at a depth of ~200 nm from the oxide layer surface.

The EL spectra were measured in the electrolyte–dielectric–semiconductor system using a method described in detail elsewhere [1]. One advantage of studying the EL in this system is the ability to study the electron injection and acceleration in SiO_2 layers in a broad range of the electric field strength (the field is a necessary condition for the EL excitation). An additional advantage is the ability to remove the silicon oxide by controlled electrochemical etching in the course of EL measurements, which provides data on the distribution of emission centers across the oxide layer. The EL spectra were measured at 273 K under the conditions excluding impact ionization in the silicon oxide volume [5].

Figure 1 shows the EL spectra of the initial Si–SiO_2 structure and the samples containing excess ion-implanted silicon, measured under identical excitation conditions. As can be seen, the ion implantation of silicon into the oxide layer leads to a significant increase in the integral intensity of emission, which is related to the appearance of two additional EL bands with the peaks at 2.75 ± 0.05 and 4.4 ± 1.1 eV. The bands are well described by the Gaussian function with a full width at half maximum of 0.45 ± 0.05 and 0.6 ± 0.2 eV, respectively. The intensities of these bands exhibited exponential growth with increasing electric field strength in the oxide. At a constant field strength, the intensity decayed with time according to the law $L(t) = A_0 + A_1\exp(-t/\tau_1) + A_2\exp(-t/\tau_2)$, where $\tau_1 = 60$ s, $\tau_2 = 600$ s, and A_0, A_1, and A_2 are constant coefficients.

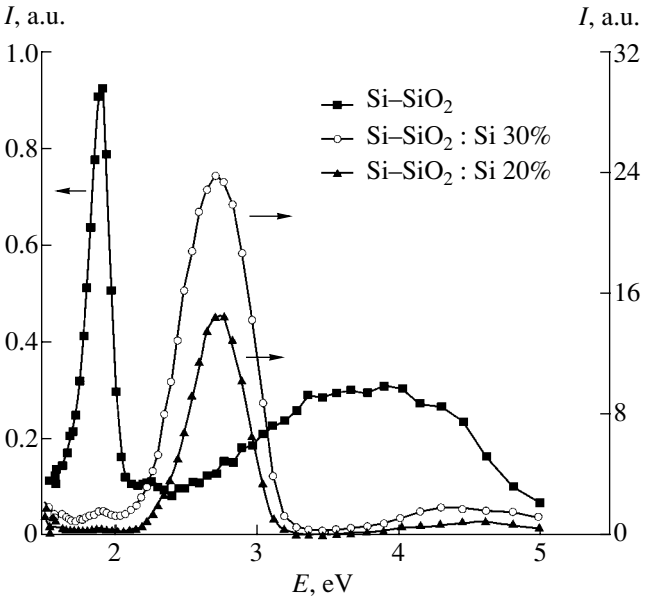

Fig. 1. The EL spectra of initial Si–SiO_2 structures and those containing different amounts of ion-implanted silicon in the oxide layer.

1063-7850/04/3001-0040$26.00 © 2004 MAIK "Nauka/Interperiodica"

An increase in the content of ion-implanted excess silicon in the oxide layer also leads to simultaneous growth in the intensity of EL bands at 2.7 and 4.4 eV, whereby their intensity ratio remains constant. The EL measurements in the course of layer-by-layer removal of the oxide showed that the emission centers responsible for the EL at 2.75 ± 0.05 and 4.4 ± 1.1 eV occur at a distance not exceeding 550 nm from the Si–SiO_2 interface. The band of emission at 1.9 eV characteristic of the initial Si–SiO_2 structures is also retained in the presence of excess silicon (Fig. 1), but the intensity of this band in the latter case is lower than that before ion implantation. It should also be noted that the EL spectrum of ion-implanted structures in the near-UV range ($h\nu > 3.5$ eV) also contains a contribution due to the emission characteristic of unimplanted Si–SiO_2 structures [1]. This distorts the shape of the induced EL band at 4.4 eV, especially on the side of higher excitation energies (i.e., greater electric field strengths in the oxide layer).

The implantation of ions into the oxide layer is accompanied by dissipation of their energy in the course of interaction with the nuclear and electron subsystems of the target. This leads to the intensive formation of defects in the oxide layer that accounts for the modification of the EL spectrum manifested by the appearance of emission bands at 2.7 and 4.4 eV. It should be noted that the ion implantation of argon to a dose of 10^{13}–3×10^{17} cm^{-2} into the Si–SiO_2 structure studied previously [6] led to qualitatively similar changes in the EL spectrum, giving rise to the intense emission bands at 2.7 and 4.4 eV. The appearance of these bands was explained [7] by the formation of implantation-induced defects representing oxygen atoms doubly coordinated to silicon. Such silylene centers are characterized by the radiative transitions at 2.7 and 4.4 eV excited at 5 eV [8].

We believe that changes in the EL spectrum observed in our samples upon implantation are also related to the formation of silylene centers in the volume of silicon oxide. However, the formation of silylene centers in silicon-implanted samples can take place not only due to the displacement of atoms in the SiO_2 lattice (as in the case of argon-bombarded Si–SiO_2 structures) but due to the introduction of additional silicon atoms as well. The fact that most of the emission centers are localized closer to the Si–SiO_2 interface as compared to a maximum in the distribution of implanted silicon ions suggests that atomic displacements in the SiO_2 lattice still play a significant role in the formation of silylene centers. On the other hand, the fact that the intensity of the EL band at 2.7 eV observed upon the implantation of silicon is greater than that upon the implantation of argon to the same dose (Fig. 2) is evidence of the direct participation of implanted silicon in the formation of silylene centers. The excitation of emission from the implantation-induced centers in both cases takes place due to their interaction with hot electrons possessing an energy above 5 eV. This is indicated by exponential dependence of the intensity of the EL bands at 2.7 and 4.4 eV on the electric field strength in silicon oxide.

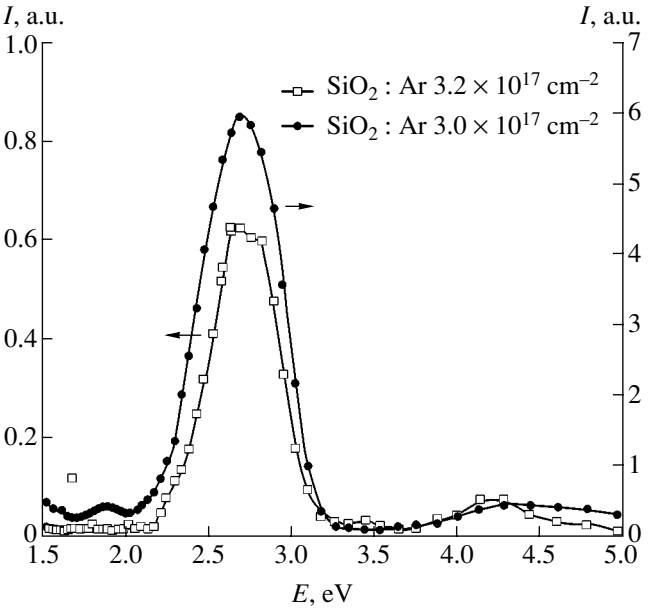

Fig. 2. The EL spectra of Si–SiO_2 structures with the oxide layers implanted with argon or silicon ions.

In conclusion, the implantation of silicon ions into the oxide layer of Si–SiO_2 structures leads to the formation of defects representing oxygen atoms doubly coordinated to silicon, which serve as the effective centers of electroluminescence. The formation of such defects is inherent in the process of ion implantation and, to the first approximation, is independent of the type of implanted ions.

Acknowledgments. This study was supported by the Ministry of Defense of the Russian Federation, project no. PD02-1.2-356.

REFERENCES

1. A. P. Baraban, V. V. Bulavinov, and P. P. Konorov, *Electronics of SiO_2 Layers on Silicon* (LGU, Leningrad, 1988).
2. P. Solomon and N. Klein, J. Appl. Phys. **47**, 1023 (1976).
3. A. J. Pepe, W. Chen, and M. Oyler, J. Electrochem. Soc. **140**, 1090 (1993).
4. L. Rebohle, J. Borany, R. A. Yankov, *et al.*, Appl. Phys. Lett. **71**, 2809 (1997).
5. A. P. Baraban, I. V. Klimov, N. I. Tenoshvili, *et al.*, Pis'ma Zh. Tekh. Fiz. **15** (17), 44 (1989) [Sov. Tech. Phys. Lett. **15**, 680 (1989)].
6. A. P. Baraban, P. P. Konorov, L. V. Malyavka, and A. G. Troshikhin, Zh. Tekh. Fiz. **70** (8), 87 (2000) [Tech. Phys. **45**, 1042 (2000)].
7. A. P. Baraban and L. V. Miloglyadova, Zh. Tekh. Fiz. **72** (5), 56 (2002) [Tech. Phys. **47**, 569 (2002)].
8. L. N. Skuya, A. N. Streletskiĭ, and A. B. Pakovich, Fiz. Khim. Stekla **14**, 481 (1988).

Translated by P. Pozdeev

Technical Physics Letters, Vol. 30, No. 1, 2004, pp. 42–44. Translated from Pis'ma v Zhurnal Tekhnicheskoĭ Fiziki, Vol. 30, No. 2, 2004, pp. 6–11.

X-ray Interference Effects in Thin Equiatomic Co–Pt Single Crystal Films

P. D. Kim*, S. V. Stolyar, R. S. Iskhakov, I. A. Turpanov, V. I. Yushkov, A. Ya. Beten'kova, G. N. Bondarenko, and A. M. Makhlaev

Kirensky Institute of Physics, Siberian Division, Russian Academy of Sciences, Krasnoyarsk, Russia

Krasnoyarsk State University, Krasnoyarsk, Russia

Krasnoyarsk State Technical University, Krasnoyarsk, Russia

Institute of Chemistry and Chemical Technology, Siberian Division, Russian Academy of Sciences, Krasnoyarsk, Russia

** e-mail: kim@iph.krasn.ru*

Received May 26, 2003

Abstract—Thin single crystal films of an equiatomic $Co_{50}Pt_{50}$ alloy synthesized by magnetron sputtering on a MgO single crystal substrate were studied by X-ray diffractometry. Interference oscillations with a period depending on the Co–Pt alloy film thickness were observed in the region of (001) reflection, characterizing the $L1_0$ type ordering, and in the region of small diffraction angles ($2\Theta < 10°$). *© 2004 MAIK "Nauka/Interperiodica".*

Thin magnetic films of equiatomic alloys such as CoPt, FePt, and FePd are considered as potential high-density magnetic data recording media. The hysteresis behavior of these alloys is related to the formation of an ordered uniaxial magnetic superstructure of the $L1_0$ type [1]. One of the main conditions for the use of such films as magnetic recording media is the homogeneity of composition: this very property provides for the constant tetragonal $L1_0$ type superstructure and, hence, for the absence of fluctuations in the crystallographic anisotropy field. Another critical condition is the constant film thickness over the entire area that ensures the absence of magnetostatic charges on the surface. The third important condition for the use of thin films as magnetic recording media with perpendicular magnetic anisotropy is a monodomain character, that is, the presence of a single domain in the magnetic structure, with the tetragonal axis *C* in the whole film volume being parallel to the normal to the film surface.

In order to check that all these conditions are fulfilled, it is necessary to develop integral methods sensitive to homogeneity of the synthesized films. One such method could be the X-ray diffractometry of thin single crystal films, which can readily detect thickness-related oscillations in the interference contrast provided that the above conditions are valid. The problem of quality monitoring is now of considerable importance for thin films (made of semiconductors, superconductors, etc.) used in microelectronics [2].

The samples of thin $Co_{50}Pt_{50}$ single crystal films were obtained by magnetron sputtering in an argon atmosphere at a pressure of 2.7×10^{-2} Pa. In order to avoid chemical inhomogeneity, the films were synthesized by deposition of alternating Co and Pt layers. The deposition time τ_i was selected so as to provide that each layer would be one atomic monolayer thick. The total deposited layer thickness *d* was varied from 2 to 20 nm. The films were deposited onto (001)-oriented MgO singe crystal substrates. The thickness d_0 and the chemical composition of each film were determined by X-ray fluorescence measurements. Isothermal annealing of the films was performed in a vacuum chamber at a pressure not exceeding 6.7×10^{-4} Pa.

The sample structure was studied at room temperature by X-ray diffraction on a DRON-4 diffractometer using CuK_α radiation ($\lambda = 0.154$ nm) from an X-ray tube operating at $U = 32$ kV, $I = 32$ mA. The measurements were performed using a two-crystal scheme with flat and bent crystal monochromators with Soller slit widths of 2 mm (vertical) and 6 mm (horizontal) and an output vertical slit width of 0.25 mm. The diffraction angle was scanned at a rate of 1 deg/min with an 0.02° detector angle step in the automated regime.

Figure 1 shows a large-angle X-ray diffraction pattern for a 7-nm-thick $Co_{50}Pt_{50}$ film annealed for 3 h at $T = 873$ K. As can be seen, the region of the (001) reflection characterizing the ordered $L1_0$ superstructure displays thickness-related oscillations of the interfer-

1063-7850/04/3001-0042$26.00 © 2004 MAIK "Nauka/Interperiodica"

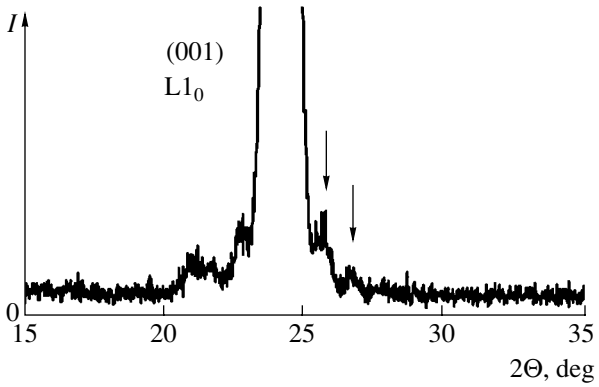

Fig. 1. Typical large-angle X-ray diffraction pattern for a 7-nm-thick $Co_{50}Pt_{50}$/MgO film annealed for 3 h at T = 873 K.

ence contrast. According to the experimental [2, 3] and theoretical [4] data, the full width at half maximum (FWHM) of the central peak equals the oscillation period, while the distance from the central maximum to the first satellite reflection is one and a half times the FWHM value (Fig. 1). The thickness contrast measurements for $Co_{50}Pt_{50}$ films show evidence of a homogeneous thickness and confirms the high quality of the films obtained by magnetron sputtering.

The film thickness can be estimated from these data using the well-known Selyakov relation [4] modified for the case when the diffraction vector is perpendicular to the surface of a plane-parallel crystal plate:

$$d = \lambda/\Delta(2\Theta)\cos\Theta. \quad (1)$$

Here, λ is the wavelength, Θ is the Bragg angle, and $\Delta(2\Theta)$ is the period of oscillations of the thickness contrast.

Figure 2 presents a small-angle diffraction pattern for a 12-nm-thick $Co_{50}Pt_{50}$ film after isothermal annealing for 3 h at 873 K, also clearly displaying interference oscillations. It should be noted that the thickness contrast oscillations in as-prepared films were observed as well. The small-angle diffraction pattern with equidistance peaks (Fig. 2) is due to the interference of X-rays reflected from the outer (air–metal interface) and inner (film–MgO substrate interface) surfaces of the film. For this reason, the values inverse to the wave vectors $k = \sin\Theta/\lambda$ are proportional to the film thickness d_0.

The small-angle diffraction pattern can also be used for evaluation of the film thickness. Indeed, the distance between neighboring reflections obeys the Bragg condition $2d\sin\Theta = n\lambda$. Assuming that $\sin\Theta = \Theta$ for small angles, we obtain the formula for the film thickness

$$d = \lambda/\Delta(2\Theta), \quad (2)$$

where $\Delta(2\Theta)$ is the period of oscillations. This formula is a particular case of the Selyakov expression (1) for the region of small diffraction angles ($\cos\Theta = 1$).

Figure 3 shows the plot of d_0 versus the ratio $\lambda/\Delta(2\Theta)$. As can be seen, the experimental points fit to the bisector of the right angle well. Estimates show that the effect of interference oscillations will not be manifested at a film surface roughness on the order of ±1 nm.

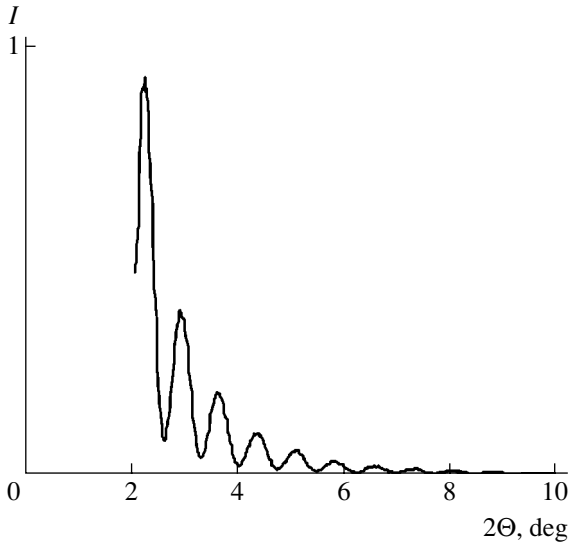

Fig. 2. Typical small-angle X-ray diffraction pattern for a 12.7-nm-thick $Co_{50}Pt_{50}$/MgO film annealed for 3 h at T = 873 K.

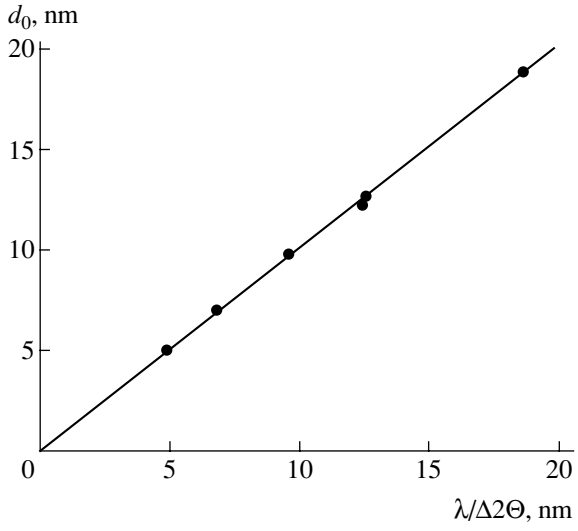

Fig. 3. A plot of the $Co_{50}Pt_{50}$/MgO film thickness (d_0) determined from X-ray fluorescence data versus the thickness $d_0 = \Delta(2\Theta)$ estimated from small-angle X-ray diffraction patterns.

To summarize, we have studied the peculiarities of X-ray diffraction from $Co_{50}Pt_{50}$/MgO structures, where the $Co_{50}Pt_{50}$ single crystal film obtained by magnetron sputtering has a disordered fcc structure in the as-prepared state and acquires an $L1_0$ superstructure upon thermal treatment. The presence of oscillations in the interference contrast is evidence of a high homogeneity of the film thickness. This effect provides a very good method for checking the morphological homogeneity of thin metal films used in microelectronics.

REFERENCES

1. N. I. Vlasova, G. S. Kandaurova, and N. N. Shchegoleva, Fiz. Met. Metalloved. **90** (3), 31 (2000).
2. Yu. N. Drozdov, L. D. Moldavskaya, and A. E. Parafin, Poverkhnost, No. 10, 13 (1989).
3. G. F. Kuznetsov, Kristallografiya **40**, 936 (1995) [Crystallogr. Rep. **40**, 869 (1995)].
4. V. I. Iveronova and G. P. Revkevich, *X-ray Scattering Theory* (Mosk. Gos. Univ., Moscow, 1987).

Translated by P. Pozdeev

Technical Physics Letters, Vol. 30, No. 1, 2004, pp. 45–47. Translated from Pis'ma v Zhurnal Tekhnicheskoĭ Fiziki, Vol. 30, No. 2, 2004, pp. 12–16.

Determination of the Liquid Drop Profile on a Solid Surface

V. Z. Kanchukoev

Kabardino-Balkarian State University, Nalchik, Kabardino-Balkaria, Russia

e-mail: vlad-kan@yandex.ru; exp@kbsu.ru

Received July 2, 2003

Abstract—The variational problem of determining the capillary surface of a sessile liquid drop on a solid surface is solved and the solution is analyzed. © *2004 MAIK "Nauka/Interperiodica".*

The results of theoretical and experimental investigations of the statics and dynamics of a small sessile liquid drop on a solid surface, especially in the three-phase contact region, provide valuable information necessary for the solution of many basic and practical problems [1–3]. Achievements in the theory of minimal surfaces, on the one hand, and demands of the aerospace and medicinal technologies, on the other hand, have stimulated a new wave of investigations in several directions of the theory of capillary phenomena [4].

Consider a drop of a viscous liquid with the volume V, freely resting on the horizontal surface of a homogeneous solid under the action of gravity directed downward along the z axis. Let ρ_i be the known densities of contacting phases, and σ_{ij}, the specific free surface energies at the interfaces between ith and jth phases (the indices $i, j = 1, 2, 3$ referring to solid, liquid, and ambient medium, respectively), such that the system obeys the relation

$$0 < \arccos[(\sigma_{13} - \sigma_{12})/\sigma_{23}] \le \pi/2. \tag{1}$$

The shape of the symmetric capillary surface will be determined by the well-known variational method used previously [5, 6] for obtaining an approximate analytical solution of this problem.

Let $z = f(x, h_0)$ be a solution describing the shape of the capillary surface and h_0 be the central height of the drop (unknown parameter). Since the drop surface can be considered as axisymmetric, the total energy of the liquid drop–solid substrate system per unit length of the drop contour can be expressed as [5]

$$W(x_f) = \int_{-x_f}^{x_f} \left[\sigma_{23}\left(\sqrt{1 + f_x^2} + \frac{f^2}{2a^2}\right)\right]dx + 2x_f(\sigma_{12} - \sigma_{13}). \tag{2}$$

Here, x_f is the unknown abscissa of the drop front (base radius), $a^2 = \sigma_{23}/g(\rho_2 - \rho_3)$ is the capillary constant, and g is the acceleration of gravity.

Consider the manifold M of functions (curves) $f(x, h_0)$ obeying the following conditions:

(i) The functions $f(x, h_0)$ are continuously differentiable on a certain finite segment Δ, the internal points of which are the values $x = \pm x_f$ (i.e., $f(x, h_0) \in C^1[\Delta]$), $[-x_f, x_f] \subset \Delta$.

(ii) The ends of these curves obey zero boundary conditions:

$$\begin{aligned} f(x, h_0) &= 0, \quad x = -x_f; \\ f(x, h_0) &= 0, \quad x = x_f. \end{aligned} \tag{3}$$

(iii) The functions $f(x, h_0)$ obey a nonlocal boundary condition

$$\int_{-x_f}^{x_f} f(x, h_0)dx = S_0. \tag{4}$$

This relation (written taking into account the rotational symmetry of the surface under consideration) reflects the fact that the drop cross section area is constant:

$$S_0 = \sqrt[3]{9\pi/16}V^{2/3} = k_0V^{2/3}. \tag{5}$$

Now, let us define a functional J on the manifold M, such that

$$J[f] = \int_{-x_f}^{x_f} F(f, f_x)dx + 2(\sigma_{12} - \sigma_{13})x_f, \tag{6}$$

where $F = \sigma_{23}(\sqrt{1 + f_x^2} + f^2/(2a^2)) - \lambda f$ is the function possessing continuous partial derivatives up to the sec-

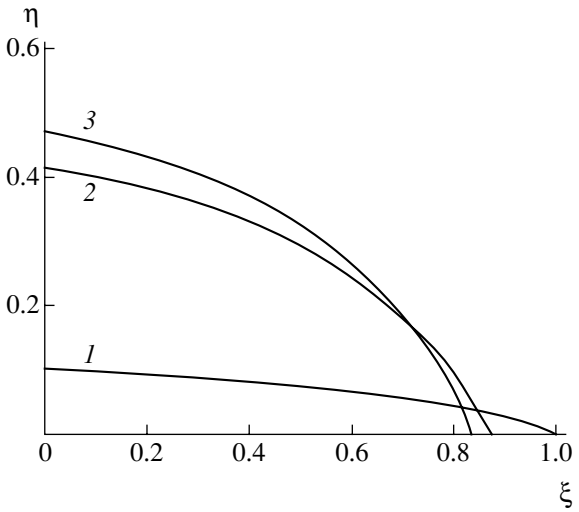

The profiles of sessile drops of various liquids on a brass surface (in dimensionless variables): (*1*) ethanol; (*2*) water; (*3*) glycerol.

ond order with respect to both variables and λ is an unknown variation parameter.

Any function $f(x, h_0) \in M$ corresponding to an extremum of functional (6) can be readily seen to obey the Euler condition

$$Lf \equiv \frac{d}{dx}\left[\frac{f_x}{\sqrt{1+f_x^2}}\right] - \frac{f}{a^2} + \lambda = 0, \quad -x_f < x < x_f, \quad (7)$$

and the transversality condition

$$\begin{aligned}&(F - f_x F_{f_x})\big|_{x=-x_f}\\ &+ 2(\sigma_{12} - \sigma_{13}) + (F - f_x F_{f_x})\big|_{x=x_f} = 0.\end{aligned} \quad (8)$$

Then, using the substitution

$$U = 2a^2\cos\theta_s + 2\lambda a^2 f - f^2 > 0, \quad (9)$$

the problem can be reduced to solving the ordinary differential equation

$$\begin{aligned}&\frac{dU}{dx} - \operatorname{sgn} x\left(\frac{2}{U}(2a^2 - U)\sqrt{2a^2 + U}\right) = 0,\\ &-x_f < x < x_f,\end{aligned} \quad (10)$$

with boundary conditions (3) for $\lambda = h_0/a^2$ and $h_0 = a\sqrt{2(1-\cos\theta_s)}$.

Taking into account the symmetry of the problem under consideration, the equation of the free surface profile of the liquid drop can be written as

$$\sqrt{1 - (\eta - \eta_0)^2} - \psi(\eta) = \xi - \xi_0, \quad (11)$$

where

$$\eta_0 = h_0/(2a) = \sin(\theta_s/2), \quad \eta = f/(2a),$$
$$0 \le \eta < \eta_0,$$

$$\xi_0 = -x_f/(2a)$$
$$= -(0.5\cos(\theta_s/2) + k_0 V^{2/3}/(8a^2\sin(\theta_s/2))),$$

$$\xi = -x/(2a), \quad \xi_0 \le \xi < 0.$$

This representation of a solution to the problem under consideration shows that $\psi(\eta)$ is a function characterizing deviation of the contour of the capillary surface of the drop from a semicircle of unity radius with the center at a point with the coordinates (ξ_0, η_0).

It should be noted that there exists a certain critical value of the liquid drop volume V_C [3, 5, 6] above which the drop height ceases to increase: for $V > V_C$, the extremal drop height h_0 remains constant. This critical volume can be determined using boundary condition (4), which yields

$$V_C = \frac{4}{3\sqrt{\pi}}\left(\frac{2\sigma_{23}}{g(\rho_2 - \rho_3)}\sin\theta_s\right)^{3/2}. \quad (12)$$

Further increase in the drop volume only leads to an increase in the area of contact between liquid and solid and in the area of a plateau. As a result, the drop becomes more like a disk and there appears a sign by which the drop can be distinguished from a thin layer of liquid freely spreading over the solid surface.

Since the height of the liquid layer for $V \ge V_C$ remains constant, the extremal height h_0 can be considered as the equivalent free liquid layer thickness δ on a solid surface.

For an analysis of the results formulated above, we have used formula (11) to calculate the profiles of capillary surfaces of a critical sessile drop for various liquids on a solid surface. Some results are presented in the figure. The results of these calculations showed that, as the wetting ability of the liquid increases, the central height of the drop (at a constant volume) decreases, while the base radius (or the area wetted by liquid) increases. It should be noted that Eq. (11) also describes the profile of the capillary surface of a drop of nonspreading liquid.

The obtained exact solution of the problem of determining the capillary surface of a liquid partly wetting the solid surface is also important for solving the inverse problems, whereby the linear dimensions of an equilibrium drop surface are used to determine the physicochemical parameters of the system (σ_{ij}, θ_s, a^2, etc.). For example, the known values of h_0 and a can be

used to determine the equilibrium wetting angle by the formula

$$\theta_s = 2\arcsin\left(\frac{h_0}{2a}\right) \quad (13)$$

using a method described in [7].

An analysis of the results described above showed that they are qualitatively and quantitatively consistent with the published data and can be used for solving various applied problems related to the physics and chemistry of surface phenomena.

Acknowledgments. This study was supported by the Russian Foundation for Basic Research, project no. 03-02-96010.

REFERENCES

1. B. D. Summ and Yu. V. Goryunov, *Physicochemical Principles of Wetting and Spreading* (Khimiya, Moscow, 1976).
2. P. G. De Gennes, Rev. Mod. Phys. **57**, 227 (1985).
3. A. I. Rusanov and V. A. Porkhaev, *Interphase Strain Metering* (Khimiya, St. Petersburg, 1994).
4. R. Finn, *Equilibrium Capillary Surfaces* (Springer-Verlag, New York, 1986; Mir, Moscow, 1989).
5. Ya. Frenkel', Zh. Éksp. Teor. Fiz. **18**, 659 (1948).
6. E. I. Nesis, V. I. Tokmakov, and T. S. Chigareva, Izv. Akad. Nauk SSSR, Énerg. Transp., No. 2, 146 (1967).
7. I. I. Markov, M. V. Baturin, and A. A. Khashchenko, RF Patent No. 2170921, Byull. Izobret., No. 20 (2001).

Translated by P. Pozdeev

Technical Physics Letters, Vol. 30, No. 1, 2004, pp. 48–50. Translated from Pis'ma v Zhurnal Tekhnicheskoĭ Fiziki, Vol. 30, No. 2, 2004, pp. 17–24.

X-ray Diffraction Study of the Effect of Photohardening on the Structure of Self-developing Dichromated Gelatin Sensitized with Methylene Blue

Yu. S. Zagaĭnova* and S. S. Kolesnikov

Irkutsk State University, Irkutsk, Russia

** e-mail: yuliazagainova@mail.ru*

Received June 10, 2003

Abstract—Peculiarities of the structural organization of self-developing emulsion layers based on dichromated gelatin sensitized with Methylene Blue dye and containing 76% water have been studied by X-ray diffraction. The diffraction patterns $I(2\theta)$ of the photolayers are presented. The scattering functions of the amorphous state have been calculated. Differences between the photolayer structures in the exposed and unexposed state are considered. It is shown that recording an image leads to ordering of the photolayer structure that is related to changes in the conformations of gelatin macromolecules. *© 2004 MAIK "Nauka/Interperiodica".*

Introduction. The process of photohardening of self-developing emulsions based on dichromated gelatin sensitized with Methylene Blue and containing 76% water leads to the appearance of certain peculiarities in the structural organization of this medium. Considering the characteristics of recorded holograms, it is necessary to take into account, besides the primary photochemical processes, some features of the structure and changes in the conformations of gelatin macromolecules in the photolayer.

Investigations of the structure of collagen-type proteins by X-ray diffraction and electron microscopy show that these macromolecules contain both ordered (crystalline) and disordered (amorphous) regions. The structural features of collagenous proteins, as determined by their amino acid composition, allow these proteins to be separated into a group of fibrillar proteins belonging to the keratin–myosin–fibrinogen type [1, 2]. The amino acid residues participate in stabilization of the intramolecular structure of gelatin molecules and are involved in intermolecular hydrogen bonds, thus forming the quaternary conformation state of macromolecules.

Characteristic signs of the X-ray diffraction pattern of proteins of the collagen type are the presence of an intensity maximum with $s/2 = 2.86$ Å, a strong reflection with $s/2 = 11.4$ Å, and a diffuse maximum with $s/2 = 4.6$ Å (s is the coordinate in the reciprocal space). It is commonly accepted that the interference maxima with $s/2 = 2.86$ Å correspond to the length of a single amino acid residue, while the interplanar spacings $d = 11.4$ and 4.6 Å correspond to the distances between side chains of amino acid residues arranged at right angles to the polypeptide chain [1, 3]. The patterns of X-ray diffraction from gelatin emulsions also display the characteristic diffuse peaks at $s/2 = 4.6$ and 11.2 Å, which is evidence of the presence of regions in the helix and coil conformations in the structure of gelatin layers. On the other hand, the dominating structural conformation is determined not only by the gelatin concentration but depends on the pH and ionic strength of solution, the temperature, and the presence of hardening agents (metal ions and/or neutral salts).

The aim of this study was to reveal changes in the emulsion layer structure arising in the course of holographic recording, depending on the parameter s of synthesis, water content, and photohardening.

Experimental. We have studied laminar self-developing emulsion layers based on dichromated gelatin sensitized with Methylene Blue. The layers were synthesized using photographic gelatin preliminarily dissolved for 1 h in distilled water at $T = 22$°C. The emulsion solution was prepared at $T_1 = 43$°C. To the aqueous gelatin solution were sequentially added glycerol, ammonium bichromate, and 0.001% aqueous solution of Methylene Blue dye. The solution was poured into a flat cell with the height (2 mm) determining the emulsion layer thickness. The photolayer formation time was 24 h at $T_2 = 15$°C.

The diffraction efficiency as a function of the exposure energy E was studied in a holographic setup for recording plane wave holograms. The holograms were projected by the method of amplitude division [4]. The radiation source was a He–Ne laser (LG-220) with a power of $P_L = 20$ mW. The holograms were recorded with a spatial frequency of ~800 lines/mm. The diffraction efficiency was measured using a silicon photodiode (FD-7K).

The photolayer structure dynamics depending on the water content was studied by measuring X-ray diffraction at large angles in the transmission and reflec-

1063-7850/04/3001-0048$26.00 © 2004 MAIK "Nauka/Interperiodica"

tion modes. The measurements were performed on a DRON-3R diffractometer using CuK_α radiation focused according to the Bragg–Brentano scheme. The diffraction patterns $I(2\theta)$ were automatically recorded in a continuous detector scan mode. In addition, the photolayer structure was studied by the phototechnique described in [5–7]. Using the normalized intensity curves $I(2\theta)$, we calculated the correlation curves of the radial distribution of atomic scattering centers in the diffraction medium $f(r) = 4\pi r^2(z(r) - z_{av}(r))$ [5–7].

Results and discussion. For the given conditions of synthesis and an emulsion layer thickness of 2 mm, the maximum diffraction efficiency (DE_{max}) was 45% at an exposure energy of $E = 40$ mJ/cm^2. This is 32% higher than the DE_{max} values obtained for 2-mm-thick holograms with a spatial frequency of 800 (lines/mm) recorded using the emulsion media reported earlier [2].

The X-ray diffraction measurements revealed peculiarities in the structural organization of photolayers before recording holograms and showed changes related to the exposure. For this purpose, all samples were characterized by the diffraction patterns $I(2\theta)$ in the transmission and reflection modes (Fig. 1). Both the large-angle X-ray diffraction measurements and the phototechnique showed that photolayers possess a fully amorphous structure. However, a comparison of the $I(2\theta)$ curves of exposed and unexposed photolayers revealed significant changes in the structural organization of emulsion caused by the exposure. The curves display three diffusion peaks at $2\theta_1 = 9.4°$, $2\theta_2 = 27.3°$, and $2\theta_3 = 42°$ (Fig. 1). The presence of diffuse reflections is evidence of equilibrium disorder in all directions. A decrease in the intensity and halfwidth of the diffuse peak at $2\theta_1$ in the diffraction pattern of exposed samples is indicative of some ordering in the system in the course of exposure to HE–Ne laser radiation. This is accompanied by a decrease in halfwidth of the peak at $2\theta_2$.

The above changes are more pronounced in the diffraction patterns of emulsion layers measured in the reflection mode. This fact suggests that holographic recording leads to changes in the emulsion structure predominantly in the planes parallel to the surface of a photolayer (or a substrate on which the layer was formed). These changes depend on the parameters of synthesis. In particular, the diffuse peak at $2\theta_3$ was not detected for the photolayers synthesized under conditions other than those indicated above. The maximum diffraction efficiency of holograms recorded with a spatial frequency of 800 lines/mm in the layers obtained under different conditions decreases by half.

Let us consider the distributions of average interatomic distances r_i in the photolayers, as described by the correlation functions calculated from the diffraction intensity curves $I(2\theta)$. The uncertainty of determination of these distances (Fig. 2) depends on the instrumental error and the limited character of experimental data. In

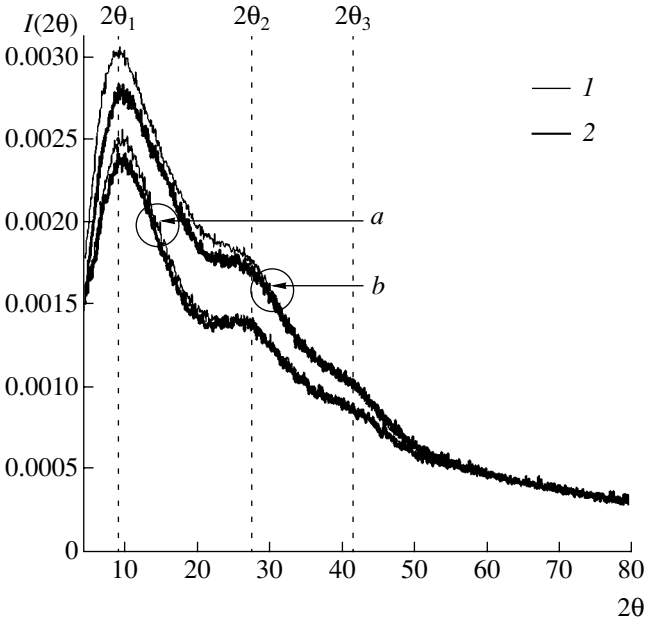

Fig. 1. X-ray diffraction intensity $I(2\theta)$ in the (*a*) reflection and (*b*) transmission mode in self-developing emulsion layers based on dichromated gelatin sensitized in the red spectral range: (*1*) before exposure; (*2*) after exposure.

our case, the average interatomic distances exceeding $r \sim 15$ Å are insufficiently reliable and have to be rejected. The results of measurements in transmission mode revealed no changes in r_i upon exposure. Below, the effect of photohardening on the emulsion layer structure is considered as revealed by the diffraction patterns of exposed and unexposed samples measured in the reflection mode. The scattering functions for the initial samples measured in both transmission and reflection modes give the following average distances r_i (Å): $r_1 = 0.7$; $r_2 = 1.7$; $r_3 = 3$; $r_4 = 4.2$; $r_5 = 5$; $r_6 = 7$; $r_7 = 9.1$; $r_8 = 11.2$; $r_9 = 12.7$; $r_{10} = 13.7$; $r_{11} = 15$ (Fig. 2).

Now, let us proceed to the scattering function for exposed samples, determined from the results of measurements in the reflection mode (Fig. 2). Similar to the transmission data, the values of r_1 and r_2 are observed as well. It should be noted that these values of r_i are observed for all jelly emulsions based on aqueous gelatin solutions, while being absent in the case of dry emulsions. Our experimental data and the results reported by other researchers on the structure of water under normal conditions [5, 6] allow the r_1 and r_2 values to be interpreted as reflecting the contribution from "bulk" water molecules [8] present in the photolayer and/or from a hydration shell formed as a result of the interaction between solvent (water) and gelatin molecules.

Taking into account the chemical formula of gelatin macromolecules [9] and using the table of atomic radii [10], the distance r_3 is assigned to the peptide chain sequence –N–C–C– frequently repeated along the gel-

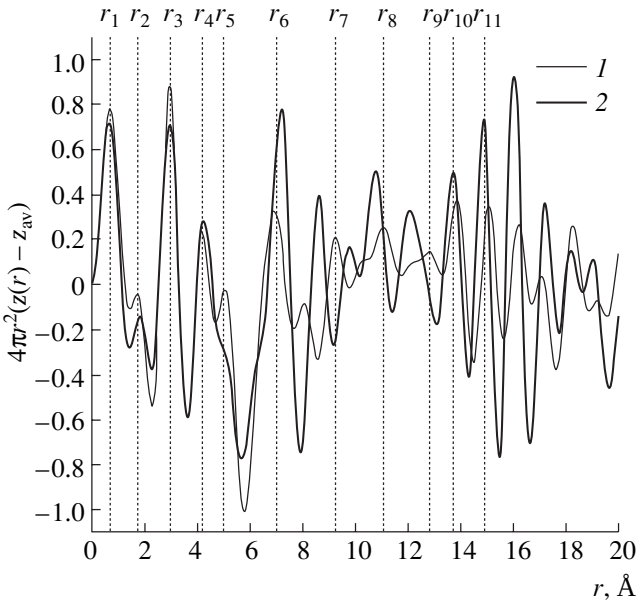

Fig. 2. Correlation curves of the radial distribution of atomic scattering centers in the reflection mode in the gelatin emulsion layers (*1*) before and (*2*) after holographic recording.

atin molecule. In the literature, the value of r_4 is usually attributed to the distance between amino acid residues [3, 11], but we would prefer to assign this distance to the peptide chain sequence –N–C–N– because nitrogen forms stable chemical bonds with amino acid residues. The distances r_1–r_4 observed in both transmission and reflection modes for the initial and exposed samples confirm the above conclusion concerning the amorphous state of substance in the emulsions under consideration.

Now, let us consider the differences between correlation functions calculated for the unexposed and exposed emulsion layers. It is assumed [2] that the maturation of emulsions under the conditions described above leads to the formation of gelatin macromolecules occurring predominantly in the state of α helix with a period of about 5 Å. Holographic recording in the layers of dichromated gelatin involves the primary photochemical processes [1] and secondary changes in the molecular conformation or a photostimulated phase transition of the helix–coil type [2]. For this reason, we assign the distance r_5 (Fig. 2) to gelatin molecules in the helical conformation. This distance is not revealed by diffraction in the reflection mode. This fact indicates that, besides secondary changes in the conformation, the parts of gelatin molecules of the α-helix type involved in the recording are spent predominantly in the photolayer planes parallel to the substrate plane.

As for the behavior of $f(r)$ in the interval of $r_i \in (6; 14)$ Å, these average interatomic distances in exposed samples shift toward lower values (Fig. 2). This is related to the decrease in the spacing between neighboring gelatin molecules upon recording as a result of photohardening. It should also be noted that the $f(r)$ curve for r_i obtained in the transmission mode decreases in intensity upon the exposure. This is evidence of a redistribution of "bulk" water in the curse of holographic recording in self-developing emulsion layers based on dichromated gelatin.

Conclusions. The X-ray diffraction investigation of thick self-developing emulsion layers based on dichromated gelatin sensitized in the red spectral range showed that this medium possesses a fully amorphous structure. Exposure of the samples to radiation of a He–Ne laser leads to ordering predominantly in the planes parallel to the surface of a photolayer (or a substrate on which the layer was formed). The correlation analysis of the diffraction curves reveals intrastructural changes related to the redistribution of "bulk" water in the emulsion layer in the course of exposure. These changes probably account for a modification of the refractive index profile necessary for the holographic recording.

REFERENCES

1. A. I. Kryukov, V. P. Sherstyuk, and I. I. Dilung, *Phototransfer of Electrons and Applied Aspects* (Naukova Dumka, Kiev, 1982).
2. A. G. Konop, S. P. Konop, and A. N. Malov, *Holographic Methods in Science and Technology* (Yaroslavl. Gos. Pedagog. Univ., Yaroslavl, 1977), pp. 115–123.
3. B. K. Vaĭnshteĭn, *X-ray Diffraction on Chain Molecules* (Akad. Nauk SSSR, Moscow, 1963).
4. M. Miler, *Holography* (Mashinostroenie, Leningrad, 1979), translated from Czech.
5. A. F. Skryshevskiĭ, *Structural Analysis of Fluids and Amorphous Bodies*, 2nd ed. (Vysshaya Shkola, Moscow, 1980).
6. A. F. Skryshevskiĭ, *Structural Analysis of Fluids: X-ray Diffraction Analysis, Neutron Diffraction Analysis* (Vysshaya Shkola, Moscow, 1971).
7. *Physical Methods of Studying Proteins and Nucleic Acids: Collection of Articles*, Ed. by Yu. S. Lazutkin (Nauka, Moscow, 1967).
8. V. N. Izmaĭlova, G. P. Yampol'skaya, and B. D. Summ, *Surface Phenomena in Protein Systems* (Khimiya, Moscow, 1988).
9. T. H. James and C. E. Mees, *Theory of the Photographic Process* (Macmillan, New York, 1966; Khimiya, Leningrad, 1973).
10. L. I. Mirkin, *Handbook of X-ray Analysis of Polycrystalline Materials* (Fizmatgiz, Moscow, 1961; Plenum Press, New York, 1964).
11. Yu. P. Gomza, Yu. E. Kuzilin, Yu. B. Mel'nichenko, and V. V. Shilov, Usp. Nauchn. Fotogr. **26**, 124 (1992).

Translated by P. Pozdeev

Technical Physics Letters, Vol. 30, No. 1, 2004, pp. 51–54. Translated from Pis'ma v Zhurnal Tekhnicheskoĭ Fiziki, Vol. 30, No. 2, 2004, pp. 25–32.

The Synthesis and Properties of Epitaxial Layers of $(Si_2)_{1-x}(GaAs)_x$ Solid Solutions on Silicon Substrates

B. Sapaev, A. S. Saidov, and B. N. Zaveryukhin

Physicotechnical Institute, "Solar Physics" Research and Production Corporation, Academy of Sciences of the Republic of Uzbekistan, Tashkent, Uzbekistan

e-mail: atvi@physic.uzsci.net

Received June 2, 2003

Abstract—Epitaxial layers of $(Si_2)_{1-x}(GaAs)_x$ ($0 \le x \le 0.85$) solid solutions were grown by liquid phase epitaxy in a temperature interval from 850 to 700°C from a tin-based solution melt confined between two horizontal polycrystalline silicon substrates. The dependence of the quality and parameters of the epilayers on the process conditions have been studied. The obtained $Si–(Si_2)_{1-x}(GaAs)_x$ structures can be used in various microelectronic and photoconversion devices, replacing analogous but more expensive GaAs-based structures. Experimental data on the electrical properties and photoelectric characteristics of the $Si–(Si_2)_{1-x}(GaAs)_x$ structures are presented. © *2004 MAIK "Nauka/Interperiodica".*

Heterostructures based on the $A^{III}B^{V}$ and $A^{IV}B^{IV}$ semiconductor compounds offer unique combinations of properties and receive increasing attention of researchers. Silicon, belonging to group IV of the Periodic Table, possesses certain advantages over the other semiconductor materials, including higher mechanical strength, better thermal conductivity, lower cost, and some others. On the other hand, silicon is inferior to $A^{III}B^{V}$ semiconductor compounds in some other respects, for example, in radiation stability and the efficiency of solar energy conversion into electricity. For this reason, good prospects are related with the growth of thin (≤20 μm) GaAs epilayers on cheaper substrates, in particular, on polycrystalline silicon (polysilicon). In this context, investigations of the growth process aimed at the synthesis of new solid solutions of the $(Si_2)_{1-x}(GaAs)_x$ system possessing unique properties is a highly promising direction in semiconductor physics and technology.

Metastable continuous solid solutions of the $(C_2^4)_{1-x}(A^3B^5)_x$ type were originally obtained by pyrolytic synthesis [1]. The electrical properties of these solid solutions were reported in [2]. The present study was aimed at obtaining epilayers of $(Si_2)_{1-x}(GaAs)_x$ solid solution on polysilicon substrates by liquid phase epitaxy (LPE) from a limited volume of a Sn–Si–GaAs solution melt. We have also studied the electrical properties and photoelectric characteristics of the obtained $Si–(Si_2)_{1-x}(GaAs)_x$ structures.

For determining the optimum solution melt composition, we have preliminarily studied the phase diagrams of the Si–GaAs–solvent system using the solubility technique [3] and the published data [4]. The epitaxial growth technology involved conventional stages [5]. The layers of $(Si_2)_{1-x}(GaAs)_x$ solid solutions were grown from a limited volume of a tin-based solution melt in a temperature interval from 850 to 700°C in an atmosphere of palladium-purified hydrogen. The melt was confined between two substrates having the shape of disks with a diameter of 20 mm and a thickness of 350–400 μm. The disks were cut from coarse- and fine-grained polysilicon plates of the *n*- and *p*-type conductivity with a resistivity of $\rho \approx 30\ \Omega$ cm and 0.1–3.0 Ω cm, respectively.

In order to determine how the properties of epilayers of the $(Si_2)_{1-x}(GaAs)_x$ solid solutions depend on the growth conditions, we have varied the crystallization onset temperature T_1 and the spacing δ between parallel substrates oriented in the horizontal plane. In some cases, about 0.1 at. % of aluminum was added to the solution melt in order to improve the substrate wetting and obtain samples with mirror-smooth surfaces [6]. The resulting epitaxial films grown on *p*-type substrates formed a *p–n* junction, while the films grown on the *n*-type substrates contain an isotype *n–n* junction.

When the crystallization begins at $T_1 < 700$°C, the growing layer appears as a polyhedral dendrite cone (sometimes, a polyhedron) tightly bound to the substrate. On the substrate, the dendrites were sometimes separated by thin (0.1–0.3 μm thick) films. The structure of layers grown beginning with $T_1 > 800$°C was also dendritic, but the dendrites were arranged in the layers of 5- to 10-μm-thick films. The dendrite size increases with the crystallization onset temperature T_1 until reaching the upper substrate (to which the dendrites are also bound). The films grown under optimum conditions, including proper crystallization onset (T_1) and growth termination (T_2) temperatures and the sub-

strate spacing δ, possessed smooth mirror-bright surfaces with ornaments reproducing the patterns of grains on the polysilicon substrates.

The results of investigations of the film thickness and structure as dependent on the crystallization onset temperature and the cooling rate showed that the growth of films beginning with $T_1 < 700$°C at a cooling rate above 1.5 K/min is accompanied by increasing dendrite size. A decrease in the cooling rate below 0.5–0.75 K/min significantly increases the process duration and, hence, the energy consumption, while not providing any significant increase in parameters of the grown layers.

For the crystallization onset temperatures $T_1 >$ 800°C, cooling at a rate exceeding 1.0–1.2 K/min was unacceptable because bulk crystallization took place in the volume of the solution melt. This leads to the appearance of dendrites weakly (or not at all) connected with the layer (sometimes, such dendrites can be detached from the film without breaking the surface). The films grown beginning with $T_1 = 800$°C at a cooling rate below 0.5–0.75 K/min contain almost no dendrites, but this is achieved at the expense of high energy consumption. Finally, films grown in the interval of the crystallization onset temperatures from 700 to 800°C at a cooling rate of 0.75–1.0 K/min are smooth and mirror bright.

The compositions and thicknesses of the obtained epitaxial films were determined by the method of thin-film X-ray radiometry [7]. The characteristic emission from the component elements was excited by X-ray radiation from a ^{109}Cd source (for Ga and As) and by γ radiation from an ^{241}Am source (for Sn) and detected by a system including a Si(Li) detector (energy resolution $R = 300$ eV) and a spectrometric complex based on an AI-1024-95-02 amplitude analyzer. The quantitative content of each element in epilayers of the $(Si_2)_{1-x}(GaAs)_x$ solid solutions was determined by comparing the characteristic emission intensities measured using the samples with known and unknown compositions. For this X-ray radiometric analysis, we used several standard plates of polycrystalline silicon with epilayers of various compositions.

The content of each chemical element—for example, arsenic—was calculated using the formula [7]

$$C_{As} = \frac{I_{As} C_{As}(\text{st.})}{I_{As}(\text{st.})}, \quad (1)$$

where C_{As} and C_{As}(st.) are the concentrations of arsenic in the sample and standard, respectively, and I_{As} and I_{As}(st.) are the intensities of characteristic emission lines for the sample and standard, respectively. Percentage compositions of the epilayers were determined using data on the initial content of each element (in grams) and then used for estimating the film density and thickness. The error of such determinations did not exceed 5%.

We have also used an X-ray microprobe of the Jeol JSM 5910LV type (Japan) for an analysis of the surface composition and for scanning cleavages of the epilayers of $(Si_2)_{1-x}(GaAs)_x$ solid solutions. The results of these measurements are presented in Fig. 1a. An analysis of the scanning electron micrographs of the surface of samples showed that the epilayers of $(Si_2)_{1-x}(GaAs)_x$ solid solutions contain no macroscopic defects and metallic inclusions and confirmed homogeneous distribution of all elements both in plane and in depth of the solid solution layer.

The structural perfection of the epitaxial layers was checked by X-ray diffraction. The measurements were performed using specially prepared epitaxial layers of $(Si_2)_{1-x}(GaAs)_x$ solid solutions with a thickness of d = 3–5 μm. The diffraction patterns were obtained on a DRON-3M diffractometer using filtered Cu$K_{\alpha 1}$ (λ = 1.5405 Å) and Cu$K_{\alpha 2}$ (λ = 1.5443 Å) radiations from an X-ray tube with the copper anode operating at 30 kV and 20 mA. Separate recording of reflections from the same plane for both components increases the accuracy of determination of the interplanar spacings d_{hkl} (h, k, l are the Miller indexes). The K_α emission line represents a doublet (α_1 and α_2), provided that the spectrograph possesses a sufficiently high resolving power. Splitting of the spectral line into a doublet is clearly demonstrated in Fig. 1b. This doublet is due to the fact that the electron energy in an atom depends not only on the principal quantum number but on the azimuthal and spin quantum numbers as well.

The lattice parameter a was determined by measuring selected reflections in the course of point-by-point measurement at an angular step of $\Delta(2\theta) = 0.01°$ and data acquisition time of $\tau = 20$ s at each point. The Bragg diffraction condition can be written as $\lambda = 2d_{hkl}\sin\theta$, where d_{hkl} [Å] is the spacing between atomic planes with the Miller indexes hkl; λ [Å] is the radiation wavelength; and θ [deg] is the Bragg angle of X-ray diffraction. This yields the following formula for the lattice parameter: $a = d\sqrt{h^2 + k^2 + l^2}$ [8]. The uncertainty of determination of the interplanar spacing d_{hkl} in the region of $2\theta = 53$–58° for the (311) reflection amounts to $\Delta d \approx 0.0001$ Å, and the error of determining the parameter a is $\Delta a \approx 0.0004$ Å. The absence of other peaks in the diffractogram and the presence of a $K_{\alpha 1}$ and $K_{\alpha 2}$ doublet is additional evidence of a high structural perfection of the obtained epilayers. The shapes and positions of peaks on the diffractograms depend on the growth conditions.

We have also studied some electrical properties of the obtained epilayers of $(Si_2)_{1-x}(GaAs)_x$ solid solutions. The Hall effect measurements showed that the electron and hole mobilities are $\mu_n \approx$ 800–1200 cm^2/(V s) and

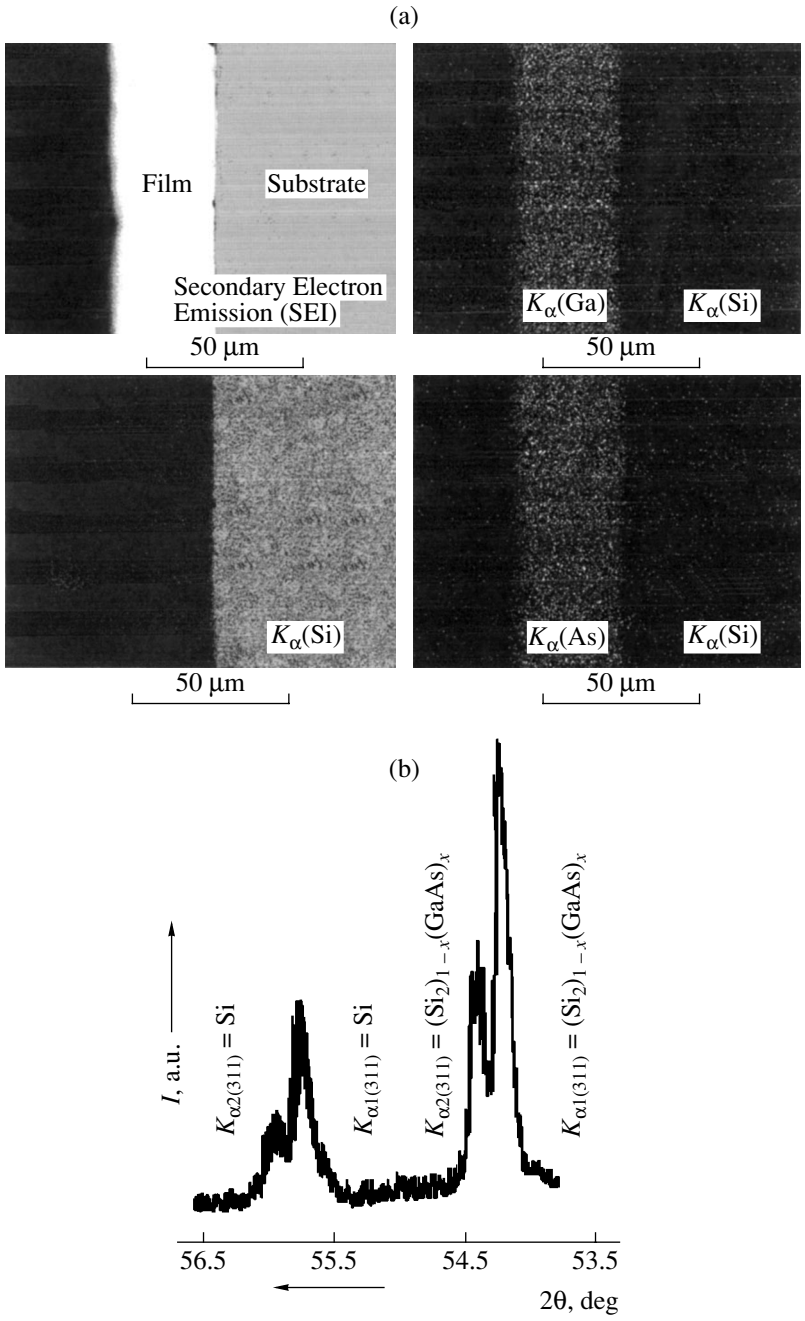

Fig. 1. Si–$(Si_2)_{1-x}(GaAs)_x$ structures: (a) scanning electron micrographs; (b) X-ray diffractograms.

$\mu_p \approx 500$–800 cm^2/(V s), respectively. The four-point-probe measurements of the resistivity showed that the self-doped $(Si_2)_{1-x}(GaAs)_x$ epilayers exhibit conductivity of the *n* type with $\rho \approx 0.5$–1.5 Ω cm. We have measured the spectral sensitivity and the current–voltage characteristics of device structures of the *p*-Si/*n*-$(Si_2)_{1-x}(GaAs)_x$ type based on the obtained epilayers. The *p*–*n* junctions of these structures exhibit rectifying properties in a broad temperature range (77–100 K), but the mechanism of charge transfer in this system is rather complicated.

The obtained Si–$(Si_2)_{1-x}(GaAs)_x$ structures exhibit photosensitivity in a wavelength range of $\lambda \approx 0.427$–1.1 μm (Fig. 2). The initial photoresponse at $E \approx 1.1$–1.4 eV is related to the generation of nonequilibrium charge carriers in the silicon substrate and the $(Si_2)_{1-x}(GaAs)_x$ epilayer. In the interval of photon energies $E \approx 1.42$–1.6 eV, the increase in the photocurrent is due to the production of nonequilibrium charge carriers in the *p*–*n* junction and in the adjacent GaAs layer. In the energy range $E = 1.6$–2.8 eV, one portion of charge carriers generated in the GaAs layer reaches the *p*–*n*

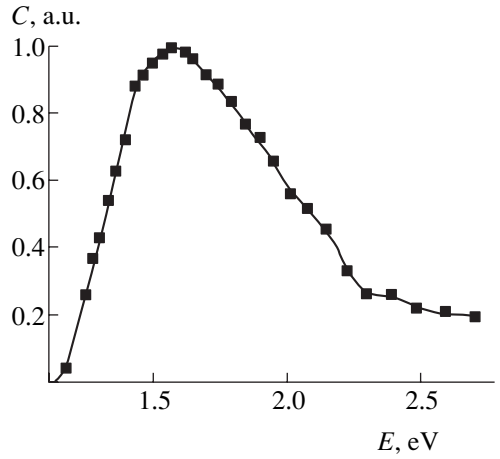

Fig. 2. The typical spectral characteristic of a Si–$(Si_2)_{1-x}(GaAs)_x$ heterostructure.

junction and contributes to the photocurrent, while the other carriers are trapped on deep levels in the GaAs layer. This leads to a decrease in the signal amplitude in the wavelength interval $\lambda \approx 0.427$–0.77 μm.

This study was not aimed at determining the nature and parameters of deep levels present in the Si–$(Si_2)_{1-x}(GaAs)_x$ structures under consideration. The open-circuit voltage of these structures is $V_{oc} \approx$ 0.80–0.83 V, and the short-circuit current density is $I_{sc} \approx$ 10–12 mA/cm^2 (without clarification). These values agree with the published data for GaAs-based structures with *p–n* homojunctions and comparable with the data for analogous structures grown on single crystal GaAs substrates.

To summarize, methods developed in this study allow the synthesis of epilayers of new $(Si_2)_{1-x}(GaAs)_x$ solid solutions meeting high requirements of semiconductor device technology and providing for the obtainment of high-quality devices. The epilayers of $(Si_2)_{1-x}(GaAs)_x$ solid solutions grown on silicon substrates can be successfully used instead of analogous structures based on expensive single crystal GaAs substrates.

REFERENCES

1. Zh. I. Alferov, M. Z. Zhingarev, S. G. Konnikov, *et al.*, Fiz. Tekh. Poluprovodn. (Leningrad) **16**, 831 (1982) [Sov. Phys. Semicond. **16**, 532 (1982)].
2. Zh. I. Alferov, R. S. Vartanyan, V. I. Korol'kov, *et al.*, Fiz. Tekh. Poluprovodn. (Leningrad) **16**, 887 (1982) [Sov. Phys. Semicond. **16**, 567 (1982)].
3. A. S. Saidov, M. S. Saidov, and É. A. Koshchanov, *Liquid Epitaxy of Compensate Layers of Gallium Arsenide and Solid Solutions on Their Basis* (Fan, Tashkent, 1986), p. 129.
4. V. M. Andreev, L. M. Dolginov, and D. N. Tret'yakov, *Liquid Epitaxy in Technology of Semiconductor Devices* (Sov. Radio, Moscow, 1975), p. 328.
5. M. Hansen and K. Anderko, *Constitution of Binary Alloys* (McGraw-Hill, New York, 1958; Metallurgizdat, Moscow, 1962).
6. B. Sapaev, A. S. Saidov, and U. T. Davlatov, Vestn. Gulistansk. Gos. Univ., No. 1, 50 (2001).
7. S. V. Mamikanyan, *Equipment and Methods of Fluorescence X-ray Radiometric Analysis* (Atomizdat, Moscow, 1976), p. 279.
8. E. F. Vegman, Yu. G. Rufanov, and I. N. Fedorchenko, *Crystallography, Petrography and X-ray Radiography* (Metallurgiya, Moscow, 1990), p. 264.

Translated by P. Pozdeev

Technical Physics Letters, Vol. 30, No. 1, 2004, pp. 55–57. Translated from Pis'ma v Zhurnal Tekhnicheskoĭ Fiziki, Vol. 30, No. 2, 2004, pp. 33–37.

The Lagrange Formalism with Fractional Derivatives in Problems of Mechanics

S. Sh. Rekhviashvili

Kabardino-Balkarian State University, Nalchik, Kabardino-Balkaria, Russia

e-mail: rsergo@mail.ru

Received May 14, 2003; in final form, July 8, 2003

Abstract—An analog of the Lagrange equation with a fractional derivative with respect to time is derived using the principle of least action. Based on this approach, a new equation of motion is obtained and the solution of a simple kinematical problem is found that shows the "mechanical sense" of the fractional derivative. The proposed approach allows a new formulation of various problems in mechanics and mathematical physics.

The concept of fractional derivatives arises in many fields of physics, especially in the problems related to transfer processes in fractal media (see, e.g., [1–5] and references therein). Typical examples of such media are carbon nanocomposites, structured polymers, and various porous materials. Recently, Guk [5] considered the Lagrange formalism in application to an equation with fractional derivatives describing the motion of a particle in a fractal medium. However, the result should be treated as incorrect because the obtained equation (see [5, Eq. (5)]) does not minimize the action functional and, hence, is inconsistent with the initial formulation of the problem.

Let us consider the motion of a particle in a fractal medium. By analogy with [3], we define the average velocity of the particle in this medium as

$$\langle v(t)\rangle = \frac{1}{\tau}D_{0t}^{\alpha-1}v(t) = \frac{1}{\tau}D_{0t}^{\alpha-1}\frac{dx(t)}{dt} = \frac{1}{\tau}D_{0t}^{(\alpha)}x(t), \quad 0 \le \alpha \le 1, \tag{1}$$

where τ is the characteristic time of the process, t is the dimensionless (normalized to τ) time, $v(t)$ is the current velocity of the particle in the fractal, and $x(t)$ is the particle coordinate. In this definition, D_{st}^{α} is the Riemann–Liouville integro-differential operator of the fractional order α defined as [4, 6]

$$D_{st}^{\alpha}g(t) = \begin{cases} \dfrac{\operatorname{sgn}(t-s)}{\Gamma(-\alpha)}\displaystyle\int_s^t \frac{g(t')dt'}{(t-t')^{\alpha+1}}, & \alpha < 0, \\ \operatorname{sgn}^{[\alpha]+1}(t-s)\dfrac{d^{[\alpha]+1}}{dt^{[\alpha]+1}}D_{st}^{\alpha-[\alpha]-1}g(t), & \alpha \ge 0, \end{cases}$$

where $\Gamma(-\alpha)$ is the Euler gamma function, $[\alpha]$ is the integer part of α, and $D_{st}^{(\alpha)}$ is the regularized fractional derivative of the fractional order α,

$$D_{st}^{(\alpha)}g(t) = D_{st}^{\alpha-1}\frac{dg(t)}{dt}.$$

Taking into account definition (1), the generalized action functional is written as

$$S = \int_0^T L(t, x(t), \langle v(t)\rangle)dt, \tag{2}$$

where T is the total time of the particle motion (normalized to τ). The integration limits from 0 to T in Eq. (2) are selected so as to simplify writing (as can be readily checked, the integration limits do not influence subsequent considerations). Let $x_0(t)$ be a solution of the problem (2) (i.e., the functional exhibits an extremum). For the comparative curves

$$x(t) = x_0(t) + \varepsilon h(t),$$

$$h(0) = h(T) = 0$$

(where ε is a small parameter), Eq. (2) yields

$$S = \int_0^T L\left(t, x_0(t) + \varepsilon h(t), \frac{1}{\tau}D_{0t}^{(\alpha)}x(t) + \frac{\varepsilon}{\tau}D_{0t}^{(\alpha)}h(t)\right)dt. \tag{3}$$

The action functional S depends on a single parameter ε. Since $x_0(t)$ is a solution, we have $\delta S = 0$, where δ denotes incomplete isochronous variation. Relation (3) corresponds to the well-known principle of least action.

Using this expression, the first variation of the functional is calculated as

$$\frac{dS}{d\varepsilon} = \int_0^T \left(\frac{dL}{d\varepsilon}\right) dt = \int_0^T \left(\frac{dL}{dx} - \frac{1}{\tau} D_{Tt}^{(\alpha)} \frac{dL}{d\langle v \rangle}\right) h(t)\, dt, \quad (4)$$

where $\langle v \rangle$ is defined in (1) and $D_{Tt}^{(\alpha)}$ is the regularized fractional derivative of the fractional order α calculated on the interval from T to t. Equating derivative (4) to zero, we obtain

$$\frac{dL}{dx} - \frac{1}{\tau} D_{Tt}^{(\alpha)} \frac{dL}{d\langle v \rangle} = 0. \quad (5)$$

As can be readily seen, the usual Lagrange equation is a partial case of Eq. (5) and exactly follows from this equation for $\alpha = 1$.

Now, let us consider the equation of motion. For this purpose, it is necessary to define the function L. According to the initial problem formulation, this function must depend on $\langle v \rangle$. Since the Euclidean space in which the fractal is embedded is homogeneous and isotropic, the function L has to be scalar and explicitly independent of time. Therefore, L can be expanded into series in even powers of $\langle v \rangle$. To within the second-order terms, we have

$$L = -U(x) + \frac{m}{2} \langle v \rangle^2. \quad (6)$$

The coefficient m and $U(x)$ do not depend on the order of the fractional derivative determining the velocity $\langle v \rangle$. Therefore, there is no reason for distinguishing these quantities from the usual mass and potential energy of the particle. Substituting expression (6) into relation (5), we obtain the following equation for the unknown function $x(t)$:

$$\frac{m}{\tau^2} D_{Tt}^{(\alpha)} D_{0t}^{(\alpha)} x(t) = -\frac{dU(x)}{dx}. \quad (7)$$

As expected, Eq. (7) with $\alpha = 1$ becomes the classical equation of motion. The right-hand part of Eq. (7) determines a conservative force acting upon the particle.

It should be pointed out that it is common practice to write an equation of motion by formally replacing the ordinary derivative by a fractional, instead of deriving Eq. (7). However, from the standpoint of physics, such a replacement is absolutely unjustified: first, the modified equation does not obey the principle of least action, and second, it does not lead to the principle of relativity. Unfortunately, these facts are ignored.

In order to determine the physical meaning of the left-hand part of Eq. (7), let us consider the simplest example corresponding to free motion. In this case, Eq. (7) appears as

$$D_{Tt}^{(\alpha)} D_{0t}^{(\alpha)} x(t) = 0. \quad (8)$$

Writing this equation in terms of the fractional Riemann–Liouville derivatives, we obtain

$$D_{Tt}^{\alpha-1} \frac{d}{dt} \left\{ D_{0t}^{\alpha-1} \frac{dx(t)}{dt} \right\} = 0. \quad (9)$$

Applying operator $D_{Tt}^{1-\alpha}$ to Eq. (9) and integrating with respect to t, we obtain

$$D_{0t}^{\alpha-1} \frac{dx(t)}{dt} = \text{const}. \quad (10)$$

Then, applying operator $D_{0t}^{1-\alpha}$ to Eq. (10), integrating with respect to t, and taking into account the boundary conditions, we arrive to the final solution

$$x(t) = x(0) + \frac{x(T) - x(0)}{T^\alpha} t^\alpha. \quad (11)$$

As can be seen from this expression, changing α from 1 to 0 in the absence of conservative forces corresponds to the passage from uniform motion to full stop. Indeed, for $\alpha = 1$, the uniform motion trajectory is $x(t) = x(0) + v_0 t$, where $v_0 = (x(T) - x(0))/T$; for $\alpha = 0$, the motion terminates at the point $x(T)$. This implies that the motion accompanied by variation of the parameter α occurs in a kind of "dissipative" medium. The same conclusion follows from the consideration of other simple motions.

It can be noted that Eq. (7) with $\alpha < 1$ is not symmetric with respect to the sign of time, which is also indicative of a "dissipative" (irreversible) character of this motion. Sometimes, such processes are also referred to as the "motions with loss of memory." As for the power term t^α in Eq. (11), such a term is typical of many dynamic fractals and frequently appears in the physical characteristics of kinetic processes in fractal media. In particular, Eq. (11) coincides in form with the well-known Hurst law obtained from experimental measurements of the income and outcome of lake water [7].

Thus, the application of a fractional derivative of the trajectory with respect time in the principle of least action allows dissipation processes in a mechanical system to be explicitly taken into account. It would be of interest from the standpoint of both physics and mathematics to apply Eq. (7) to various problems in mechanics and mathematical physics.

Acknowledgments. The author is grateful to A.V. Pskha for fruitful discussions.

REFERENCES

1. A. N. Kochubeĭ, Differ. Uravn. **26**, 1359 (1990).
2. A. I. Saichev and S. G. Utkin, Zh. Tekh. Fiz. **73** (7), 1 (2003) [Tech. Phys. **48**, 801 (2003)].
3. V. Kh. Shogenov, S. K. Kumykova, and M. Kh. Shkhanukov-Lafishev, Dokl. Nats. Akad. Nauk Ukr., No. 12, 47 (1997).
4. A. M. Nakhushev, *Elements of Fraction Calculus and Their Application* (Kabardino-Balkarsk. Nauchn. Tsentr Ross. Akad. Nauk, Nalchik, 2000).
5. I. P. Guk, Zh. Tekh. Fiz. **68** (4), 7 (1998) [Tech. Phys. **43**, 353 (1998)].
6. S. G. Samko, A. A. Kilbas, and O. I. Marichev, *Fractional Integrals and Derivatives. Theory and Applications* (Nauka i Tekhnika, Minsk, 1987; Gordon and Breach, Amsterdam, 1993).
7. J. Feder, *Fractals* (Plenum, New York, 1988; Mir, Moscow, 1991).

Translated by P. Pozdeev

Technical Physics Letters, Vol. 30, No. 1, 2004, pp. 58–59. Translated from Pis'ma v Zhurnal Tekhnicheskoĭ Fiziki, Vol. 30, No. 2, 2004, pp. 38–42.

Deformation-Induced Electric Noise in Steel under Plasto-Elastic Alternating Strain Conditions

V. M. Baranov, E. Yu. Kapralov*, and Yu. A. Kapralov

Moscow Physical Engineering Institute (State Technical University), Moscow, Russia

**e-mail: e-kapr@kpu.mephi.ru*

Received June 27, 2003

Abstract—We have studied the relationship between mechanical stresses developed in steel under the conditions of cyclic plasto-elastic loading to a preset strain level and a noise component of the ac electric current induced by the alternating voltage applied to the sample. Both the mechanical and the electric noise characteristics are different in the steel samples not subjected to mechanical surface processing and in those with polished surfaces. It is shown that the stage of accumulation of the structural changes leading to fatigue fracture of a material can be determined by measuring the electric noise parameters of the samples.

The development of methods for diagnostics and prediction of the working life of materials and structures subjected to fatigue straining is still an important task. Recently [1–3], we demonstrated that such diagnostics can employ the noise techniques based on the monitoring and analysis of a random noise component of the electric current passing through a given structural material (e.g., steel). In continuation of these investigations, we have attempted to detect changes in the spectral density of electric noise in the range of low and infralow frequencies depending on the preliminary mechanical processing of steel samples.

The method of fatigue strain testing was generally analogous to that described previously [3]. The sample of a structural steel (steel 20) in the form of an ~0.5-mm-thick plate was fastened with one end in a dielectric holder with a diameter of d = 2 mm and strained by bending to a preset angle ($\varphi = \pm 45°$) relative to the initial position. The sample was connected to an ac voltage generator, so that both the constant component and fluctuations of the current in this circuit could be monitored together with the characteristics of loading (maximum load required for bending the sample to a preset angle in each half-cycle of straining).

In the given series of fatigue tests, we have studied three samples randomly selected from a batch of like plates. Samples 1 and 2 were preliminarily not processed, while the surface of sample 3 in the zone of plastic deformation was ground and finished to R_z = 0.8–0.4 μm, which resulted in preliminary strengthening of the material [4].

The results of tests for samples 1 and 2 are presented in Fig. 1a, where solid curves show variation of the maximum deforming moment M_{def} (calculated as a product of the maximum load by length of the sample) versus the relative number of loading cycles to fracture $N_a = N/N_{\text{f}}$ (where N_{f} is the number of the cycle during which the sample exhibited fracture). As can be seen from these data, the samples (both 1 and 2) not subjected to preliminary mechanical processing initially exhibit strengthening (at N_a = 0.1–0.3). Then, the maximum load decreases to the initial level and remains approximately constant in the interval N_a = 0.4–0.6. Finally, the maximum load exhibits a monotonic decrease until the moment of fracture.

Dashed curves in Fig. 1a show the behavior of the spectral density S of the electric noise averaged over the frequency range of 0.001–0.05 Hz, also plotted versus the relative number of cycles N_a for samples 1 and 2. The experimental spectral density curves were smoothened using a polynomial approximation with fitting by least squares. As can be seen, this noise characteristic exhibits local minima and maxima in the region N_a = 0.1–0.8 for sample 1 and N_a = 0.1–0.65 for sample 2, with the difference between the maximum and minimum S values reaching 0.5×10^{-7} V^2/Hz. The different shapes of the S curves of samples 1 and 2 in the initial stage of experiment is apparently due to the difference in the initial condition of these samples (not subjected to preliminary mechanical treatments). This assumption is consistent with the fact that the M_{def} curve of sample 2 is also shifted by $N_a \sim 0.1$ relative to the curve of sample 1. In the interval N_a = 0.8–1.0, the spectral density of the infralow-frequency noise monotonically increases. Note that the minimum in the noise characteristic S corresponds to the onset of a transition to the state of decreased resistance to the bending strain. According to the results of microscopic observations (MBS-2 microscope), this related to the formation of macroscopic cracks in the material.

Thus, there are three stages in the fatigue straining of samples 1 and 2. The initial strengthening, accompa-

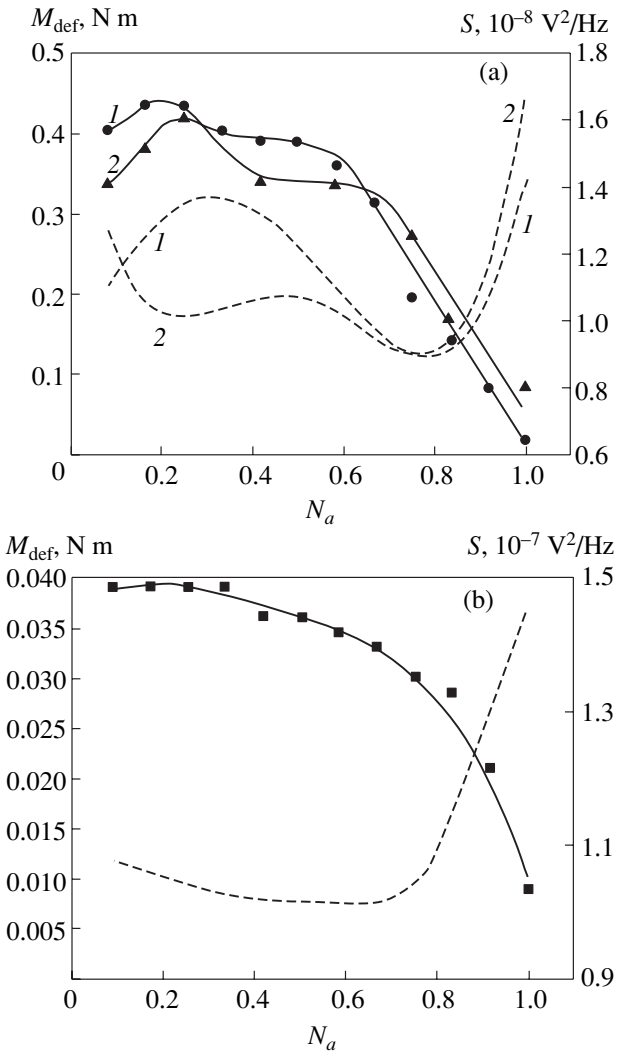

Fig. 1. Plots of the maximum deforming moment M_{def} (solid curves) and the spectral density S of electric noise in the 0.001–0.05 Hz frequency range (dashed curves) versus relative number of bending cycles N_a to fracture for steel samples (a) not subjected to mechanical surface processing and (b) in those with ground and finished surfaces.

nied by a local maximum in the noise characteristic, probably corresponds to an increase in the density of dislocations in the zone of plastic deformation. The resulting increase in electric resistance of the working part of the sample leads, according to the Nyquist theorem [5], to an increase in the noise component.

Upon reaching the maximum possible density of dislocations in the deformation zone, this parameter is saturated and the subsequent increase in the plastic straining takes place at a constant load. This is accompanied by clusterization of the point defects present in the zone of plastic deformation [6], which probably leads to a decrease in the spectral density of noise.

A minimum in the spectral density of noise is attained immediately before the main crack formation, while the subsequent growth of S can be related to the formation of new surfaces that results in a growth of the electric resistance of the working part of the sample.

As can be seen from Fig. 1b, sample 3 does not exhibit the stage of initial strengthening. In this case, the deforming moment (solid curve) remains approximately constant in the interval N_a = 0.1–0.35 and then monotonically decreases until the moment of sample fracture. Note that this decrease proceeds differently before and after the main crack formation taking place at N_a = 0.7–0.8. In the absence of initial strengthening, the spectral density of electric noise decreases (similarly to the previous case) at an almost constant straining load, which is probably indicative of a constant configuration of structural defects. During the subsequent decrease in the deforming moment, the noise level remains constant in the subcritical cracking stage and increases in the supercritical crack growth stage.

Thus, by measuring the spectral density of electric noise, it is possible to estimate the state of a material from the standpoint of fatigue accumulation in the course of plasto-elastic straining and to detect the moment of macroscopic crack formation. In addition, this method distinguishes the materials subjected or not to mechanical surface processing.

Acknowledgments. This study was supported by the Ministry of Education of the Russian Federation, project no. 01.2003.04409.

REFERENCES

1. V. M. Baranov, T. V. Gubina, and E. Yu. Kapralov, in *Proceedings of the 14th Scientific–Technological Conference, Moscow, 2002* (Mos. Gos. Inst. Elektron. Mashinostr., Moscow, 2002), pp. 205–206.
2. V. M. Baranov and E. Yu. Kapralov, Tr. Mosk. Inzh.-Fiz. Inst. **9**, 165 (2003).
3. V. M. Baranov, E. Yu. Kapralov, and Yu. A. Kapralov, Zavod. Lab. **69** (3), 36 (2003).
4. V. E. Panin, V. S. Pleshanov, S. A. Burkova, *et al.*, Materialovedenie, Nos. 8–9, 22 (1997).
5. J. S. Bendat and A. G. Piersol, *Random Data: Analysis and Measurement Procedures* (Wiley, New York, 1971; Mir, Moscow, 1974).
6. A. A. Berzin, A. I. Morozov, and A. S. Sigov, Fiz. Tverd. Tela (St. Petersburg) **42**, 1757 (2000) [Phys. Solid State **42**, 1802 (2000)].

Translated by P. Pozdeev

Technical Physics Letters, Vol. 30, No. 1, 2004, pp. 6–8. Translated from Pis'ma v Zhurnal Tekhnicheskoĭ Fiziki, Vol. 30, No. 1, 2004, pp. 15–20.

Giant Magnetoelectric Effect in Composite Materials in the Region of Electromechanical Resonance

D. A. Filippov[a,*], M. I. Bichurin[a], V. M. Petrov[a], V. M. Laletin[b], N. N. Poddubnaya[b], and G. Srinivasan[c]

[a] *Novgorod State University, Velikiĭ Novgorod, Russia*
[b] *Institute of Technical Acoustics, Vitebsk, Belarus*
[c] *Physics Department, Oakland University, Rochester, Michigan 48309, USA*
* *e-mail: fdma@novsu.ac.ru*

Received June 30, 2003

Abstract—The magnetoelectric effect in multilayer ferrite-piezoelectric composites has been theoretically and experimentally studied. Using the method of effective parameters, an expression for the magnetoelectric coefficient is determined and its frequency dependence is analyzed. It is shown that, in the region of electromechanical resonance, the magnitude of the effect exceeds a low-frequency value by more than an order of magnitude. The results of calculations obtained for a nickel ferrite spinel–PZT composite are in good agreement with the experimental data. © *2004 MAIK "Nauka/Interperiodica".*

Magnetoelectric composite materials are mechanical mixtures of magnetic and piezoelectric components prepared using standard ceramic technology. In these materials, it is possible to observe effects that are absent in each of the individual components. In particular, these materials exhibit a magnetoelectric (ME) effect consisting in the appearance of a polarization under the action of a magnetic field and, vice versa, in the appearance of a magnetization under the action of an electric field.

The ME effect in composite materials is related to the interaction between the ferrite and piezoelectric subsystems. In a magnetic field, magnetostriction in the ferrite component gives rise to mechanical stresses that are transferred into the piezoelectric phase and, owing to the piezoelectric effect, cause a polarization. Since the appearance of polarization in such composite materials under the action of a magnetic field is associated with the appearance of mechanical stresses, it is reasonable to expect that the magnitude of this effect will be much greater in the region of the electromechanical resonance [1, 2]. The ME effect in bulk composite materials in the region of the electromechanical resonance was first reported in [3]. However, the electromechanical resonance in that study was only used as a method for detecting the useful signal on a noise background and no detailed investigation of the ME effect was performed.

In this paper, we report the results of theoretical and experimental investigation of the ME effect in the region of the electromechanical resonance in multilayer composite materials. Macroscopically, the composite materials can be characterized by certain effective parameters, such as the effective elastic moduli (compliances), effective piezoelectric coefficients, and effective magnetostriction constants. It is evident that these effective parameters are determined by the properties of the ferrite and piezoelectric components, the degree of connectivity, and the concentrations of these components in a given composite material [4]. These effective parameters can be used if the characteristic scale of the external action is much greater than the size of the base structural unit. In layered materials, such a parameter is the layer thickness of the ferrite and piezoelectric components. Since the typical layer thickness in a layered composite material is on the order of 10 μm, the above effective parameters can be used to describe the propagation of elastic interactions at frequencies up to about several hundred megahertz.

As a model, we consider a ferrite-piezoelectric composite material in the form of a thin plate with thickness d, width b, and length L. The top and bottom surfaces of the plate bear thin metal contacts. Let the sample be polarized along the normal to the contact planes (the Z axis). Magnetic fields (a static bias magnetic field and an alternating field with a frequency of ω) can be directed either along the same axis (longitudinal field orientation) or perpendicularly to the polarization direction, i.e., along the X axis (transverse field orientation). Accordingly, we will distinguish the longitudinal and transverse ME effects. Due to magnetostriction, the alternating magnetic field induces oscillations that propagate both in depth and in plane of the plate. In what follows, we consider oscillations of the lowest frequency, i.e., the volume oscillations propagating along the plate. It is assumed that the plate thickness and width are much smaller than its length, i.e., $d \ll L$ and $b < L$. The faces of the plate are assumed to be free;

1063-7850/04/3001-0006$26.00 © 2004 MAIK "Nauka/Interperiodica"

therefore, the surface stresses are equal to zero. Since the plate is thin and narrow, stress components T_2 and T_3 are assumed to be zero not only on the surfaces but throughout the volume. Thus, the only nonzero component is T_1. In addition, since the top and bottom faces of the plate are equipotential surfaces, the only nonzero component of the electric field intensity vector is E_z.

For the longitudinal field orientation, equations for the strain tensor S_i and the electric induction D_i have the form

$$S_1 = s_{11}T_1 + d_{31}E_3 + q_{31}H_3, \quad (1)$$

$$D_3 = \varepsilon_{33}E_3 + d_{31}T_1 + \alpha_{33}H_3, \quad (2)$$

where s_{11} are the components of the compliance tensor; ε_{33} and α_{33} are the components of the permittivity tensor and the magnetoelectric susceptibility tensor, respectively; and d_{31} and q_{33} are the piezoelectric and piezomagnetic coefficients, respectively.

For a transverse field orientation, the equations can be written as

$$S_1 = s_{11}T_1 + d_{31}E_3 + q_{11}H_1, \quad (3)$$

$$D_3 = \varepsilon_{33}E_3 + d_{31}T_1 + \alpha_{31}H_1. \quad (4)$$

Expressing the stress components via the deformation components and substituting these expressions into the equation of the medium motion, we obtain a differential equation for the x projection of the displacement vector of the medium (u_x). Taking into account the fact that the plate surfaces are stress-free, a solution to this equation has the following form:

$$u_x(x) = \frac{1}{k}\left(\left(\frac{\cos(kL)-1}{\sin(kL)}\right)\cos(kx) + \sin(kx)\right) \times (d_{31}E_3 + q_{31}H_3), \quad (5)$$

where $k = \omega(\rho s_{11})^{1/2}$ is a parameter and ρ is the effective density of the composite. For the transverse field orientation, the expression for u_x contains q_{11} instead of q_{31}.

The electric field arising due to the piezoelectric effect can be found from Eqs. (2) (for the longitudinal field orientation) and (4) (for the transverse field orientations) by using the open circuit condition. Expressing the components of the stress tensor from (1) and (3) via the strain tensors, using a solution for u_x, and substituting these expressions into (2) and (4), respectively, we obtain an expression for E_z. Defining the magnetoelectric coefficient as $E_3 = \alpha_{E,L}H_3$ and $E_3 = \alpha_{E,T}H_1$ (for longitudinal and transverse field orientations, respectively), we obtain the expressions

$$\alpha_{E,L} = \frac{1}{\Delta_a}\left(\frac{d_{31}q_{31}}{\varepsilon_{33}s_{11}}(1 + \tan(\kappa)/\kappa) - \frac{\alpha_{33}}{\varepsilon_{33}}\right), \quad (6)$$

$$\alpha_{E,T} = \frac{1}{\Delta_a}\left(\frac{d_{31}q_{11}}{\varepsilon_{33}s_{11}}(1 + \tan(\kappa)/\kappa) - \frac{\alpha_{31}}{\varepsilon_{33}}\right); \quad (7)$$

where $\kappa = kL/2$ is a dimensionless parameter, $K_{31}^2 = d_{31}^2/(\varepsilon_{33}s_{11})$ is the square of the electromechanical coupling coefficient for the planar oscillations, and $\Delta_a = 1 - K_{31}^2(1 + \tan(\kappa)/\kappa)$.

From Eqs. (6) and (7), it is seen that, at the so-called antiresonant frequency when $\Delta_a = 0$, the ME coefficient sharply increases. In real structures, there are losses that take place mainly in the contacts. Therefore, it is necessary to introduce a term $i\Gamma$ responsible for damping into the expression for Δ_a. The antiresonant frequency is determined by the effective parameters of a material and the sample geometry (primarily by the plate length), the value of the compliance coefficient s_{11}, and the material density. Estimates show that, for ferrite spinel–lead zirconate titanate (PZT) composite plates with a length on the order of one centimeter, the antiresonant frequency is about 300 kHz.

Experimentally, the effect was investigated on the samples of a multilayer composite material consisting of eleven layers of nickel ferrite spinel (each layer was 13 μm thick) and ten layers of PZT piezoceramics (each layer was 26 μm thick). The samples had a rectangular shape 7.3 mm in length and 2.15 mm in width. First, we studied the dependence of the low-frequency ME effect on the intensity of a constant magnetic field. Next, for the bias field intensity corresponding to the maximum of the effect, we recorded the frequency dependence of the ME coefficient in the vicinity of the electromechanical resonance for both longitudinal and transverse orientations of the magnetic and electric fields.

The experimental data and theoretical curves calculated using formulas (6) and (7) are presented in Figs. 1a and 1b, respectively. In our calculations, we used the following values of the parameters. For nickel ferrite spinel: $s_{11} = 6.5 \times 10^{-12}$ m^2/N, $q_{31} = 125 \times 10^{-12}$ m/A, $q_{11} = -680 \times 10^{-12}$ m/A, and $\varepsilon_{33}/\varepsilon_0 = 10$; for PZT: $s_{11} = 15.3 \times 10^{-12}$ m^2/N, $d_{31} = -175 \times 10^{-12}$ m/V, and $\varepsilon_{33}/\varepsilon_0 = 1750$. The effective parameters of the composite were calculated according to the method described in [4], and the damping parameter was found from the electromechanical resonance line width. In the calculations, the value of the damping parameter was taken equal to $\Gamma = 0.2$. As is seen from data in the figures, there is a good agreement between the theoretical

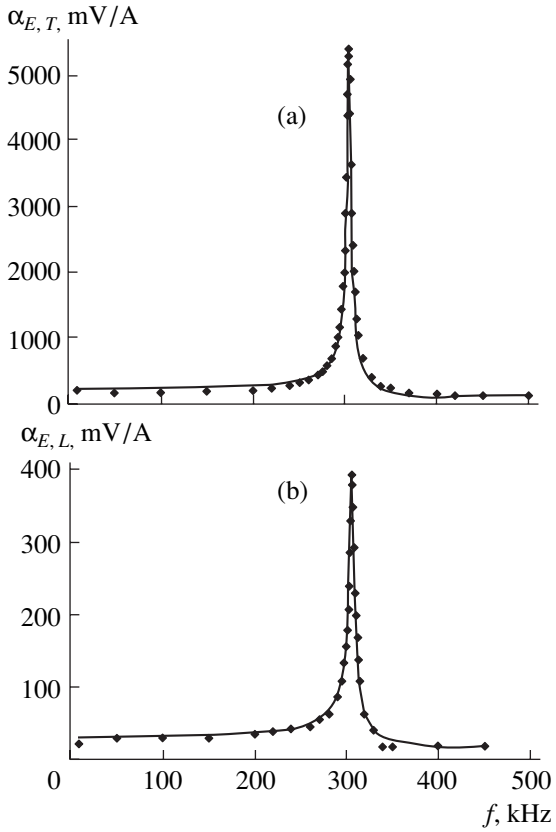

Fig. 1. Frequency dependence of the ME coefficient for the (a) transverse and (b) longitudinal field orientation (solid lines show the results of theoretical calculations and symbols represent the experimental data).

dependence and the experimental results. At a frequency near 300 kHz, the resonant enhancement of the ME effect is observed. The maximum value of the ME coefficient (5200 mV/A) is observed for the transverse field orientation, whereas the value at a frequency of 100 Hz is 180 mV/A. Thus, the resonant value of the ME coefficient exceeds the low-frequency value by a factor of about 30. For the longitudinal field orientation, the magnitude of the ME effect is one order of magnitude smaller. This is explained by the fact that, for the longitudinal field orientation, the ME effect is significantly affected by demagnetizing fields.

Thus, the magnitude of the ME effect near the electromechanical resonance exceeds a low-frequency value by more than an order of magnitude. For a multilayer nickel ferrite spinel–PZT composite, the value of the ME coefficient exceeds 5 V/A. This makes possible practical applications of the ME effect, which were previously hindered by values of the ME coefficient that were too small.

Acknowledgments. This study was supported in part by the Ministry of Education of the Russian Federation (project no. E02-3.4-278), the Program "Universities of Russia" (project no. UR 01.01.007), and the US National Science Foundation (DMR-0322254).

REFERENCES

1. M. I. Bichurin, D. A. Filippov, V. M. Petrov, and G. Srinivasan, in *Proceedings of the International Conference on the Physics of Electronic Materials, Kaluga, 2002*, p. 309.
2. D. A. Filippov, M. I. Bichurin, V. M. Petrov, and G. Srinivasan, Bull. Am. Phys. Soc. **48**, 214 (2003).
3. A. M. J. G. van Run, D. R. Terrell, and J. H. Scholing, J. Mater. Sci. **9**, 1710 (1974).
4. M. I. Bichurin, V. M. Petrov, and G. Srinivasan, J. Appl. Phys. **92**, 7681 (2002).

Translated by Yu. Vishnyakov

Technical Physics Letters, Vol. 30, No. 1, 2004, pp. 60–63. Translated from Pis'ma v Zhurnal Tekhnicheskoĭ Fiziki, Vol. 30, No. 2, 2004, pp. 43–51.

Accelerated Mechanical Alloying of Mutually Insoluble Metals: Co–Cu System

R. S. Iskhakov*, L. A. Kuzovnikova, S. V. Komogortsev, E. A. Denisova, A. D. Balaev, V. K. Mal'tsev, and G. N. Bondarenko

Kirensky Institute of Physics, Siberian Division, Russian Academy of Sciences, Krasnoyarsk, Russia

Krasnoyarsk Branch, Irkutsk State University of Railway Communications, Krasnoyarsk, Russia

Institute of Chemistry and Chemical Technology, Siberian Division, Russian Academy of Sciences, Krasnoyarsk, Russia

** e-mail: rauf@iph.krasn.ru*

Received May 22, 2003; in final form, July 28, 2003

Abstract—We propose a new method for accelerating the process of mechanical alloying in the Co–Cu system possessing positive enthalpy of mixing and exhibiting no mutual solubility of components under equilibrium conditions. For this purpose, highly disperse powders of composite particles representing a Co–P amorphous alloy core covered with a nanocrystalline copper shell were prepared by chemical deposition. These composite powders were mechanically alloyed by processing in a ball mill. Investigation of the atomic structure and magnetic properties of the composite powders upon milling showed that the formation of supersaturated Co–Cu solid solutions under such conditions requires a much shorter milling time as compared to that for the conventional mechanical alloying processes. *© 2004 MAIK "Nauka/Interperiodica".*

In the last decade, nanocrystalline alloys based on the combinations of elements immiscible under equilibrium thermodynamic conditions, such as (Co, Fe)–(Cu, Au, Ag), have been extensively studied. Prepared by various nonequilibrium methods, these alloys exhibit a number of anomalous physical properties with good prospects for application in practice [1–8]. An example is offered by alloys of the Co–Cu system obtained by magnetron sputtering [2, 3], rapid quenching from melt [4], and prolonged grinding of metal powders in special ball mills (mechanical alloying) [5–8].

The method of mechanical alloying has drawn the special attention of researchers due to the apparent simplicity and still unclear mechanism of alloy formation. Using this method, metastable Co–Cu solid solutions of various compositions with a grain size of 5–20 nm and an excess energy level of up to 10 kJ/mol were obtained [5–8] from mixtures of metallurgical Co and Cu powders with a particle size of 70–150 μm. The required milling time varied from 20 to 50 h, depending on the activator power. It was found that further milling does not change the alloy microstructure, which indicates that a dynamic equilibrium is established between breakage and restoration of a chemically homogeneous structure in metastable solid solutions. Considerable time and mechanical work consumed during milling are spent for the formation of a special contact interface between particles in the reaction mixture.

In this Letter, we propose a means of accelerating the process of alloy formation between cobalt and copper while obtaining metastable Co–Cu solid solutions by means of milling (mechanical alloying). Using the proposed method, the milling time can be reduced to less than one-tenth of that required for the conventional processing technology.

Reaction mixtures for the mechanical alloying of Co and Cu were prepared in the form of ultrafine powders consisting of composite particles representing a $Co_{88}P_{12}$ amorphous alloy core with a nanocrystalline copper shell. The $(Co_{88}P_{12})_{100-X}/Cu_X$ (X = 20 or 50 at. %) composite powders were obtained by method of combined chemical deposition based on the reduction of metals from aqueous solutions of the corresponding salts. In the first step, ultrafine Co–P powders were obtained from an aqueous solution of $CoSO_4$ by reduction at T = 80°C with sodium hypophosphite NaH_2PO_2 [9]. The content of phosphorus was determined by chemical analysis with an error of ±0.5 at. %. Previously [9], it was established that $Co_{88}P_{12}$ powders obtained using this method are amorphous and consist of spherical particles with diameters in the range from 0.1 to 3 μm. In the second step, $Co_{88}P_{12}$ amorphous alloy particles were coated with nanocrystalline copper shells of various thicknesses. The reducing agent in solutions for the copper plating of Co–P powder was formaldehyde.

1063-7850/04/3001-0060$26.00 © 2004 MAIK "Nauka/Interperiodica"

Mechanical alloying was achieved by processing composite powders in hermetically sealed containers in a planetary ball mill (AGO-2U). The duration of milling with steel balls at an acceleration of 20*g* and a ball to powder weight ratio of 10 : 1 was t_m = 0.5, 1, 2, 3, or 4 h.

The atomic structure of the alloys obtained by milling was studied by X-ray diffraction on a DRON-3 diffractometer using CuK_α radiation. Note that, according to the accepted notions, the X-ray diffraction data cannot be used for the final judgment on the formation of chemically homogeneous solid solutions in a system of mutually insoluble components. Indeed, the change in the interplanar distances determined from the diffraction patterns can be related both to the formation of a solid solution and, for example, to a coherent fitting of the crystal lattice of ultrasmall particles of one component to the crystal lattice of another (matrix) component [6].

For this reason, the atomic structure of the obtained Co–Cu alloy was additionally characterized using the nuclear magnetic resonance (NMR) and low-temperature magnetization $M(T)$ measurements. These methods provide data on the short-range order and the environment of Co atoms in the crystal lattice. The room-temperature NMR spectra were recorded on a standard spin-echo spectrometer operating in a frequency range from 150 to 230 MHz. The low-temperature magnetization measurements were performed in a temperature range from 4.2 to 200 K on a vibrating-sample magnetometer with an applied field of 20 kOe.

The X-ray diffraction patterns were obtained for the initial reaction mixtures charged into the ball mill and for the samples processed in the mills for each preset milling time t_m. The reaction mixtures were either a mechanical mixture of highly disperse Co–P and Cu powders or the $(Co_{88}P_{12})_{80}/Cu_{20}$ and $(Co_{88}P_{12})_{50}/Cu_{50}$ composite powders (Fig. 1a). The results of these measurements showed that a 2-h processing of the mixture of Co–P and Cu powders did not produce any significant change in the atomic structure: the amorphous component (Co–P) remains amorphous and the diffraction peaks of Cu exhibit broadening while retaining their angular positions.

A different situation is observed in the course of milling of the composite powders. Here, even a 0.5-h processing brings significant structural changes. As can be seen from the diffractograms of these samples (Fig. 1a shows the diffraction patterns for the $(Co_{88}P_{12})_{50}/Cu_{50}$ composite), the main phase of the material has an fcc structure with the interplanar distances (directly related to the angular positions of the diffraction reflections by the Bragg formula $d_{hkl} = \lambda/2\sin\Theta$) smaller than in fcc Cu but greater than in fcc Co. This fact is indicative of the Co–Cu alloy formation. Subsequent milling is accompanied by an insignificant decrease in the interplanar spacing (which always remains smaller than that in fcc Cu) and by broadening of the diffraction lines.

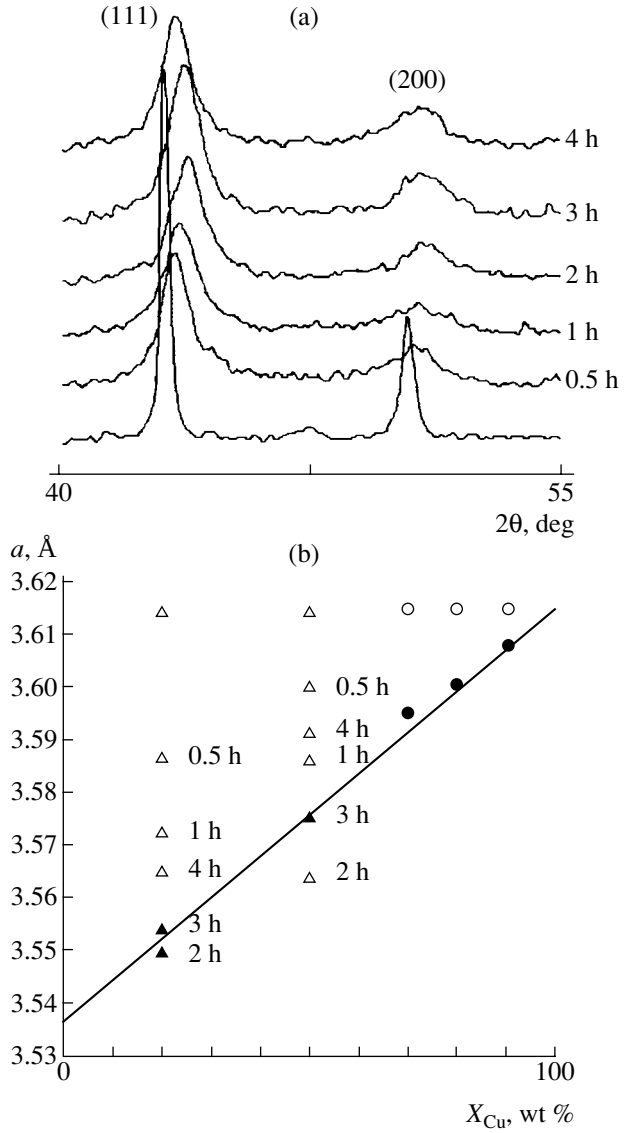

Fig. 1. X-ray diffraction study of a $(Co_{88}P_{12})_{50}/Cu_{50}$ composite powder: (a) diffractograms measured in various stages of mechanical alloying (figures at the curves indicate the milling time t_m); (b) variation of the lattice parameter of copper *a* in the course of mechanical alloying (Δ, this study; ○, data of [8] (initial and after 50-h milling); solid line corresponds to the Vegard law; black symbols correspond to alloys most close to the state of solid solution.

The results of X-ray diffraction measurements are summarized in Fig. 1b. As can be seen, the alloys obey the Vegard law. Note that a 2- to 3-h milling of the composite powder renders the state of the Co–Cu solid solution analogous to that observed after a 50-h conventional mechanical alloying of a mixture of metallurgical powders.

Thus, the main physicochemical factors responsible for the accelerated mechanical alloying of composite

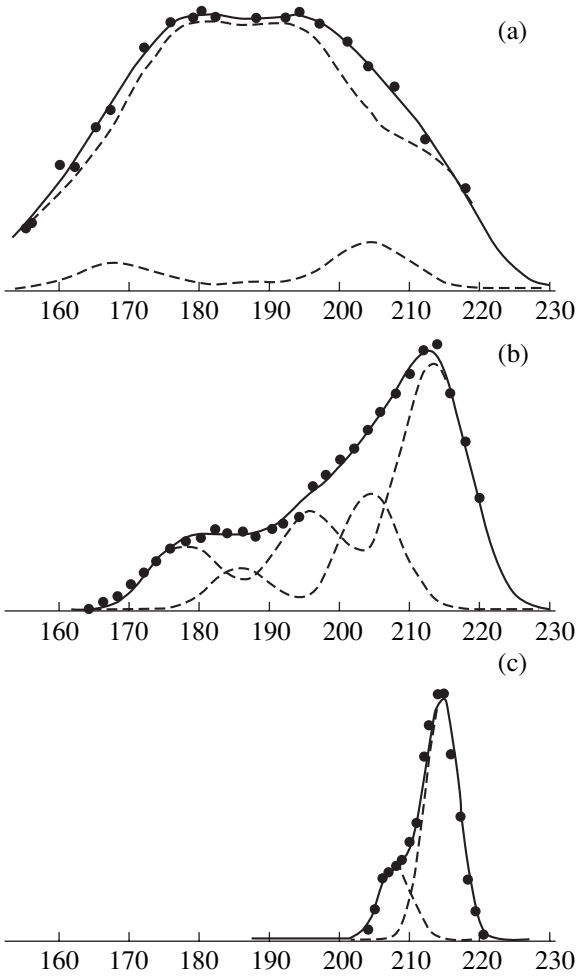

Fig. 2. Variation of the NMR spectra of a $(Co_{88}P_{12})_{50}/Cu_{50}$ composite powder: (a) initial powder; (b) after milling for t_m = 0.5 h; (c) after milling for t_m = 4 h and annealing for 1 h at T = 500°C (dashed curve show the results of deconvolution into components).

powders is the special character of interface between alloy components in these particles. This conclusion follows from a comparison of the diffractograms of the mechanical mixture of Co–P and Cu powders and the patterns observed for the composite powders.

Figure 2 shows the NMR spectrum of the initial $(Co_{88}P_{12})_{50}/Cu_{50}$ composite powder and changes in this spectrum upon the first 0.5-h milling and after a 4-h milling followed by annealing for 1 h at 500°C. The NMR spectrum of pure Co contains two main components corresponding to the resonances at 213.5 MHz (fcc Co) and 221 MHz (hcp Co). The nearest environment of Co in both fcc and hcp lattices includes 12 neighbors. When the magnetic neighbors are replaced by nonmagnetic ones, the NMR spectrum displays equidistant satellites. Deconvolution of the NMR spectrum of the initial powder into components shows that Co atoms occur primarily in an fcc environment including one or two nonmagnetic neighbors (Fig. 2a).

Already the first 0.5-h milling of the $(Co_{88}P_{12})_{50}/Cu_{50}$ composite powder leads to a significant change in the NMR spectrum (Fig. 2b): the main resonance now corresponds to pure fcc Co (which is evidence for the crystallization of the initially amorphous Co) and there appears a satellite reflecting the hcp Co environment. After a 1-h processing, the total NMR signal intensity decreases, but the shape of the spectrum also indicates the presence of Co in both fcc and hcp environments. After 2-h and 4-h milling, the room-temperature NMR signal vanishes and appears again only after a 1-h annealing at 500°C, representing a sum of two resonance components (Fig. 2c). One of these components corresponds to pure fcc Co (213.5 MHz), and the other (208 MHz), to a Co-based solid solution with an hcp structure featuring one nonmagnetic atom in the first coordination sphere of Co. Since phosphorus atoms in the sample annealed at T = 500°C enter a phosphide phase (Co_2P) and do not contribute to NMR, the role of a nonmagnetic neighbor in the environment of Co is played by Cu. The component at 208 MHz corresponds to a $Co_{92}Cu_8$ solid solution with an hcp structure.

The above NMR data indicate that milling is accompanied by a polymorphous transformation (fcc–hcp) in the nearest environment of cobalt. These local martensitic shifts probably favor a significant increase in the coefficients of heterodiffusion of the alloy components. In addition, an analysis of the NMR spectra suggests the possible formation of copper phosphide (Cu_2P) together with cobalt phosphide (Co_2P).

The typical low-temperature magnetization curve $M(T)$ of the $(Co_{88}P_{12})_{100-X}/Cu_X$ composite powder (Fig. 3) shows that the alloy contains both the regions of solid solution rich in Co (ferromagnetic phase) and the regions where separate Co atoms and small clusters are not coupled by exchange (superparamagnetic phase). The experimental $M(T)$ curve can be approximated by the following expression:

$$M(T) = a_0 - a_1 T^{3/2} + a_2 L\left(\frac{a_3}{T}\right), \qquad (1)$$

where $L(x) = \coth(x) - 1/x$ is the Langevin function. The first two terms in this expression, describing a decrease in the magnetization of the ferromagnetic (FM) phase related to the spin waves, correspond to the Bloch "3/2" law: $a_0 - a_1 T^{3/2} \equiv M_f v_f (1 - BT^{3/2})$, where M_f is the average magnetization of the ferromagnetic component, v_f is the volume fraction of this component, and $B \sim A^{-2/3}$ is the average Bloch constant related to the effective exchange coupling constant A [10]. The third term in Eq. (1) describes a decrease in the magnetic susceptibility of the superparamagnetic phase that corresponds to the Langevin law [11]: $a_2 L(a_3/T) \equiv M_{sp} v_{sp} L(M_{sp} H V_{sp}/(kT))$, where M_{sp} is the average

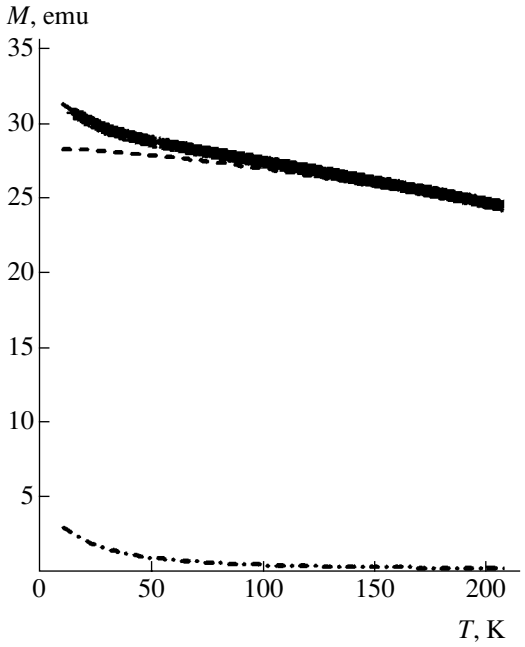

Fig. 3. The typical low-temperature magnetization curve $M(T)$ of a composite powder measured in an external magnetic field of $H = 20$ kOe. Solid curve shows the approximation according to formula (1); dash and dot-dash curve correspond to the ferromagnetic and superparamagnetic components in formula (1). This example refers to a $(Co_{88}P_{12})_{50}/Cu_{50}$ composite powder milled for $t_m = 4$ h.

magnetization of the superparamagnetic component, v_{sp} is the volume fraction of this component, and V_{sp} is the average volume of a superparamagnetic particle.

Expression (1) describes the experimental $M(T)$ curve well (Fig. 3). The values of parameters a_0, a_1, a_2, and a_3 were determined, but detailed analysis of the low-temperature magnetization behavior is beyond the scope of this paper. Here, let us consider the Bloch constant $B = a_1/a_0$. For the initial $(Co_{88}P_{12})_{80}/Cu_{20}$ composite powder, this quantity amounts to $B = 6.5 \times 10^{-6}$ K$^{-3/2}$. In the course of milling, this value is almost doubled to reach $B = 13.9 \times 10^{-6}$ K$^{-3/2}$ at $t_m = 1$ h (further milling does not significantly change this value: $B = 14.7 \times 10^{-6}$ K$^{-3/2}$ at $t_m = 4$ h). For the initial $(Co_{88}P_{12})_{50}/Cu_{50}$ composite powder, the Bloch constant also equals $B = 6.5 \times 10^{-6}$ K$^{-3/2}$. In the course of milling, this value first exhibits a sevenfold growth to reach $B = 43.3 \times 10^{-6}$ K$^{-3/2}$ at $t_m = 2$ h and then varies only slightly to reach $B = 48.4 \times 10^{-6}$ K$^{-3/2}$ at $t_m = 4$ h. Since the magnitude of the exchange coupling constant A (determining the B value) is related to the nearest environment of Co atoms, the changes in B observed for the composite powders during the initial milling for 1–2 h are naturally attributed to the formation of Co–Cu solid solutions.

According to the published data on the mechanical alloying of Co and Cu, the characteristic times of milling after which the formation of a Co–Cu solid solution takes place amount to ~20 h and above [5–8]. The new method proposed in this paper allows the solid solution to be obtained after milling for $t_m = 2$–3 h, which significantly reduces the energy consumption for the mechanical alloying of Co and Cu.

REFERENCES

1. S. D. Kaloshkin, I. A. Tomilin, E. V. Shelekhov, *et al.*, Fiz. Met. Metalloved. **84** (3), 68 (1997).
2. H. Errahmani, N. Hassanain, A. Berrada, *et al.*, J. Magn. Magn. Mater. **241**, 335 (2002).
3. J. R. Childress and C. L. Chien, Phys. Rev. B **43**, 8089 (1991).
4. P. Panissod, M. Malinowska, E. Jedryka, *et al.*, Phys. Rev. B **63**, 014408 (2000).
5. C. Gente, M. Oehring, and R. Bormann, Phys. Rev. B **48**, 13244 (1993).
6. M. A. Uimin, A. Ye. Yermakov, V. V. Serikov, *et al.*, Phys. Status Solidi A **165**, 337 (1998).
7. J. Y. Huang, Y. K. Wu, A. Q. He, *et al.*, Nanostruct. Mater. **4**, 293 (1994).
8. Y. Ueda, S. Ikeda, and S. Chikazawa, Jpn. J. Appl. Phys. **35**, 3414 (1996).
9. R. S. Iskhakov, L. A. Chekanova, and E. A. Denisova, Fiz. Tverd. Tela (St. Petersburg) **41**, 464 (1999) [Phys. Solid State **41**, 416 (1999)].
10. R. S. Iskhakov, G. V. Popov, and M. M. Karpenko, Fiz. Met. Metalloved. **56** (1), 85 (1983).
11. S. V. Vonsovskiĭ, *Magnetism* (Nauka, Moscow, 1971; Wiley, New York, 1974).

Translated by P. Pozdeev

Technical Physics Letters, Vol. 30, No. 1, 2004, pp. 64–67. Translated from Pis'ma v Zhurnal Tekhnicheskoĭ Fiziki, Vol. 30, No. 2, 2004, pp. 52–60.

The Effects of Temporal and Longitudinal Spatial Coherence in a Disbalanced-Arm Interferometer

V. P. Ryabukho, D. V. Lyakin, and M. I. Lobachev

Institute of Precision Mechanics and Control, Russian Academy of Sciences, Saratov, Russia

e-mail: rvp@sgu.ru

Received July 7, 2003

Abstract—During the interference of optical fields possessing broad frequency and angular spectra in an oscillating-mirror Michelson interferometer, the presence of a film introducing an additional optical path increment in one of the arms leads to a mutual shift (recession) of the signals of temporal and longitudinal spatial coherence. This phenomenon leads to breakage of the mutual coherence of the interfering fields. In the presence of two light sources, this effect can be used for the independent determination of the thickness and refractive index of the film. © *2004 MAIK "Nauka/Interperiodica".*

The interference of optical fields in a scanning interferometer employing a light source with broad frequency spectrum leads to the formation of an interference signal with the duration determined (in terms of the optical path difference Δ) by the temporal coherence length $l_c \approx \lambda_0^2/\Delta\lambda$ [1]. The position of the maximum of the signal envelope (determined by the temporal coherence modulus $|\gamma_{11}(\Delta)|$) coincides with the zero optical path difference ($\Delta = 0$). When an optically thick film is introduced into one of the interferometer arms, the interference signal shifts relative to the initial position by a value corresponding to the additional path difference Δ_1 and exhibits a change in shape related to the dispersion $n(\lambda)$ of the film material [2–6].

This study was aimed at an analysis of the effect of the longitudinal spatial coherence on the interference signal formation [7–9], which is manifested if the optical field possesses a sufficiently large angular spectrum in the region of interference signal detection (or if the light source has a large angular size).

The experiments were performed with a Michelson interferometer in which one of the mirrors performed oscillations along the optical axis (Fig. 1). The oscillation amplitude l_0 was sufficient for the manifestation of both temporal and longitudinal spatial coherence of light: $2l_0 \gg l_c$ and $2l_0 \gg \rho_\parallel$ ($\rho_\parallel$ is the longitudinal spatial coherence length estimated by the relation $\rho_\parallel \approx 2\lambda_0/\theta^2$, where 2θ is the angular aperture of the light beam in the detection plane) [7, 8]. The mirror-drive mechanism excluded tilts relative to the optical axis, so that the transverse shifts $\Delta\rho$ of the optical field in the detection plane could be ignored: $\Delta\rho \ll \rho_\perp$, where $\rho_\perp \approx \lambda_0/2\theta$ is the transverse spatial coherence radius. The modulated output signal $\tilde{u}_p(t)$ of the detector was fed to an oscillograph locked-in with the mirror-drive mechanism. Simultaneously, the output signal was digitized at 2.5 MHz and transmitted to a computer for storage and analysis.

For simultaneous separate observation of the output signal components related to the manifestation of only the temporal or the longitudinal spatial coherence, we used two light sources: a superluminescent LED ($\lambda_0 \approx 0.85$ μm), $\Delta\lambda \approx 0.02$ μm) with collimated beam and a low-pressure sodium-vapor lamp (DNAS-18) with a sufficiently extended emitting area and a large temporal coherence length of light in the region of a yellow doublet ($l_c = \lambda_1\lambda_2/\Delta\lambda_{12} \approx 600$ μm, where $\lambda_1 = 0.589$ μm and

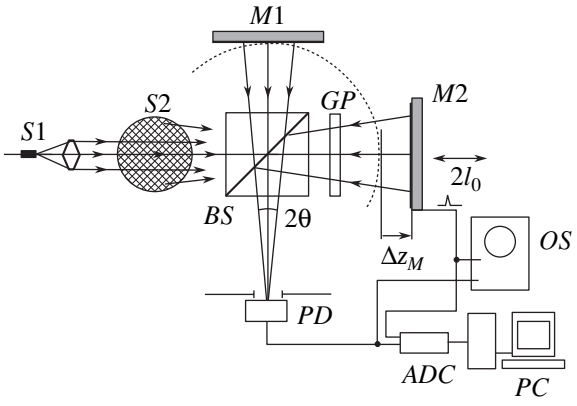

Fig. 1. Schematic diagram of the oscillating-mirror Michelson interferometer with two light sources *S*1 (a broadband superluminescent LED) and *S*2 (a quasimonochromatic extended gas-discharge sodium vapor lamp): (*M*1) flat mirror smoothly adjustable in the longitudinal direction; (*M*2) flat mirror oscillating with an amplitude of l_0; (*BS*) beam splitter; (*GP*) plate-parallel plate; (*PD*) photodetector; (*OS*) oscillograph; (*ADC*) analog-to-digital signal converter; (*PC*) computer.

$\lambda_2 = 0.5896$ μm). Thus, the aperture of a photodetector adjusted at the optical axis of the system simultaneously received two pairs of interfering light beams: an almost collinear pair with a small temporal coherence length ($l_c \approx 36$ μm) and the pair with a rather big angular aperture ($2\theta \approx 0.2$ rad) and a relatively large temporal coherence length. In the course of oscillations of mirror $M2$, these pairs of beams formed two independent interference signals. By smoothly adjusting mirror $M1$, it was possible to move the interference signals to a position convenient for digital recording.

An additional optical layer with variable optical thickness d in the interferometer arms was modeled by a special beam splitting cube, in which one half-prism could be smoothly shifted along the division (hypotenuse) face. This introduced an uncompensated optical path into the corresponding interferometer arm (Fig. 1).

Figure 2 shows the digital oscillograms of the interference signals representing the temporal (1) and spatial (2) coherence reflected on the optical path scale $\Delta = 2\Delta z_M(t)$, where Δz_M is the longitudinal displacement of mirror $M2$. The signals displayed in Figs. 2a and 2b correspond to the presence of an additional layer in the first arm ($M1$) of the interferometer. In Fig. 2c, the two signals almost coincide, which corresponds to compensation of the optical paths in the interferometer ($d = 0$), and in Fig. 2d, the additional layer appears in the second arm ($M2$) of the interferometer. Mutual superimposition of the signals in Figs. 2b and 2c gives rise to spatial beats of the interference oscillations.

An uncompensated optical path introduces additional time delay [4], equal to $\delta t \approx \Delta_1/c = 2d(n-1)/c$ (where c is the velocity of light and n is the group refractive index), corresponding to a spatial shift $\Delta_1 = 2d(n-1)$ of the wave trains upon double passage through the additional layer. The amplitude–phase structure of the optical field in the output arm of the interferometer exhibits an advancing longitudinal spatial shift δz in the opposite direction. To the first approximation, the magnitude of this shift can be evaluated as $\delta z \approx 2d(n-1)/n$. The influence of the longitudinal shift becomes significant in the field with a relatively small longitudinal spatial coherence length $\rho_\parallel \approx \delta z$.

Figure 3a shows the propagation of light beams with a broad angular spectrum through a plane-parallel transparent layer. Here, $U_1(\boldsymbol{\rho}, z, t)$ and $U_2(\boldsymbol{\rho}, z, t)$ are the complex field amplitudes in the absence of this layer and in the presence of a layer with the optical thickness dn, respectively. We can write the latter amplitude as $U_2(\boldsymbol{\rho}, z, t) \approx U_1(\boldsymbol{\rho}, z - \delta x, t + \delta t)$, where the approximate equality implies a certain decorrelation of the complex field amplitude $U_1(\boldsymbol{\rho}, z, t)$ produced by the transparent layer due to the dispersion $n(\lambda)$ of the layer material and the spherical aberration of light transmitted through the layer. For the more clear illustration of processes under consideration, Fig. 3b gives a scheme of the interferometer and shows mutual spatial arrangement of the identical wave trains in the interfering fields and their identical amplitude–phase structures upon the introduction of an additional layer of optical thickness dn into the initially equal-arm interferometer.

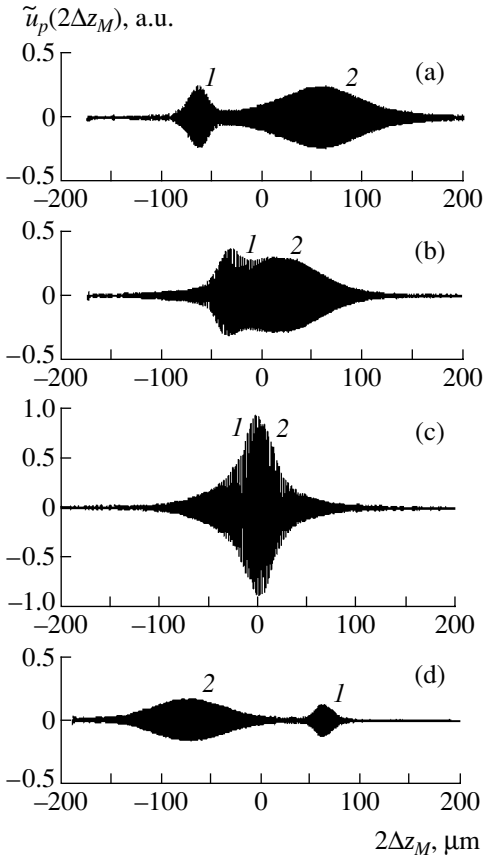

Fig. 2. Oscillograms of the interference signals of the (*1*) temporal and (*2*) longitudinal spatial coherence on the optical path scale $2\Delta z_M$, observed upon introduction of an additional layer of the optical thickness dn into the interferometer arm with mirror $M1$ (a, b) or $M2$ (d); oscillogram (c) corresponds to $d \approx 0$.

In the presence of an additional optical layer in the second arm of the interferometer (see Fig. 1), the mutual shift Δ_1 of the wave trains (corresponding to the time delay δt) is compensated by displacing mirror $M2$ away from beam splitter BS by a distance of $d(n-1)$. On the other hand, the longitudinal shift of the amplitude–phase field structures is compensated and the interference signal of the longitudinal spatial coherence is observed upon moving mirror $M2$ toward beam splitter BS by the distance $\delta z \approx d(n-1)/n$ (Fig. 2d). If the layer GP appears in the other arm of the interferometer (containing mirror $M1$), compensation of the aforementioned shifts will require moving mirror $M2$ in the directions opposite to those indicated above (Figs. 2a and 2b). Thus, introduction of an additional optical layer into one of the interferometer arms leads to the mutual shift (recession) of the signals of temporal and longitudinal spatial coherence.

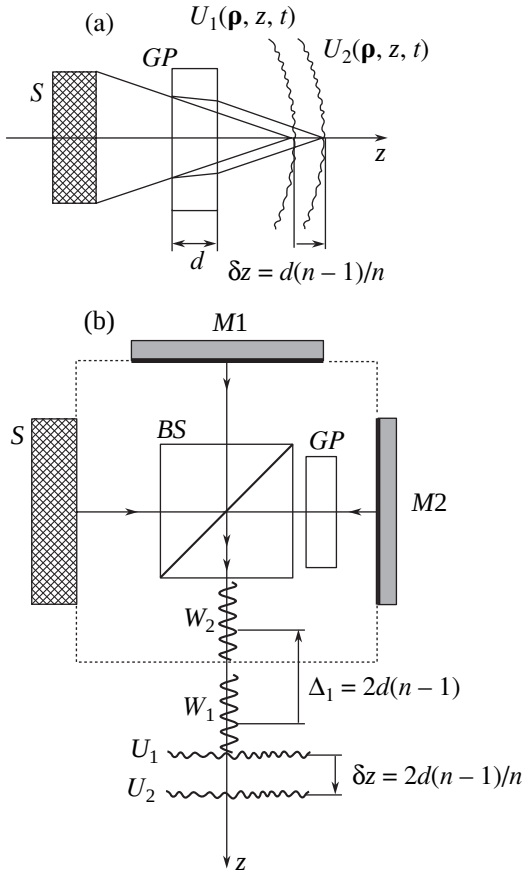

Fig. 3. Schematic diagrams illustrating (a) a longitudinal shift of the amplitude–phase structure of the optical field with a broad angular spectrum and (b) mutual shift of the identical wave trains (W_1, W_2) and the identical amplitude–phase structures (U_1, U_2) of the optical fields at the interferometer output upon introduction of a transparent layer with the optical thickness dn into one of the arms: (*S*) extended light source; (*BS*) beam splitter; (*M*1, *M*2) flat mirrors; (*GP*) plane-parallel plate. See the text for explanations.

A decrease in the amplitude of interference oscillations in the signals of temporal and longitudinal spatial coherence, which is observed upon increasing the optical layer thickness in one of the arms (Figs 2a, 2b, and 2d), is caused by a decrease in the mutual coherence of waves related to the influence of the dispersion $n(\lambda)$ of the layer material and the spherical aberration of light in the layer.

The phenomenon of recession of the interference signals of the temporal and longitudinal spatial coherence, observed using two light sources with close values of the average wavelength, can be used for independent determination of the thickness d and the group refractive index n of the additional optical layer [10]. Indeed, let us measure both a shift of the temporal coherence signal $\Delta_1 \approx 2d(n-1)$ and a displacement of the longitudinal spatial coherence signal $\delta z \approx 2d(n-1)/n$ caused by the introduction of layer with the optical thickness dn into one arm of the initially equal-arm oscillating-mirror interferometer. Then, the geometric thickness d and the refractive index n can be determined using the formulas $d \approx 0.5\Delta_1\delta z/(\Delta_1 - \delta z)$ and $n \approx \Delta_1/\delta z$. For example, the signal depicted in Fig. 2d corresponds to a layer with the thickness $d \approx 90$ μm and the group refractive index $n \approx 1.5$.

If the interferometer employs only one extended light source with a broad frequency spectrum, which forms an optical field with a sufficiently wide angular spectrum in the detection plane, the envelope of the alternating component $\tilde{u}_p$ of the interferometer signal will be determined (within a certain approximation) by the product of the temporal coherence modulus $\gamma_{11}(2\Delta z_M(t) \pm 2d(n-1))$ and the spatial coherence modulus $\gamma_{12}(\delta z(t) \mp 2d(n-1)/n)$:

$$\begin{aligned}\tilde{u}_p(t) \sim &\left|\gamma_{11}(2\Delta z_M(t) \pm 2d(n-1))\right| \\ &\times \left|\gamma_{12}(\delta z(t) \mp 2d(n-1)/n)\right| \\ &\times \cos\left[\frac{4\pi}{\lambda_0}(\Delta z_M(t) \pm d(n-1)) + \Delta\varphi_0\right],\end{aligned} \quad (1)$$

where $\Delta\varphi_0$ is the initial phase difference. The presence of a plane-parallel layer plate in one of the interferometer arms leads to the combined manifestation of both temporal and longitudinal spatial coherence and results in the disappearance of the interference signal when $2d(n-1) \approx l_c$ (for $l_c < \rho_\parallel$) or when $2d(n-1)/n \approx \rho_\parallel$ (for $l_c > \rho_\parallel$). In the former case ($l_c < \rho_\parallel$), the mutual delay between wave trains in the interferometer arms is compensated and the mutual temporal coherence is restored when mirror *M*2 is displaced toward beam splitter *BS* by $\Delta z_M \approx d(n-1)$. This displacement leads to the corresponding longitudinal shift $2d(n-1)$ of the wave field at the interferometer output, after which the total mutual longitudinal shift of the interfering wave fields will be equal to $\delta z \approx 2d(n-1)/n + 2d(n-1)$. If the longitudinal spatial coherence radius $\rho_\parallel$ is smaller than δz, so that $\rho_\parallel < 2d(n^2-1)/n$, the mutual coherence is not restored and the interference signal is not observed irrespective of the mirror displacement. However, since $\rho_\parallel \approx 2\lambda/\theta^2$, the mutual coherence can be restored by decreasing θ (e.g., by shifting the observation plane away from beam splitter *BS*), after which the interference signal will be observed.

Analogous considerations are valid in the case when $l_c > \rho_\parallel$ and the longitudinal field coherence is limited by the spatial coherence length. In order to compensate the longitudinal shift $\delta z \approx 2d(n-1)/n$ of the wave field caused by the appearance of the optical layer in the interferometer arm, it is necessary to displace mirror *M*2 away from beam splitter *BS* by the same distance. As a result, the path difference increases to $\Delta \approx 2d(n-1) + 2d(n-1)/n$. Again, if this difference exceeds the coherence length l_c, the mutual coherence is not restored. In order to restore the interference signal, it is

necessary to increase l_c, for example, by filtration of the frequency spectrum of the radiation employed.

It should be noted that the effects considered above can be observed using scattered laser radiation with a sufficiently broad angular spectrum in combination with a broadband source of collimated light. Moreover, analogous phenomena can be observed during the interference of focused light beams with broad angular spectra, but this will require using a detector possessing a sufficiently wide integrating aperture [11].

Making allowance for the phenomena considered above in the investigation of processes involving the interference of optical fields with broad frequency and angular spectra (e.g., in low-coherence interferometry and tomography using focused low-coherence probing light beams) will provide for a more adequate interpretation of the results of interference measurements.

Acknowledgments. This study was supported by the Presidential Grant for Support of Leading Scientific Schools (no. NSh-25.2003.2) and by a grant from the US Civilian Research and Development Foundation for the Independent States of the Former Soviet Union (CRDF Award no. REC-006).

REFERENCES

1. L. Mandel and E. Wolf, *Optical Coherence and Quantum Optics* (Cambridge Univ. Press, Cambridge, 1995; Nauka, Moscow, 2000).
2. H. G. Danielmeyer and H. P. Weber, Phys. Rev. A **3**, 1708 (1971).
3. S. A. Akhmanov, Yu. E. D'yakov, and A. S. Chirkin, *Introduction to Statistical Radiophysics and Optics* (Nauka, Moscow, 1981).
4. V. A. Moskalev, *Theoretical Grounds of Optical–Physical Studies* (Mashinostroenie, Leningrad, 1987).
5. P. De Groot, Opt. Lett. **17**, 898 (1992).
6. C. K. Hitzenberger, A. Baumgartner, and A. F. Fercher, Opt. Commun. **154**, 179 (1998).
7. L. M. Soroko, *Fundamentals of Holography and Coherent Optics* (Nauka, Moscow, 1971).
8. J. Rosen and A. Yariv, Opt. Commun. **117**, 8 (1995).
9. J. Rosen and M. Takeda, Appl. Opt. **39**, 4107 (2000).
10. M. Ohmi, T. Shiraishi, H. Tajiri, and M. Haruna, Opt. Rev. **4**, 507 (1997).
11. V. P. Ryabukho, V. L. Khomutov, D. V. Lyakin, and K. V. Konstantinov, Pis'ma Zh. Tekh. Fiz. **24** (4), 19 (1998) [Tech. Phys. Lett. **24**, 132 (1998)].

Translated by P. Pozdeev

Technical Physics Letters, Vol. 30, No. 1, 2004, pp. 68–70. Translated from Pis'ma v Zhurnal Tekhnicheskoĭ Fiziki, Vol. 30, No. 2, 2004, pp. 61–65.

Optimization of the Plastic Relaxation of Misfit Stresses in Ge_xSi_{1-x}/Si(001) ($x \leq 0.61$) Heterostructures

Yu. B. Bolkhovityanov, A. S. Deryabin, A. K. Gutakovskiĭ, M. A. Revenko, and L. V. Sokolov*

Institute of Semiconductor Physics, Siberian Division, Russian Academy of Sciences, Novosibirsk, 630090 Russia

Tomsk State University, Tomsk, 634050 Russia

** e-mail: sokolov@isp.nsc.ru*

Received June 19, 2003

Abstract—High-quality Ge_xSi_{1-x}/Si(001) (x = 0.38–0.61) heterostructures (600–750 nm thick) with plastically relaxed mechanical stresses were grown by low-temperature molecular beam epitaxy. The total film thickness was reduced by using low-temperature growth and two-step variation of the Ge_xSi_{1-x} layer composition. High quality of the heterostructure is achieved due to the fact that misfit stresses between layers are released by dislocations passing from the first layer to the second. © *2004 MAIK "Nauka/Interperiodica"*.

Plastically relaxed Ge_xSi_{1-x}/Si(001) heterostructures are promising substrate materials both for the heteroepitaxy of $A^{III}B^{V}$ semiconductor films and for the growth of high-speed IC elements based on GeSi solid solutions. Stress-relieved heterostructures with $x \geq 0.3$ and a density of penetrating dislocations not exceeding 10^5–10^6 cm^{-2} are usually obtained under standard growth conditions (T = 500–550°C) either by means of multistep variation of the composition (Δx = 0.05–0.1 per step) [1, 2] or by forming a thick buffer layer with continuously increased germanium fraction [3, 4]. In both cases, a thick transition layer is formed that increases the cost and leads to greater surface roughness. A decrease in the transition layer thickness at a small change in the germanium fraction per step or a small composition gradient is hindered by the fact that sufficiently complete relaxation of the misfit stress is possible only within a thick (>1 μm) layer [5].

An alternative solution consists in the formation of a low-temperature buffer layer of silicon between the substrate and the GeSi film. Using this method, plastically relaxed $Ge_{0.3}Si_{0.7}$ films with a density of penetrating dislocations within 10^5–10^6 cm^{-2} were obtained with a transition layer thickness not exceeding 0.5 μm [6, 7]. However, as was pointed out in [8], this approach can be used only for x not exceeding 0.3. Thus, the problem of obtaining Ge_xSi_{1-x}/Si(001) heterostructures of limited thickness (~1 μm) and low density of dislocations for $x > 0.3$ still remains unsolved.

The large epilayer thickness necessary for the relaxation of mechanical stresses in epitaxial films grown under standard conditions is related to the barrier character of the nucleation of dislocations and to the lack of dislocations growing from silicon substrate, which would serve as the sources of misfit dislocations. A different situation takes place in a two-layer heterostructure, where the second layer with high germanium content is grown on an artificial substrate comprising a silicon substrate with the first layer of plastically relaxed Ge_xSi_{1-x}. In this case, misfit dislocations will form as a result of bending of the existing dislocations, penetrating through the boundary between two GeSi layers. Because of the absence of a nucleation threshold, this process begins when the second layer thickness only slightly exceeds the critical value. Thus, provided that the dislocation path length is sufficiently large, the relaxation of mechanical stresses in the second layer can be ensured only by the dislocations growing from the first layer. Therefore, it can be expected that the density of dislocations will not increase in the second stage of epitaxial growth.

Epilayers of Ge_xSi_{1-x} solid solution were grown in an molecular epitaxy system "Katun" equipped with an electron-beam evaporator generating the flux of Si atoms and a crucible for the evaporation of germanium. The deposition rates were 0.01–0.3 nm/s for Si and 0.006–0.04 nm/s for Ge, depending on the desired film composition. The types of structural defects and their spatial arrangement were studied using a Jeol JEM-4000EX electron microscope. The compositions of epitaxial layers and the degree of mechanical stress relaxation in these layers were determined from the X-ray rocking curves measured for (004), (115), (224), and (113) reflections [9]. The surface morphology of heterostructures was studied in a Solver P-47H atomic force microscope operating in the contact mode. The density of penetrating dislocations was determined upon etching heterostructures in an anisotropic etchant.

1063-7850/04/3001-0068$26.00 © 2004 MAIK "Nauka/Interperiodica"

The epitaxial growth cycle started with growing a 50-nm-thick buffer layer of silicon at $T = 700$°C. This layer is necessary to cover the contaminations and inhomogeneities retained on the substrate surface after preliminary cleaning. Then, a 50-nm-thick low-temperature buffer silicon layer was grown at $T = 350$°C. The epitaxial layers of Ge_xSi_{1-x} were grown in two steps. In the first step, the fraction of Ge atoms was selected so as to correspond to $x = 0.17$–0.20. This epilayer was covered with a 5-nm-thick layer of silicon, after which the structure was annealed for 1 h in order to provide for a more complete relaxation of misfit stresses. Special tests showed that the density of penetrating dislocations in such relaxed films upon annealing did not exceed 10^5 cm^{-2}. Then, the sample was cooled to the second-step growth temperature, a 50-nm-thick layer of Ge_xSi_{1-x} with the first-step composition was deposited, and the second layer with a high germanium content was grown. The growth regimes and the main parameters of heterostructures are presented in the table.

The electron-microscopic image of the cross section of sample 26 presented in the figure clearly reveals two layers of the Ge_xSi_{1-x} solid solution, separated from one another and from the substrate by dislocation networks. Small density of the penetrating dislocations in the second layer (~10^5 cm^{-2}, as determined by etch pits) is consistent with their absence in the image. According to the X-ray diffraction data, the first layer was stress-relaxed by 80%. The second layer, despite a small thickness and low growth temperature, was also plastically relaxed (which accounts for the misfit dislocation network formed at the interface). The degree of plastic relaxation in the second layer, according to the electron-microscopic images in plane, is no less than 40%. The films with such a misfit, grown on a silicon substrate at 350°C, remain pseudomorphous up to a thickness of 200 nm.

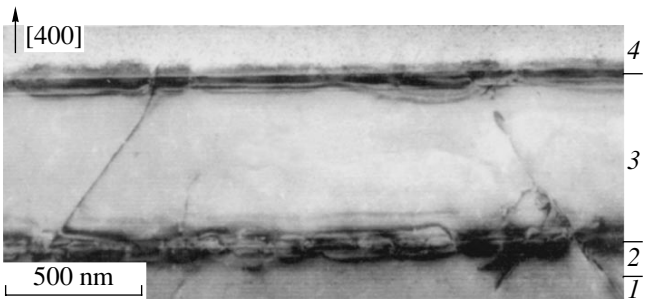

Electron-microscopic image of the cross section of a Ge_xSi_{1-x}/Si(001) heterostructure (sample D26): (*1*) silicon substrate; (*2*) high- and low-temperature buffer silicon layers; (*3*) first GeSi epilayer; (*4*) second GeSi epilayer.

In the second layer of sample D29, a significant relaxation was achieved even at a layer thickness of 100 nm. According to the X-ray diffraction data, the degree of relaxation was about 80%. We have also obtained heterostructures with the Ge fraction in the second layer increased by $\Delta x = 0.35$, 0.38, and 0.42 (samples D37, D45, and D46, respectively). After additional annealing at 500°C, the degree of relaxation in the second layer (relative to that in the first layer representing an artificial substrate) in these samples reached 97, 99, and 95%, respectively.

The results of observations in the atomic force microscope showed that the mean-square roughness of samples D37, D45, and D46 was 5.2, 3.1, and 3 nm, respectively. These values are on the record level reported for thick relaxed films (see, e.g., [2]).

In conclusion, we have demonstrated that, in Ge_xSi_{1-x}/Si(001) heterostructures grown with a two-step variation of the composition, the misfit stress relaxation in the second layer can be provided by dislocations penetrating from the first layer. Using this approach, we succeeded in growing ultimately thin

Epitaxial growth regimes and main parameters of the two-layer Ge_xSi_{1-x} films

Sample	Layer	Ge fraction, %	Layer thickness, nm	Growth temperature, °C	Annealing temperature, °C (1 h)	Total GeSi layer thickness, nm
D26	1	17	500	350	800	750
	2	38	200	350	–	
D29	1	20	500	350	800	650
	2	48	100	350	–	
D37	1	19	500	350	800	750
	2	54	200	350	500	
D45	1	16	500	350	700	650
	2	54	100	300	500	
D46	1	19	500	350	700	600
	2	61	100	300	500	

relaxed heterostructures with a germanium content on the surface within $x = 0.38–0.61$ and a total thickness of 600–750 nm.

Acknowledgments. This study was supported by the Russian Foundation for Basic Research (project no. 03-02-16085) and the Presidential Grant no. 00-15-96806.

REFERENCES

1. P. M. Mooney, J. L. Jordan-Sweet, J. O. Chu, *et al.*, Appl. Phys. Lett. **66**, 3642 (1995).
2. A. D. Capewell, T. J. Grasby, T. E. Whall, *et al.*, Appl. Phys. Lett. **81**, 4775 (2002).
3. S. B. Samavedam and E. A. Fitzgerald, J. Appl. Phys. **81**, 3108 (1997).
4. H.-J. Herzog, T. Hackbarth, G. Hock, *et al.*, Thin Solid Films **380**, 36 (2000).
5. Yu. B. Bolkhovityanov, O. P. Pchelyakov, L. V. Sokolov, and S. I. Chikichev, Fiz. Tekh. Poluprovodn. (St. Petersburg) **37**, 513 (2003) [Semiconductors **37**, 493 (2003)].
6. H. Chen, L. W. Guo, Q. Cui, *et al.*, J. Appl. Phys. **79**, 1167 (1996).
7. K. K. Linder, F. C. Zhang, J.-S. Rieh, *et al.*, Appl. Phys. Lett. **70**, 3224 (1997).
8. P. I. Gaiduk, A. N. Larsen, and J. L. Hansen, Thin Solid Films **367**, 120 (2000).
9. D. K. Bowen and B. K. Tanner, *High-Resolution X-ray Diffractometry and Topography* (Taylor & Fransis, Bristol, 1998; Nauka, St. Petersburg, 2002).

Translated by P. Pozdeev

Technical Physics Letters, Vol. 30, No. 1, 2004, pp. 71–73. Translated from Pis'ma v Zhurnal Tekhnicheskoĭ Fiziki, Vol. 30, No. 2, 2004, pp. 66–71.

Output Power Limitation in a Xe Laser Pumped by a Periodic-Pulsed Electric Beam

V. R. Gimatdinov, A. V. Karelin, D. L. Kuznetsov, Yu. N. Novoselov*, O. V. Simakova, and Yu. S. Surkov

Ural State Technical University, Yekaterinburg, Russia

Institute of Geomagnetism, Ionosphere, and Radio Wave Spreading, Russian Academy of Sciences, Troitsk, Russia

Institute of Electrophysics, Ural Division, Russian Academy of Sciences, Yekaterinburg, Russia

**e-mail: nov@iep.uran.ru*

Received July 22, 2003

Abstract—We report the experimental and theoretical characteristics of generation at 1.73 μm for a Xe laser pumped with an electron beam of a pulsed electron accelerator operating at a repetition rate of up to 100 Hz. A decrease in the average output power with time is caused by electron-beam heating of the active medium.

Xenon lasers are among the most promising near-infrared radiation sources for technological applications. The characteristics of Xe lasers pumped with electron beams or nuclear fission fragments have been extensively studied. It was established that most effective lasing is possible with an Ar–Xe mixture, in which more than 90% of the pumped energy is radiated at a wavelength of 1.73 μm. With electron beam pumping, the best output parameters obtained with this mixture at atmospheric pressure were as follows [1]: a maximum efficiency of 4.5% was achieved at a pulse duration of 4.5 μs and an electron beam current density of ~0.4 A/cm^2.

However, attempts to increase the pumping pulse duration to a few milliseconds led to a decrease in the laser output power and even to breakage of the lasing process before termination of the pumping pulse. The commonly accepted theoretical notions about processes taking place in the active medium of Ar–Xe lasers pumped with a hard ionizer, as well as the results of numerical calculations [2], suggest that the main reason for this behavior is heating of the active medium by the pumping pulses. It was of interest to study the role of this factor in a Xe laser pumped with a pulsed electron beam at a high repetition rate.

The experiments were performed using a pulsed electron accelerator as the pumping source. This accelerator, the scheme and design of which have been described elsewhere [3], is based on a pulsed voltage generator with inductive energy storage and a semiconductor current interrupter (SOS diodes analogous to those described in [4]). A pulsed electron beam generated by the accelerator was characterized by a pulse full width at half maximum of 35–40 ns, an electron energy of 235–230 keV, a current behind the foil of 330–300 A, and a cross section of 8×85 cm. The pulse repetition rate during long-term operation (for several hours) could be varied from a few pulses per second up to 100 Hz. In a short-time regime (for several seconds) the pulse repetition rate could be increased up to 1000 Hz.

The laser cell was a stainless steel half-cylinder with a radius of 8 cm. The water-cooled cell walls had a constant temperature of 20 ± 1°C. In the course of laser operation, the temperature of the working gas mixture was measured using a thermoresistor (MMT-1) and estimated from the electron beam-induced pressure jump measured by a differential manometer. Adjustable units mounted on the cell ends held mirrors in the form of plane-parallel quartz plates with multilayer dielectric coatings characterized by the reflection coefficients of 99.85 and 94.7% at 1.73 μm. A working volume from which the output radiation was taken had the shape of a cylinder with a diameter of 2 cm and a length of 85 cm.

The active medium was an Ar–Xe gas mixture with the component ratio of 200 : 1 at a total pressure of 1.5 bar. The mixture was prepared in a special mixing chamber and then admitted to the laser cell (preliminarily evacuated to 10^{-2} Torr. The specific pumping energy did not exceed 6×10^{-5} J/(cm^3 bar). The maximum power pumped into the laser cell volume at a pulse repetition rate of 100 Hz was 1.4 W/bar. The laser output power was measured with an IMO-2N radiant power meter.

Figure 1 shows the time variation of the average laser output power (solid curves) at a wavelength of 1.73 μm for various pumping pulse repetition frequencies *f*. In the case of pumping at a low repetition rate, the laser output power reaches a certain frequency-dependent level (curves *1* and *2*). The time of attaining this average level also depends on *f* and is determined

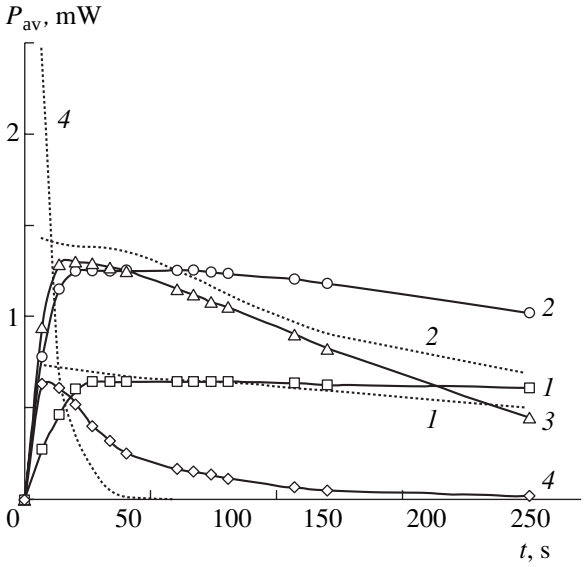

Fig. 1. Time variation of the average laser output power P_{av} for an Ar–Xe laser pumped with a pulsed electron beam at various pulse repetition frequencies f = 5 (*1*), 10 (*2*), 25 (*3*), and 100 Hz (*4*). Solid curves represent the experimental data, dashed curves show the results of model calculations.

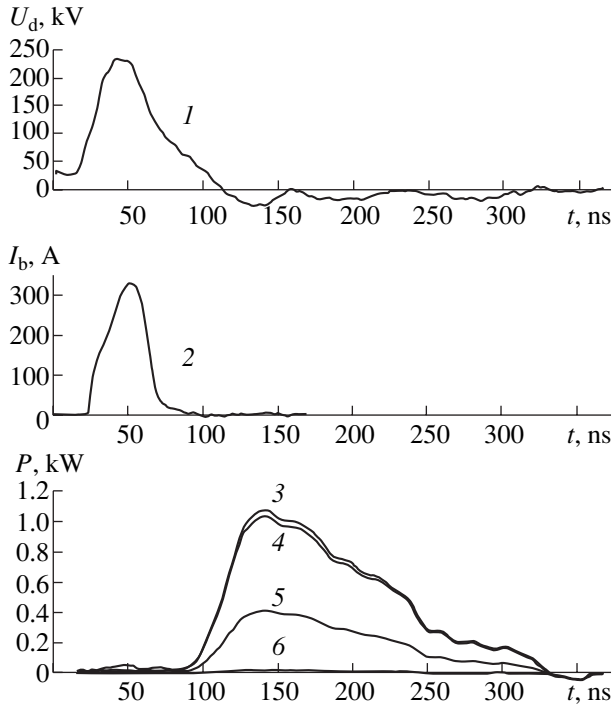

Fig. 2. The typical oscillograms of (*1*) the accelerating voltage pulses in the vacuum diode, (*2*) the electron beam current behind the accelerator output foil, and (*3*–*6*) the laser output power for various frequencies of pulsed pumping f = 0 (*3*), 10 (*4*), 25 (*5*), and 100 Hz (*6*).

by the thermal inertia of the sensitive element in the IMO-2N meter. At higher frequencies f, the average laser output power reaches a maximum level and then decreases (Fig. 1, curves *3* and *4*). For example, at f = 25 Hz, the average power (measured by the IMO-2N meter) reaches a maximum at t = 30 s and then decreases to reach zero at t = 800 s. At f = 100 Hz, the corresponding times are 10 and 300 s.

We believe that this limitation of the laser output power is related to heating of the active medium. Numerous experiments (see, e.g., [2] and references therein) showed that an increase in the temperature of the Ar–Xe gas mixture results in that the lasing characteristics begin to drop when the pumping level is far from reaching the maximum energy deposition of ~100 mJ/cm^3. In our opinion, heating of the active medium leads, first, to an increase in the efficiency of population of the lower laser level from the underlying state 6*s*' for the working electron transition $5d[3/2]_1^0 - 6p[5/2]_2$ in xenon and, second, to a decrease in the concentration of $ArXe^+$ and, hence, in the flux of dissociative recombination of $ArXe^+$ ions involved in pumping of the upper lasing level. This leads to violation of the state of population inversion and to breakage of the laser generation process. Our calculations [2] performed for the nuclear pumping of an Ar–Xe laser at a pulse duration of several milliseconds showed that it is a growth in the rate of population of the lower laser level from the underlying states 6*s* and 6*s*' and a decrease in the flux of dissociative recombination of ArX^+ that lead to the premature termination of lasing during the pumping pulse.

Analogous calculations have been performed for the active medium pumped with a nanosecond pulsed electron beam under the experimental conditions described above. The results of these calculations showed that the model of Xe laser active medium developed in [2] provides for an adequate description of the experimental data obtained in this study. Time variation of the average laser output power calculated using the model developed in [2] for various pumping frequencies is shown by dashed curves in Fig. 1. In these calculations, we ignored the transient characteristics of the power meter (IMO-2N) and the contribution to gas mixture cooling due to heat exchange at the cell walls (these restrictions may account for the discrepancies between calculated and experimental data in Fig. 1). The experiments showed that each frequency f corresponds to a certain gas mixture temperature established as a result of the electron beam induced gas heating and the heat exchange at the water-cooled cell walls. For f = 10, 25, and 100 Hz, this temperature is 11.5, 23.4, and 81.2°C.

Figure 2 shows the typical oscillograms of the accelerating voltage pulses in the vacuum diode, the electron beam current behind the accelerator output foil, and the laser output power for various frequencies of pulsed pumping. As can be seen from these data, the delay between the pumping pulses and the output radiation pulses is stable and independent of the pumping frequency. An increase in the pumping pulse repetition rate f (and, hence, in the gas mixture temperature) leads

to decrease in the laser pulse amplitude but not in the pulse shape. This fact indicates that a change in the pumping frequency and gas mixture temperature result only in decreasing concentration of inversely excited xenon atoms rather than in changing the kinetics of inverse level population for the working electron transition.

The results of this study show that stable generation is ensured in a Xe laser at a sufficiently low level of the working gas mixture heating. The experiments suggest that it is possible to create a high-frequency cw laser pumped with an electron beam, provided that effective cooling of the active medium will be ensured.

Acknowledgments. This study was supported within the framework of the Federal Program "Integration of Science and Higher Education in Russia," project no. ChO-015/2301.

REFERENCES

1. D. A. Zayarnyĭ, L. V. Semenova, N. N. Ustinovskiĭ, *et al.*, Kvantovaya Élektron. (Moscow) **25**, 493 (1998).
2. A. V. Karelin and O. V. Simakova, Kvantovaya Élektron. (Moscow) **28** (2), Part 1, 121 (1999); Part 2, 129 (1999).
3. F. Ya. Zagulov, V. V. Kladukhin, D. L. Kuznetsov, *et al.*, Prib. Tekh. Éksp., No. 5, 71 (2000).
4. S. A. Darznek, S. K. Lyubutin, S. N. Rukin, *et al.*, Elektronika, No. 4, 20 (1999).

Translated by P. Pozdeev

Technical Physics Letters, Vol. 30, No. 1, 2004, pp. 74–75. Translated from Pis'ma v Zhurnal Tekhnicheskoĭ Fiziki, Vol. 30, No. 2, 2004, pp. 72–75.

Refined Parameters of the Pair Potential of Interaction between Nitrogen and Water Molecules

O. A. Podmurnaya

East-Siberian Institute of Physicotechnical and Radioengineering Measurements, Irkutsk, Russia

e-mail: root@adm.niiftri.irkutsk.ru

Received April 28, 2003; in final form, July 14, 2003

Abstract—Taking into account new experimental data on the humidity of nitrogen, the second cross virial coefficient $B_{aw}(T)$ is quite satisfactorily described in a broad temperature range in terms of the "6–12" Lennard-Jones potential. © *2004 MAIK "Nauka/Interperiodica".*

Complex gas–water systems have to be described taking into account their nonideal character, which is more pronounced with increasing pressure and decreasing temperature. For small and moderate densities (at pressures below 10 MPa), the state of such mixtures is quite satisfactorily described in terms of a virial equation with the coefficients determined using the molar fractions of components, the virial coefficients of pure components, and the corresponding cross coefficients taking into account various interactions between molecules in the system studied.

The virial coefficients of pure gases are well known, while data on the cross coefficients are insufficient and refer to restricted temperature intervals, which hinders the use of the virial equation in practical calculations. Attempts to calculate the cross coefficients using various combination rules [1, 2] usually do not provide sufficient accuracy without corrections based on the experimental data. Therefore, obtaining reliable virial coefficients is an important task.

The above fully refers to the nitrogen–water system, which is among the most frequently studied objects in the hygrometry of wet gases. Many of the technological and metrological problems presently encountered in this field are related to the extremal pressures and temperatures. Under such conditions, it is necessary to evaluate and make allowance for the deviations of various properties of wet gas mixtures from those of the ideal gas.

In this context, the values of the second cross virial coefficient $B_{aw}(T)$ for wet nitrogen have been determined [3] using experimental data on the solubility (molar fraction) of water in nitrogen. Interpolation and extrapolation of the available experimental $B_{aw}(T)$ values beyond the range of parameters studied is hindered by the complicated temperature dependence of this coefficient.

One possible approach to solving this problem can be based on extrapolation using the well-known representation

$$B(T) = 2\pi\int_0^\infty r^2 dr\left(1 - \exp\left(-\frac{\varphi(r)}{kT}\right)\right), \qquad (1)$$

provided that the pair interaction potential $\varphi(r)$ is known. This study was aimed at determining the appropriate physical parameters of this interaction using experimental values of the second virial coefficient.

The problem was solved using the known method [1] of determination of the parameters of intermolecular interactions described in terms of the "6–12" Lennard-Jones potential:

$$\varphi(r) = 4\varepsilon[(\sigma/r)^{12} - (\sigma/r)^6], \qquad (2)$$

where ε is the minimum value of $\varphi(r)$ (i.e., the potential well depth) and σ is the radius at which the potential $\varphi(r)$ is zero.

Let $\bar{B}(T_l)$ be the experimental values of the second cross virial coefficient for wet nitrogen at temperature T_l. The corresponding values of ε/k were determined by numerically solving the equation

$$\frac{\bar{B}(T_l)}{\bar{B}(T_j)} = \frac{B^*(kT_l/\varepsilon)}{B^*(kT_j/\varepsilon)} \qquad (3)$$

for all possible combinations of the experimental data ($l, j = 1, \ldots, N$). Here, B^* is a reduced dimensionless coefficient introduced in representation (1) written as

$$B_{aw}(T) = \frac{2\pi}{3}N_A\sigma^3 B^*(kT/\varepsilon). \qquad (4)$$

1063-7850/04/3001-0074$26.00 © 2004 MAIK "Nauka/Interperiodica"

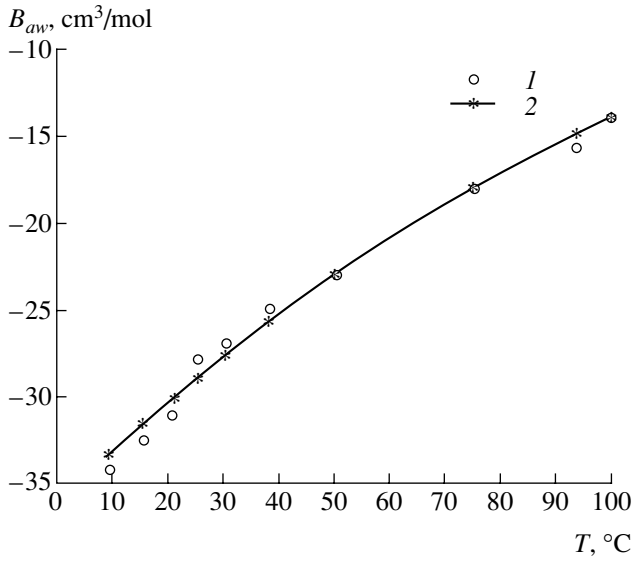

A comparison of the experimental data on $B_{aw}(T)$ and the values calculated in terms of the Lennard-Jones potential: (*1*) experiment; (*2*) theory.

Averaging over $N(N-1)/2$ values of ε/k obtained from Eq. (3) gives the final value of the potential well depth. Subsequent averaging over N values of (4) yields the corresponding value of σ.

The initial experimental data were the $B_{aw}(T)$ values obtained in [3, 4]. Equation (3) was solved for the following temperatures ($N = 10$): 9, 15, 20, 25, 30, 37.8, 50, 75, 93.3, and 100°C. The average value of ε/k is 145.29 K. The corresponding collision parameter found from Eq. (4) is $\sigma = 3.39$ Å.

In order to evaluate the reliability of the obtained parameters, the values of ε/k and σ were substituted into Eqs. (1) and (2) for the calculation of B_{aw} values. As can be seen from the comparison of experimental and calculated coefficients (see figure), the error does no exceed 1/3 of the experimental error.

Thus, the pair interaction of water and nitrogen molecules in this wet gas mixture, as characterized by the second virial coefficient, is well approximated by the "6–12" Lennard-Jones potential with the parameters ε/k and σ determined as described above. Using these parameters, it is possible not only to perform reliable interpolation but to extrapolate the B_{aw} values as well. This significantly decreases the amount of tedious experimental work for determining the temperature dependence of this virial coefficients.

In conclusion, it should be noted that the second virial coefficients are not only useful for the aforementioned practical purposes. These data are also necessary for the exact calculation of higher virial coefficients and the verification of model interaction potentials, especially in the range of even higher pressures.

REFERENCES

1. J. O. Hirschfelder, C. F. Curtiss, and R. B. Bird, *Molecular Theory of Gases and Liquids* (Wiley, New York, 1954; Inostrannaya Literatura, Moscow, 1961).
2. L. P. Filippov, N. L. Veretel'nikova, and A. D. Okhotsimskiĭ, Inzh.-Fiz. Zh. **48**, 971 (1985).
3. O. A. Podmurnaya *et al.*, in Technical Report No. 08.03.18.14 VS NIIFTRI (East-Siberian Research Inst. for Physicotechnical and Radioengineering Measurements, Irkutsk, 2001).
4. O. I. Gudkov, N. I. Dubovikov, O. A. Podmurnaya, *et al.*, Izmer. Tekh. **12**, 58 (2001).

Translated by P. Pozdeev

Technical Physics Letters, Vol. 30, No. 1, 2004, pp. 76–77. Translated from Pis'ma v Zhurnal Tekhnicheskoĭ Fiziki, Vol. 30, No. 2, 2004, pp. 76–80.

Heat Flux Measurements on the Inner Walls of a Shock Tube

S. Z. Sapozhnikov*, V. Yu. Mityakov, A. V. Mityakov, R. L. Petrov, V. V. Grigor'ev, S. V. Bobashev, N. P. Mende, and V. A. Sakharov**

St. Petersburg State Technical University, St. Petersburg, 195251 Russia
Ioffe Physicotechnical Institute, Russian Academy of Sciences, St. Petersburg, 194021 Russia
*e-mail: * serg.sapozhnikov@mail.ru; ** v.sakharov@mail.ioffe.ru*
Received July 24, 2003

Abstract—We have measured heat fluxes on the inner (cylindrical and edge) surfaces of a shock tube. The experiments were performed in gases (air, xenon) heated by a strong shock wave. For the first time, the heat flux in a shock wave was measured using sensors based on anisotropic single crystals of bismuth.

When a flying vehicle moves at a hypersonic velocity, a complicated system of shock waves arises at its surface that can lead to a considerable (tenfold and above) growth in the local heat flux density, rendering it capable of damaging the vehicle structure [1]. For this reason, designing hypersonic vehicles must include the stage of numerical modeling of streamlining with allowance for the real heat exchange. In order to set correct boundary conditions for such a modeling and to verify the numerical methods and computational schemes employed, it is necessary to estimate the level of heat fluxes and the dynamics of their variation in experiment.

A very attractive approach is to use heat flux sensors so as to perform direct measurements. Experiments in shock tubes [2, 3] require sensors possessing very fast response. Since the characteristic times of thermal processes in the systems of interest usually fall within 1–5 ms, the response time of a sensor must not exceed 0.05–0.1 ms. At the same time, the heat resistance of the sensor material is not as important as it might seem at first glance, since a gas jet with a temperature as high as $(7–8) \times 10^3$ K cannot change the temperature of streamlined surface by more than 100–200 K during such an experiment. Taking this into account, we employed gradient heat flux sensors (GHFSs) based on anisotropic single crystals of bismuth (0.9999 purity grade) [4, 5].

The GHFS operation principle relies on the transverse Seebeck effect, whereby the output thermo emf signal is proportional to the heat flux in the surface layer of bismuth. The electric field vector is perpendicular to the incident heat flux. The GHFS sensitivity typically falls within 10–20 mV/W, the response time does not exceed 0.05 ms, and the upper boundary of the working temperature range is close to the melting point of bismuth (544 K). We have used GHFSs developed at St. Petersburg State Technical University (STU) [4, 5], which have been successfully used previously, for example, in investigations of the nonstationary heat exchange in combustion chambers of Diesel engines (where the gas temperature exhibited cyclic variations with a maximum exceeding 2000 K) [6].

This letter presents the first results obtained using the aforementioned sensors for the measurement of heat fluxes in supersonic gas jets in shock tubes of the Ioffe Physicotechnical Institute (IPTI) [7] and STU [2]. The GHFSs used in these experiments had sensitive elements with an area of 4×7 mm and a thickness of 0.2 mm glued onto organic glass substrates. In the IPTI shock tube, the experiments were performed in xenon heated by a shock wave with the Mach number $M = 6$. The sensors, with their surface leveled with the inner wall of a cylindrical channel, were positioned in the tube cross section at a distance of 100 and 425 mm from the closed end and oriented with a smaller side of the sensitive element along the tube axis. Piezoelectric pressure sensors with a 4-mm sensitive element were positioned in the same cross sections. Thus, the heat flux and pressure in each experiment were first measured behind the incident shock wave and then behind the wave reflected from the closed end of the shock tube.

Figure 1 shows the results of measurements in the tube cross section 100 mm from the closed end. As can be seen, the response of the pressure sensor (dashed curve) exhibits sharp jumps when the incident ($t = 0.15$ ms) and reflected ($t = 0.55$ ms) shock waves pass through this cross section. The heat flux profile (solid curve) is fully correlated with the pressure variations. The heat flux density in the region behind the reflected shock wave (for a gas temperature of $T \sim 7000$ K) reaches 1.4 MW/m^2. Both sensors were preliminarily calibrated so that errors of the heat flux and pressure measurements did not exceed ~2% and 10%, respectively.

1063-7850/04/3001-0076$26.00 © 2004 MAIK "Nauka/Interperiodica"

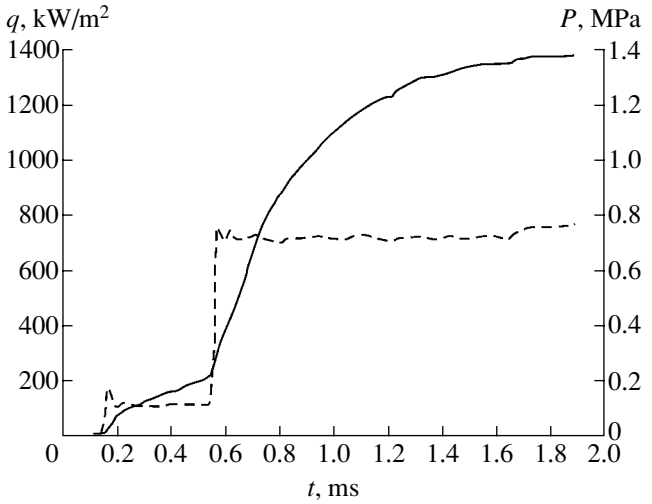

Fig. 1. Time variation of the heat flux (solid curve) and pressure (dashed curve) on the inner wall surface of a cylindrical shock tube filled with xenon. Both sensors are in the cross section at a distance of 100 mm from the closed end.

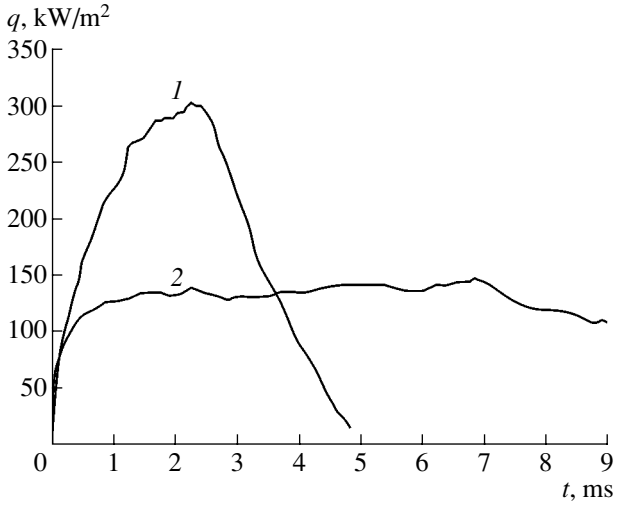

Fig. 2. Time variation of the heat flux (*1*) on the inner side wall (3 m from the closed end) and (*2*) on the inner edge surface of a cylindrical sock wave tube filled with air.

In the STU shock tube, the experiments were performed in air according to the same general scheme. Here, the shock wave velocity corresponded to $M = 1.9$. One GHFS was placed on the inner cylindrical wall in the cross section at a distance of 3 m from the closed end, while the other was mounted at the center of the closed end.

The results of heat flux measurements in the STU setup are presented in Fig. 2. Here, the front of each response pulse also corresponds to the arrival of a shock wave to the corresponding sensor. The response of the side-wall sensor (curve *1*) reflects the initial increase in the heat flux accompanying the passage of the incident shock wave (the temperature behind the wave is $T \sim 460$ K) and then decreases (for $t > 2.5$ ms) when a cold gas arrives in this cross section. The end sensor (curve *2*) immediately after arrival (and reflection) of the shock wave occurs in the region of quiescent gas possessing a higher temperature ($T \sim 900$ K). The heat flux attains a constant level at $t \sim 1.5$ ms after the wave reflection and then remains constant until $t \sim 7$ ms, when the cold gas reaches the tube end. Note that the maximum heat flux level on the cylindrical wall (Fig. 2, curve *1*) is almost two times higher than that on the edge surface (curve *2*). This fact is apparently indicative of the different mechanisms of heat exchange operative on the side and end inner surfaces of the tube. At the edge, the heat exchange proceeds as between two semi-infinite rods [8], while the process on a cylindrical wall predominantly follows the convective exchange mechanism.

The latter conclusion is consistent with the results of heat flux measurements behind the reflected shock wave in the IPTI setup (Fig. 1). This sensor occurred in a boundary layer formed by a cocurrent flow behind the incident wave. The reflected shock wave moved in the opposite direction and interacted with the boundary layer. As a result, the gas near the tube wall was not at rest (as was the gas at the tube end) and the convective heat exchange was possible.

The results of our investigation show that GHFSs based on anisotropic single crystals of bismuth can be used for the measurement of large thermal loads in supersonic gasdynamics. It should be noted that the obtained data qualitatively agree with the results of analogous measurements [9] performed using film sensors.

REFERENCES

1. B. E. Edney, AIAA J. **6**, 16 (1968).
2. M. G. Babinskiĭ, V. V. Grigor'ev, S. N. Isakov, *et al.*, Tr. Leningr. Politekh. Inst., No. 352, 100 (1976).
3. N. I. Akatnov, M. G. Babinskiĭ, and R. V. Vasil'eva, Zh. Tekh. Fiz. **52**, 884 (1982) [Sov. Phys. Tech. Phys. **27**, 566 (1982)].
4. V. Y. Mitiakov, S. Z. Sapozhnikov, Y. S. Chumakov, *et al.*, in *Proceedings of the 5th World Conference on Experimental Heat Transfer, Fluid Mechanics and Thermodynamics, Thessaloniki, 2001*, pp. 111–116.
5. S. Z. Sapozhnikov, V. Y. Mitiakov, and A. V. Mitiakov, in *Proceedings of the 3rd European Conference on Thermal Science, Heidelberg, 2000*, pp. 687–690.
6. S. Z. Sapozhnikov, V. Yu. Mityakov, and A. V. Mityakov, Izv. Vyssh. Uchebn. Zaved. Énerg. Ob"ed. SNG, Ser. Énergetika, Nos. 9–10, 53 (1997).
7. V. G. Maslennikov and V. A. Sakharov, Zh. Tekh. Fiz. **67** (11), 88 (1997) [Tech. Phys. **42**, 1322 (1997)].
8. H. S. Carslaw and J. C. Jaeger, *Conduction of Heat in Solids* (Clarendon Press, Oxford, 1959; Nauka, Moscow, 1964).
9. Yu. V. Zhilin, Preprint No. 2-005, IVTAN (Institute of High Temperatures, Academy of Sciences of USSR, 1976).

Translated by P. Pozdeev

Technical Physics Letters, Vol. 30, No. 1, 2004, pp. 78–81. Translated from Pis'ma v Zhurnal Tekhnicheskoĭ Fiziki, Vol. 30, No. 2, 2004, pp. 81–88.

Equations of a Time-Delay System under External Action Reconstructed from Time Series

M. D. Prokhorov, V. I. Ponomarenko, and A. S. Karavaev

Saratov Branch, Institute of Radio Engineering and Electronics, Russian Academy of Sciences, Saratov, Russia

e-mail: sbire@sgu.ru

Received July 2, 2003

Abstract—A new method is proposed for the use of time series for reconstructing the equations of a system with time-delay feedback under an external action. The performance of the proposed method is illustrated by application to short noisy time series of a model system under external actions of various types. © *2004 MAIK "Nauka/Interperiodica".*

Introduction. In recent years, the problem of reconstruction of the equations of nonlinear dynamical systems with time-delay feedback (time-delay systems) has received much attention [1–9]. The importance of this problem is related to the fact that time-delay systems are frequently encountered in nature. The behavior of such systems is not entirely determined by the present state, but depends on the preceding states as well. Accordingly, time-delay systems are usually described in terms of differential equations with a delayed argument. Such models are successfully used in various fields of physics, biology, physiology, and chemistry. However, reconstruction of the model equations of a time-delay system from its time series in the case when this system occurs under the action of other systems is still insufficiently studied, although this situation is encountered in solving many important practical problems.

In this paper, methods developed previously [6–8] for the reconstruction of the model equations of time-delay systems from their chaotic time series are extended so as to include such systems occurring under an external action.

Description of the method. Consider a time-delay system X described in the absence of external actions by a first-order differential equation with delayed argument of the following general type:

$$\varepsilon_0 \dot{x}(t) = -x(t) + f(x(t-\tau_0)), \quad (1)$$

where x is a dynamical variable describing the state of the system at the time t, f is a nonlinear function, τ_0 is the delay time, and ε_0 is a parameter characterizing the inertia of the system. In the general case, Eq. (1) represents the mathematical model of an oscillatory system comprising a circuit with three ideal elements: nonlinear device, inertial element, and delay line. In Fig. 1, these elements of a circuit X are denoted by f, ε_0, and τ_0, respectively.

Now, let another system Y to act upon system X. This action can be realized in different ways. We distinguish between three methods of coupling, by which a variable of system Y is introduced with a certain coefficient into various points of circuit X (denoted by Roman numerals I–III in Fig. 1). Depending on the point of application of the system Y action upon system X, the dynamics of the latter system is described by one of the following equations:

$$\text{I: } \varepsilon_0 \dot{x}(t) = -x(t) + f(x(t-\tau_0) + k_y y(t-\tau_0)), \quad (2)$$

$$\text{II: } \varepsilon_0 \dot{x}(t) = -x(t) + f(x(t-\tau_0) + k_y y(t)), \quad (3)$$

$$\text{III: } \varepsilon_0 \dot{x}(t) = -x(t) + f(x(t-\tau_0)) + k_y y(t), \quad (4)$$

where $y(t)$ is a dynamical variable describing the state of system Y at the time t and k_y is the coupling coefficient characterizing the degree of the system Y action upon X.

The proposed method allows the time-delay system X to be reconstructed, the coupling mode to be determined (i.e., the situations described by Eqs. (2)–(4) to

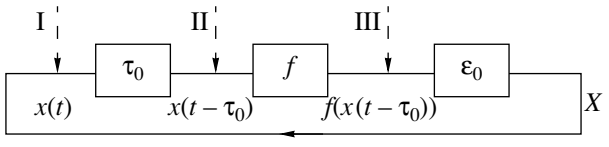

Fig. 1. Schematic diagram of a time-delay system X. Elements denoted by τ_0, f, and ε_0 represent the delay line, nonlinear device, and inertial transformation of oscillations in the system, respectively. Points I–III represent various modes of introduction of the external action (system Y) into system X.

1063-7850/04/3001-0078$26.00 © 2004 MAIK "Nauka/Interperiodica"

be distinguished), and the degree of external action (i.e., the value of k_y) to be estimated from the available time series of oscillations in systems *Y* and *X*. In order to determine the delay time τ_0 from the observed time series $x(t)$, we use the method developed in [6], where it was demonstrated that time series of the systems of type (1) contain virtually no extrema spaced from each other by τ_0. In order to find τ_0, we have to indicate extrema in the initial time series, determine the number *N* of the pairs of extrema spaced by various times τ, and construct the $N(\tau)$ dependence. Then, the delay time τ_0 is determined by the position of the absolute minimum of the $N(\tau)$ function. The results of our investigations showed that this approach can also be successfully used in cases when system *X* occurs under the action of another system *Y*, provided that this external action does not lead to the appearance of a large number of additional extrema in the time realizations of oscillations in system *X*.

For determining the parameter ε_0 and the function *f* of system *X* and the coupling coefficient k_y, we propose a method based on an analysis of the time series of both observables $x(t)$ and $y(t)$. First, let us assume that the mode of action of system *Y* upon system *X* (i.e., the structure of equation describing dynamics of the time-delay system under the external action) is known. For example, consider the coupling mode I described by Eq. (2), whereby the variable of system *Y* is introduced into the feedback circuit of *X* after the inertial element. As can be seen from Eq. (2), a set of points with the coordinates $(x(t-\tau_0) + k_y y(t-\tau_0), \varepsilon_0 \dot{x}(t) + x(t))$ plotted on the plane will reproduce the function *f*. Since the quantities ε_0 and k_y are not known a priori, we have to plot $\varepsilon\dot{x}(t) + x(t)$ versus $x(t-\tau_0) + ky(t-\tau_0)$ for various ε and *k* in search for the single-valued relationship that is possible only for $\varepsilon = \varepsilon_0$ and $k = k_y$. As a quantitative criterion of such a unique relationship in the search for ε_0 and k_y, we can use the minimum length of a segment $L(\varepsilon, k)$ connecting points (ordered with respect to abscissa) on the above plane. A minimum of $L(\varepsilon, k)$ will correspond to $\varepsilon = \varepsilon_0$ and $k = k_y$, while the dependence of $\varepsilon\dot{x}(t) + x(t)$ on $x(t-\tau_0) + ky(t-\tau_0)$ constructed for these parameters will reproduce a nonlinear function that can be approximated. The proposed approach employs all points of the time series, which allows short time series to be used for reconstruction of the system parameters ε_0 and k_y and the nonlinear function *f*.

The same method can be used for reconstructing the nonlinear function *f* and the parameters ε_0 and k_y in the situations described by Eqs. (3) and (4) by plotting $\varepsilon\dot{x}(t) + x(t)$ versus $x(t-\tau_0) + ky(t)$ and $\varepsilon\dot{x}(t) + x(t) - ky(t)$ versus $x(t-\tau_0)$, respectively, for various ε and *k*. If the point (I, II, or III) at which system *Y* acts upon system *X* is not known a priori, it is necessary to perform reconstruction for each of the three model equations (2)–(4). The only correct structure of the model equation will be indicated by single-valued form of the reconstructed function and, accordingly, by the lowest of the three values of $L_{\min}(\varepsilon, k)$. Thus, the proposed method allows both the parameters of a time-delay system under external action and the mode of this action (i.e., the form of the model equation) to be reconstructed from the observed time series.

Verification of the method. We will demonstrate the performance of the proposed reconstruction method by applying the procedure outlined above to a time-delay system *X* described by the Mackey–Glass equation,

$$\dot{x}(t) = -bx(t) + \frac{ax(t-\tau_0)}{1 + x^c(t-\tau_0)}, \qquad (5)$$

under an external system *Y* producing a harmonic or chaotic action. Equation (5) reduces to the form of Eq. (1) with $\varepsilon_0 = 1/b$ and $f(x(t-\tau_0)) = ax(t-\tau_0)/b(1 + x^c(t-\tau_0))$.

Figure 2 shows the results of reconstruction of the Mackey–Glass system in a chaotic regime ($a = 0.2$, $b = 0.1$, $c = 10$, $\tau_0 = 300$) under the action of system *Y* performing sinusoidal oscillations $y(t) = A\sin\omega t$ with an amplitude ($A = 1$) close to the amplitude of natural oscillations in system (5) and with the oscillation period $T = 2\pi/\omega = 130$. The type of *Y*–*X* coupling corresponds to mode I described by Eq. (2) with a coupling coefficient $k_y = 0.1$. The plot of $N(\tau)$ (Fig. 2a) was constructed using a time series $x(t)$ containing 5000 points. The derivative $\dot{x}(t)$ was estimated from the time series by means of a local parabolic approximation. The absolute minimum of $N(\tau)$ allows the delay time to be exactly estimated as $\tau_0 = 300$.

Figures 2b–2d illustrate reconstruction of the nonlinear function for the ε and *k* values corresponding to a minimum of $L(\varepsilon, k)$ for the model equation selected in the form (2), (3), or (4), respectively. These plots were constructed using only 1000 points for each of the $x(t)$ and $y(t)$ time series. In the search for $L_{\min}(\varepsilon, k)$, the parameter ε was varied at a step of 0.1 ($\varepsilon_0 = 1/b = 10$), and the parameter *k*, at a step of 0.01. For the model reconstructed in the form of Eq. (2), a minimum length of the $L(\varepsilon, k)$ segment normalized to the number of points was $L_{\min}(\varepsilon, k) = L(10.1, 0.10) = 0.007$. When the model was selected in the form of Eq. (3), we obtained $L_{\min}(\varepsilon, k) = L(7.4, -0.05) = 0.153$, while reconstruction in the form of Eq. (4) yielded $L_{\min}(\varepsilon, k) = L(7.3, 0.06) = 0.147$. Of the three plots, only Fig. 2b shows a nearly single-valued relationship and the corresponding $L_{\min}(\varepsilon, k)$ value is significantly smaller than the two other. These results indicate that the model equation is correctly identified in the form (2) and shows that the parameters ε_0 and k_y are determined with a good accuracy.

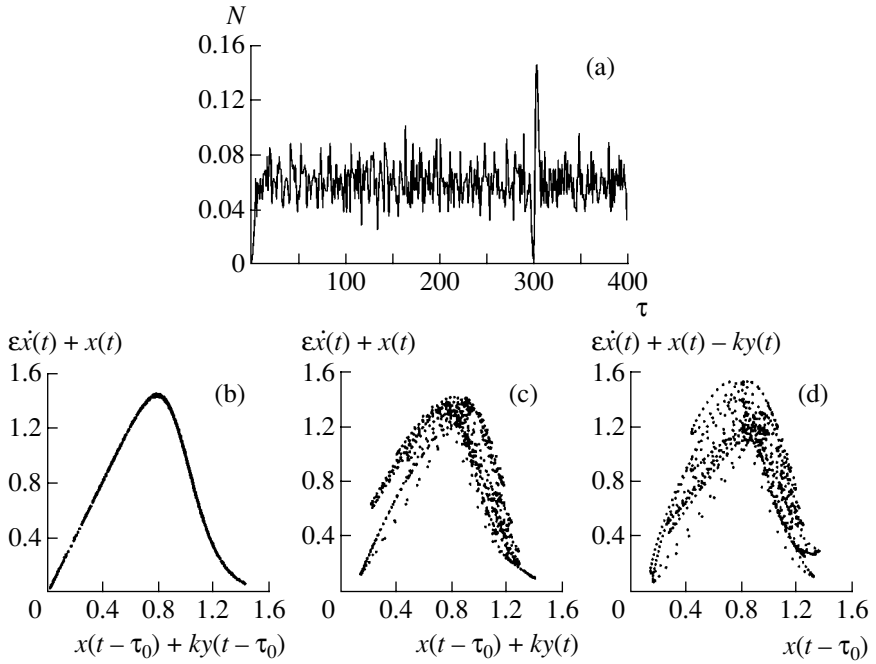

Fig. 2. Reconstruction of the Mackey–Glass system under external harmonic action: (a) plot of the number N of the pairs of extrema in a time series of X spaced by various times τ, normalized to the total number of such extrema ($N_{min}(\tau) = N(300)$; (b–d) reconstruction of the nonlinear function for a model equation selected in the form of Eqs. (2)–(4), respectively, with the parameters (b) $\varepsilon = 10.1$, $k = 0.10$; (c) $\varepsilon = 7.4$, $k = -0.05$; (d) $\varepsilon = 7.3$, $k = -0.06$.

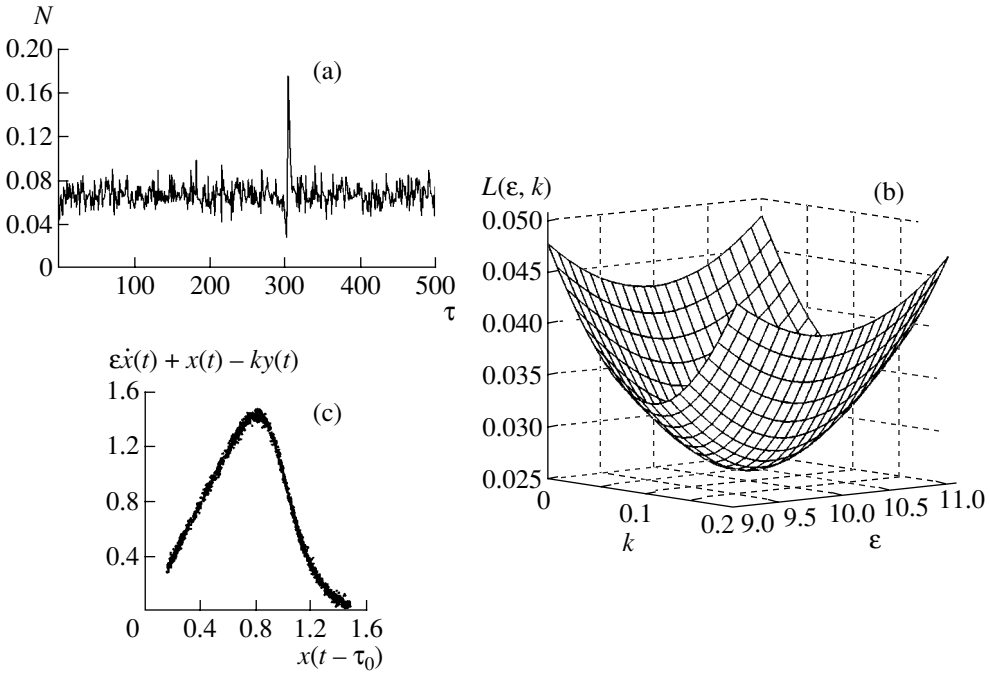

Fig. 3. Reconstruction of the Mackey–Glass system under the action of another Mackey–Glass system in the presence of noise: (a) plot of the number N of the pairs of extrema in a time series of X spaced by various times τ, normalized to the total number of such extrema ($N_{min}(\tau) = N(300)$; (b) $L(\varepsilon, k)$ function for the model equation selected in the form of Eq. (4) normalized to the number of points ($L_{min}(\varepsilon, k) = L(10.0, 0.10) = 0.026$); (c) reconstruction of the nonlinear function for $\varepsilon = 10$, $k = 0.1$.

For the parameters of systems X and Y indicated above, the proposed method allows the type of the model equation to be determined and system X to be reconstructed for $0.01 \le |k_y| \le 0.5$. In comparison to the other methods [10, 11] of determining the coupling between systems from their time series, our procedure has a number of advantages. In contrast to the method of directivity indices [11], the proposed procedure is

applicable to synchronized systems and allows the magnitude of coupling (rather than only its direction) to be estimated even in the case of fundamentally different systems.

In order to check the performance of the proposed method in the presence of perturbations, we applied it to a system with noise. The procedure has proved to be more sensitive to noise in the time-delay system, but it still works when the noise level in system X is on the order of 10%. The level of noise in system Y can be several times greater than that in system X.

Finally, we have considered the case when the external action upon system X is produced by another time-delay system Y. Figure 3 shows the results of reconstruction for a Mackey–Glass type system with $a = 0.2$, $b = 0.1$, $c = 10$, and $\tau_0 = 300$ in the presence of another Mackey–Glass type system with the same values of a, b, and c at $\tau_0 = 400$. The coupling between Y and X corresponded to mode III described by Eq. (4) with $k_y = 0.1$. In addition, both systems were perturbed by a Gaussian white noise with zero mean and an rms deviation amounting to 10% of that for the time series without noise. Despite the presence of noise, the plot of $N(\tau)$ allows the delay time to be precisely estimated (Fig. 3a) and the $L(\varepsilon, k)$ map restores the values of ε_0 and k_y (Fig. 3b). The $L(\varepsilon, k)$ plot was constructed using 2000 points of $x(t)$ and $y(t)$ time series at a step of 0.1 for ε and 0.01 for k. The presence of noise significantly impairs the quality of reconstruction of the nonlinear function (Fig. 3c). For the model reconstructed in the form of Eq. (2), we obtain $L_{\min}(\varepsilon, k) = L(10.1, 0.01) = 0.042$, while reconstruction in the form of Eq. (3) gives $L_{\min}(\varepsilon, k) = L(10.0, -0.02) = 0.039$. This analysis indicates that the model equation should be identified in the form (4), which yields the minimum value of $L_{\min}(\varepsilon, k) = L(10.0, 0.10) = 0.026$.

Conclusion. We proposed a new method for reconstructing a time delay system under an external action from the observable time series. The method was verified for various types of external action and different ways of its introduction into the given system. The proposed method can be successfully applied to the analysis of short time series even at a rather high noise level.

Acknowledgments. The authors are grateful to B.P. Bezruchko for fruitful discussions.

This study was supported by the Russian Foundation for Basic Research (project no. 03-02-17593), the US Civilian Research and Development Foundation for Independent States of the Former Soviet Union (Award no. REC-006), and the "Dynasty" Foundation of Noncommercial Programs (grant no. 245 662).

REFERENCES

1. M. J. Bünner, M. Popp, Th. Meyer, *et al.*, Phys. Rev. E: Stat. Phys., Plasmas, Fluids, Relat. Interdiscip. Top. **54**, 3082 (1996).
2. H. Voss and J. Kurths, Phys. Lett. A **234**, 336 (1997).
3. S. P. Ellner, B. E. Kendall, S. N. Wood, *et al.*, Physica D **110**, 182 (1997).
4. R. Hegger, M. J. Bünner, and H. Kantz, Phys. Rev. Lett. **81**, 558 (1998).
5. M. J. Bünner, M. Ciofini, A. Giaquinta, *et al.*, Eur. Phys. J. D **10**, 165 (2000).
6. A. S. Karavaev, V. I. Ponomarenko, and M. D. Prokhorov, Pis'ma Zh. Tekh. Fiz. **27** (10), 43 (2001) [Tech. Phys. Lett. **27**, 414 (2001)].
7. B. P. Bezruchko, A. S. Karavaev, V. I. Ponomarenko, and M. D. Prokhorov, Phys. Rev. E: Stat. Phys., Plasmas, Fluids, Relat. Interdiscip. Top. **64**, 056216 (2001).
8. V. I. Ponomarenko and M. D. Prokhorov, Pis'ma Zh. Tekh. Fiz. **28** (16), 37 (2002) [Tech. Phys. Lett. **28**, 680 (2002)].
9. V. S. Udaltsov, J.-P. Goedgebuer, L. Larger, *et al.*, Phys. Lett. A **308**, 54 (2003).
10. M. G. Rosenblum and A. S. Pikovsky, Phys. Rev. E: Stat. Phys., Plasmas, Fluids, Relat. Interdiscip. Top. **64**, 045202 (2001).
11. M. G. Rosenblum, L. Cimponeriu, A. Bezerianos, *et al.*, Phys. Rev. E: Stat. Phys., Plasmas, Fluids, Relat. Interdiscip. Top. **65**, 041909 (2002).

Translated by P. Pozdeev

Technical Physics Letters, Vol. 30, No. 1, 2004, pp. 82–84. Translated from Pis'ma v Zhurnal Tekhnicheskoĭ Fiziki, Vol. 30, No. 2, 2004, pp. 89–94.

The Nature of Optical Pumping Losses in Low-Threshold LiF(F_2, F_3^+) Crystal Microlasers

L. I. Shchepina*, S. S. Kolesnikov, and E. V. Romanovskaya

Institute of Applied Physics, Irkutsk State University, Irkutsk, Russia

** e-mail: schepina@api.isu.runnet.ru*

Received June 30, 2003

Abstract—The character of optical losses in Li(F_2, F_3^+) crystals were studied for the first time by methods of optical absorption spectroscopy and X-ray diffraction. It is suggested that centers absorbing at 420 nm represent quasi-metallic defects of the F_2F_L type. © *2004 MAIK "Nauka/Interperiodica".*

In recent years, LiF-based films colored by low-energy electron bombardment have found new applications [1] as active materials in vertical cavity devices (directed LEDs and low-threshold microlasers). These laser structures are pumped with argon lasers at λ = 458 nm and, hence, it is important to know the nature of defects absorbing in this spectral region. After the external optical action (optical bleaching by exposure to the integral radiation of a xenon lamp), the room-temperature absorption spectra of γ-irradiated LiF–Me, O, OH crystals reveal the maximum density of defects absorbing at λ_m = 420 nm. This study was aimed at elucidating the nature and the mechanism of formation of these defects (referred to below as 420-nm centers).

The optical absorption in the region of 415 nm in neutron-irradiated LiF crystals at low temperatures was originally observed by Kamikawa *et al.* [2] and assigned to the F_2 centers modified by crystal lattice defects. The same interpretation was used by Zhuravlev *et al.* [3]: the absorption band at λ_m = 420 nm observed in the spectra of LiF–OH crystals upon electron irradiation and annealing at T = 573 K was assigned to oxygen-modified F_2 centers. However, the defects under consideration are not emitting and, hence, cannot belong to the F_2-type centers. The colloidal nature of 420-nm centers is also excluded [4], because the spectral intensity distribution in this absorption band exhibits a change at T = 78 K.

We used optical absorption spectroscopy and X-ray diffraction to determine the optimum conditions for the formation of 420-nm centers in LiF. We have studied the photo- and thermoinduced transformations of the radiation defects, evaluated the electron density $\rho(x, o, o)$ in the lattice sites, and determined the X-ray diffraction reflection broadening. The experiments were performed with LiF crystals grown by the Kyropoulos technique and γ-irradiated to a dose of $D = 6 \times 10^7$–4×10^8 R. In order to induce the 420-nm centers, the crystals were exposed to the integral radiation of xenon lamps in the quantron of a 1-MW Kvant-17 laser. Selective optical bleaching was provided by exposure to the fourth harmonic of a YAG-Nd laser (λ = 266 nm; ν = 12.5 Hz; τ = 10 ns, $n = 10^4$ pulses; P = 0.03 W) at 78 K. The X-ray powder diffraction was studied in a DRON-3M diffractometer using Cu$K_{\alpha 1, 2}$ radiation.

Results and discussion. Figure 1 shows the optical absorption spectrum measured at 78 K, which displays the absorption peaks at 413.0 and 420.12 nm (curve *2*). The position of a zero phonon line (ZPL) for the absorption band at λ_m = 420 nm was determined by the formula $\nu_{00} = \nu_m^{abs} - (\Delta\nu_{abs})^2/16\ln 2kT$, where $\Delta\nu_{abs}$ is the full width at half-maximum of the absorption band and ν_m^{abs} is the absorption peak position. The ZPL position (420.12 nm) calculated using this formula coincides with the experimental value. The peak at 413.0 and the ZPL at 420.12 nm exhibit analogous behavior in the course of isochronous annealing (T = 573 K), which suggested that both signals belong to the same defect.

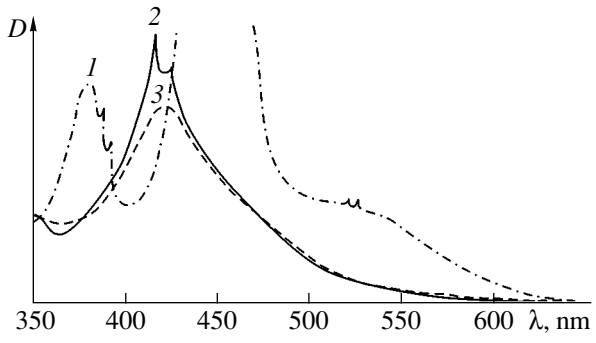

Fig. 1. The optical absorption spectra of a LiF–Me, O, OH crystal (*1*) after γ-irradiation to $D = 2 \times 10^8$ R and (*2*, *3*) after the subsequent optical discoloration by the integral light of a xenon lamp (n = 3000 pulses); measured at T = 78 K (*2*) and 300 K (*3*).

1063-7850/04/3001-0082$26.00 © 2004 MAIK "Nauka/Interperiodica"

No redistribution of the intensity of these peaks was observed during various transformations of the defect centers.

The efficiency of formation of the defects under consideration was evaluated by studying the crystals γ-irradiated to various doses. The linear accumulation of 420-nm centers with the γ-irradiation dose D increasing in the range from 6×10^7 to 4×10^8 R is evidence of the intrinsic nature of these defects in the crystal lattice, since the impurity defects exhibit saturation in the first stage of irradiation at a dose of 10^7 R. This conclusion is also confirmed by the fact that the 420-nm band is present irrespective of the impurity composition: the ZPL at 420.12 nm was also observed in a vacuum-melted sample irradiated to $D = 4.2 \times 10^8$ R.

The curves of isochronous annealing showed that the optimum temperature for the formation of defects under consideration is ~573 K and confirmed that the 420-nm centers are induced in the course of annealing of γ-irradiated crystals. It should be noted that the efficiency of formation of these centers is higher in optically bleached samples.

The charge state of the 420-nm centers was determined using optical bleaching in the F band at $T = 78$ K under the action of the fourth harmonic of a YAG-Nd laser. A sample with induced 420-nm centers was prepared by γ irradiation to $D \sim 1 \times 10^8$ R followed by the optical discoloration under the action of $n = 5700$ pulses of the integral radiation of a xenon lamp. In the sample with a thickness of ~1 mm, the F-center concentration prior to the optical discoloration amounted to 1.6×10^{17} cm^{-3}. After the exposure to 2.3×10^4 nanosecond light pulses, the concentration of broken F centers reached $\sim 1.72 \times 10^{16}$ cm^{-3}. At the same time, no changes were observed in the region of optical absorption studied. These results indicate that the 420-nm centers possess a neutral charge and do not interact with electrons of the F centers. This explains the high optical stability of the defects under consideration, which are not broken by the light with a wavelength of 420 nm.

A phototransformation of the radiation defects was observed in the stage of induction of the 420-nm centers under the action of the integral radiation of a xenon lamp. It was found that defects with the ZPL at 520.0 nm and $\lambda_m = 508$ nm are converted into the centers with the ZPL at 413.0 nm (Fig. 2). Taking into account the analogous behavior of the absorption band with $\lambda_m = 508$ nm and the ZPL at 520.0 nm under the external optical action, it was suggested that the ZPL at 520.0 nm belongs to the centers absorbing at $\lambda_m = 508$ nm. As is known, these centers are formed as a result of breakage of the F_3^+ color centers.

Recently [5], we demonstrated that the action of light and temperature leads to displacement of the electron density from F_3^+ color centers in the excited state toward the nearest lithium cation. As a result, there appears an F center containing lithium atom (F_L):

$$F_3^+ + Li^+ + h\nu \longrightarrow (F_3^+)^* + Li^+$$

$$\longrightarrow F V_a^+ V_a^+ + Li^0 \longrightarrow F_L V_a^+ V_a^+ + V_c^-.$$

The cation vacancy becomes free at a temperature of 573 K. This process is observed in the first stage of opti-

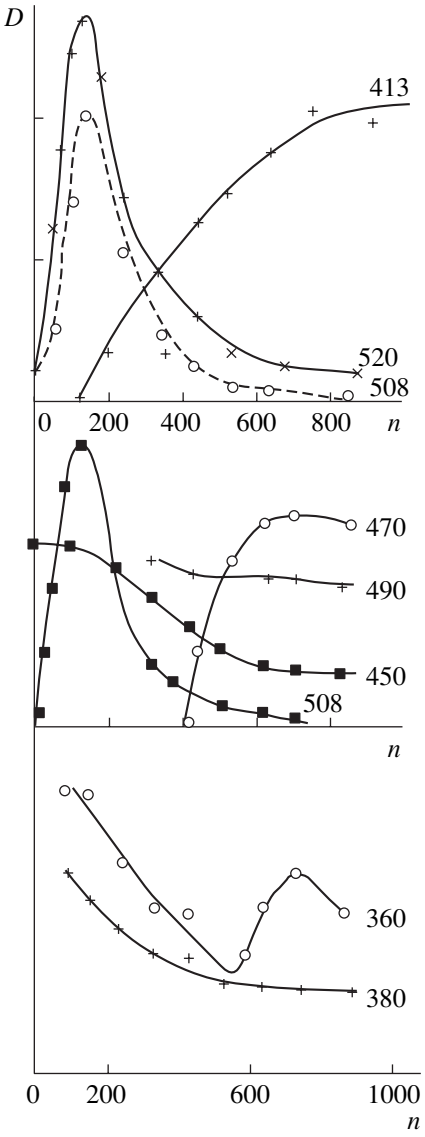

Fig. 2. Variation of the intensity of absorption peaks in the spectrum of a LiF–Me, O, OH crystal (γ-irradiated to $D = 8 \times 10^7$ R) in the course of the optical discoloration by the integral light of a xenon lamp (n is the number of light pulses): 413.0 nm (ZPL of the defects under consideration); 520.0 (ZPL of the 508-nm centers); 508 nm ($F_L V_a^+ V_a^+ + V_c^-$); 470 and 490 nm (probably Li colloids); 450 nm (F_2, F_3^+); 360 nm (V_k and Li colloids); 380 nm (F_3 and $F_L F$ centers).

cal bleaching: beginning with $n = 150$ pulses ($D = 8 \times 10^7$ R), the centers absorbing at 508 nm are converted into 420-nm centers. A high-temperature peak of thermostimulated luminescence in LiF was observed at ~573 K in [6]. Taking into account the effective formation of defects under consideration and the release of electrons from traps at this temperature, we may suggest that the localization of electrons on the anion vacancies of the centers absorbing at 508 nm leads to the formation of a new defect: $F_L F_2$. The appearance of a lithium atom in the *F* center will produce local stresses in the crystal lattice. This, in turn, must decrease the lattice parameter and cause broadening of the diffraction reflections, in agreement with what is observed in experiment.

It should be noted that an increase in the level of internal stresses might also be caused by an increase in the temperature. In this case, the electron density at the lattice sites must decrease: the greater the mean-square displacement of atoms from the equilibrium position, the weaker the interference peaks and the lower the $\rho(x, o, o)$ values obtained from the Fourier synthesis. However, an analysis of the electron density showed that this value increases at the lattice sites of both lithium and fluorine. Therefore, the increase in the internal stresses in the crystal lattice is due to the formation of a new defect.

Acknowledgments. This study was supported within the framework of the Federal Program "Universities of Russia," project no. UR.01.01.075.

REFERENCES

1. F. Somma, A. Belarouch, M. Cathelinaud, *et al.*, Radiat. Eff. Defects Solids **156** (1–4), 151 (2001).
2. T. Kamikawa, Y. Kazumota, and K. Ozawa, Phys. Status Solidi B **114**, 435 (1966).
3. K. S. Zhuravlev, S. S. Kolyago, A. I. Li, *et al.*, *Luminescence and Related Phenomena* (Irkutsk. Gos. Univ., Irkutsk, 2001), p. 109.
4. M. Montecchi, E. Nichelatti, and A. Mancini, J. Appl. Phys. **86**, 3745 (1999).
5. L. I. Shchepina, S. S. Kolesnikov, V. M. Kalikhman, and I. V. Teryaeva, Opt. Spektrosk. **90**, 622 (2001) [Opt. Spectrosc. **90**, 552 (2001)].
6. N. Yazycy and Z. Ozturk, J. Phys. D: Appl. Phys. **34**, 1592 (2001).

Translated by P. Pozdeev

Technical Physics Letters, Vol. 30, No. 1, 2004, pp. 9–11. Translated from Pis'ma v Zhurnal Tekhnicheskoĭ Fiziki, Vol. 30, No. 1, 2004, pp. 21–27.

High-Power Single-Mode 1.3-μm Lasers Based on InAs/AlGaAs/GaAs Quantum Dot Heterostructures

D. A. Livshits[a,*], A. R. Kovsh[a], A. E. Zhukov[a], N. A. Maleev[a], S. S. Mikhrin[a], A. P. Vasil'ev[a], E. V. Nikitina[a], V. M. Ustinov[a], N. N. Ledentsov[a], G. Lin[b], and J. Chi[b]

[a] *Ioffe Physicotechnical Institute, Russian Academy of Sciences, St. Petersburg, 194021 Russia*
[b] *Industrial Technology Research Institute, Hsinchu, Taiwan R.O.C.*
** e-mail: daniil.livshits@mail.ioffe.ru*
Received July 7, 2003

Abstract—Single-mode lasers operating in the 1.3 μm wavelength range have been obtained with the active region based on InAs/AlGaAs/GaAs quantum dot heterostructures. A minimum threshold current of about 1.4 mA is reached, which is a record value for ridge waveguide lasers. The maximum efficiency and maximum output power in the cw lasing mode are 0.73 W/A and 120 mW, respectively. © *2004 MAIK "Nauka/Interperiodica".*

Introduction. Laser diodes operating at a wavelength of 1.3 μm are key elements for the development of high-speed metropolitan area fiber networks. The main requirements for these devices are low cost and high efficiency. It is expected that GaAs lasers developed in recent years, rather than traditional InP laser diodes, will meet these requirements. There are two principal approaches to obtaining longwave lasing in heterostructures based on GaAs substrates. The first is to use InGaAsN quantum wells with low nitrogen content [1]. The necessary wavelengths of about 1.3 μm can be also obtained using a laser structure with the active region representing self-organized InAs quantum dots (QDs) [2, 3].

The main obstacle hindering the use of InGaAsN quantum wells is the excessively threshold current density of such lasers [4]. On the other hand, a disadvantage of QD lasers is a low differential resistance that requires using long cavities for obtaining a sufficiently high output power in the ground state of a QD array. Recently [5], we demonstrated that this problem can be solved by using several QD layers in the active region. Lasers using multilayer QD arrays (containing up to ten QD layers) possess an external quantum efficiency of about 80% and an output power above 5 W for a 100-μm aperture.

Here, we report on the methods for obtaining high-power single-mode low threshold lasers operating at a wavelength of about 1.3 μm based on InAs/AlGaAs/GaAs quantum dot heterostructures.

Experimental. The separate-confinement laser heterostructures were grown by molecular beam epitaxy in a Riber-32P system. The active region comprised 2, 5, or 10 layers of InAs quantum dots, separated by 33-nm-thick GaAs spacers, in an external InGaAs quantum well. Features of the heterostructure design and epitaxial growth process are described elsewhere [5].

The heterostructures were used for the fabrication of ridge waveguide lasers with a stripe width of 2.7 or 4.5 μm. Figure 1 shows a scanning electron micrograph of a typical laser cross section. The ridge profile was formed by plasmachemical etching in a Cl_2/Ar gas mixture in a high-density plasma regime. The etching depth was monitored by laser interferometer. The process was terminated at the boundary between the upper cladding layer and the waveguide layer. The insulating layer of SiN_x was formed by plasma-enhanced chemical vapor deposition. A window in the insulating layer for the

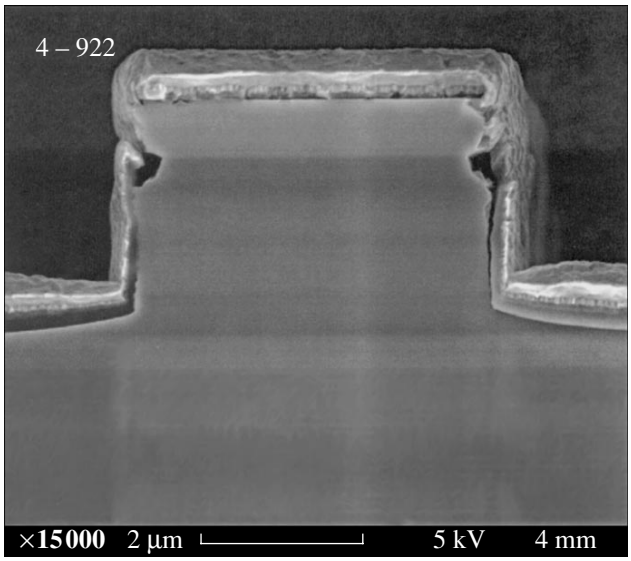

Fig. 1. A scanning electron micrograph of the cleaved cross section of a ridge waveguide laser.

1063-7850/04/3001-0009$26.00 © 2004 MAIK "Nauka/Interperiodica"

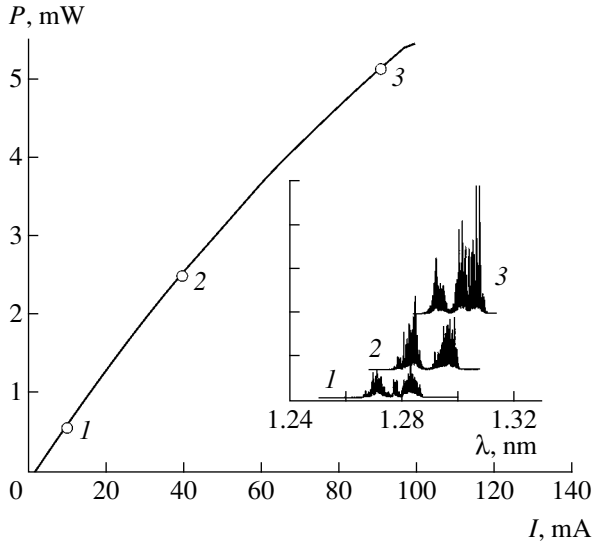

Fig. 2. The typical power–current characteristic of a laser diode with two QD layers measured in the cw regime. The inset shows the lasing spectra measured for a drive current of (*1*) 10, (*2*) 40, and (*3*) 90 mA.

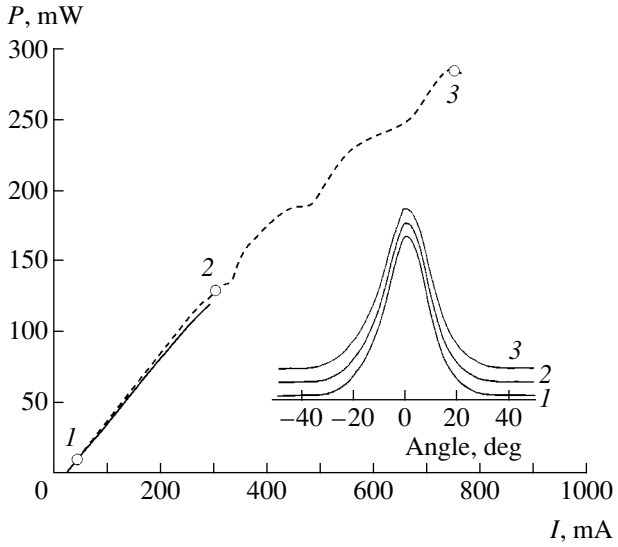

Fig. 3. The typical power–current characteristic of a laser diode with ten QD layers measured in the cw (solid curve) and pulse (dashed curve) regimes. The inset shows the far field intensity patterns measured for a drive current of (*1*) 40, (*2*) 300, and (*3*) 750 mA.

Ti/Pt/Au *p*-contact deposition was made using the self-matched mask technique. In order to provide for a reliable electric contact, the *p* side of the structure was electroplated with a 0.5-μm-thick gold film. The lasers were fixed with the *p* side up by soldering onto metallized AlN ceramic submounts with a thermal conductivity coefficient of 1.7 W/(m K) and mounted in standard TO46 cases.

Results and discussion. In order to minimize the threshold current density, we manufactured a structure with two QD layers and a cavity length of 600 μm. The front and rear cleaved mirror facets were coated with electron beam deposited high-reflection (HR) interference films comprising three and four Al_2O_3/Si bilayers, respectively. Figure 2 shows the typical output power–drive current characteristic of such a laser measured in the cw regime. A minimum threshold current reached in such laser diodes (at temperature 25°C) with a 0.6-mm-long cavity was 1.4 mA, which is a record value for ridge waveguide lasers. Lower thresholds reported in the literature were obtained only in lasers with the cavity design ensuring localization of charge carriers in the mesa region, such as quantum-well lasers with regrown mesa [6] and QD lasers with oxidized aperture [7].

Despite the HR coating on the front (output) facet, this device had an external quantum efficiency of 0.07 W/A and output power of 5.5 mW at a drive current of 100 mA. Such a low cw threshold current is explained by low internal optical losses in the heterostructure (below 1.5 cm^{-1}, as determined from the dependence of the differential efficiency on the cavity length) and by the small number of carrier states in the active region of a laser with two QD layers, determining low transparency current. The inset in Fig. 2 shows the lasing spectra measured for various drive currents (10, 40, and 90 mA). In the whole range of drive currents, lasing involves only the ground state of the QD array. In contrast, the structures with two QD layers not provided with HR coatings exhibited lasing via the first excited state (λ = 1.21 μm) simultaneously with the ground state operation (λ = 1.28 μm). This phenomenon is related to the fact that, as the drive current increases, charge carriers are accumulated in the excited states because of the finite time of the transition from excited to ground state [8].

The threshold current and, hence, the output power corresponding to the onset of lasing via excited states depend on the number of QD layers [5]. In particular, the regime of lasing via excited states was expanded toward higher output power in the structures with five and ten QD layers. Using a structure with five QD layers in the laser with a ridge stripe width of 2.7 μm, a cavity length of 1 mm, and anti-reflection (AR) and HR coatings (on the front and rear facets, respectively), we obtained an external quantum efficiency of 75%. This is a record value for single-mode QD lasers operating in the given spectral interval.

Figure 3 shows the typical output power–drive current characteristic of a laser based on a structure with ten QD layers measured in the cw (solid curve) and 2-μs pulse (dashed curve) operation regime. This laser had a 2-mm-long cavity with AR and HR coatings on the front and rear facets, respectively. The ridge waveguide width at the mesa base was 4.5 μm, which ensured stable single-mode lasing. The inset in Fig. 3 shows the far field patterns in the *p–n* junction plane measured for various drive currents (40, 300, and 750 mA). These field intensity distributions are

described by the Gauss functions with a full width at half maximum (FWHM) only slightly varying from 16.1° at the lasing threshold to 17.5° at an output power of 280 mW. The laser threshold current measured at 25°C was 19 mA, and the external quantum efficiency in the initial part of the characteristic reached 50%. In the cw lasing regime at a drive current of 300 mA, the single-mode output power was 120 mW, which is a record value for long-wavelength lasers based on QD structures [9]. As the drive current is increased further, the cw output power in the ground state exhibits saturation and the device starts operating via the excited states.

It should be noted that the output power–drive current characteristic measured in the pulse operation regime exhibits numerous reproducible breaks for currents above 300 mA. This phenomenon can be explained neither by the spatial mode competition (single-mode lasing is retained in the whole range of drive currents) nor by the jumps to lasing via excited states (such jumps take place only when the drive current exceeds 750 mA). This behavior is characteristic of all lasers based on the heterostructures with five and ten QD layers operating at a drive current density above 3 kA/cm^2. Elucidating this peculiarity requires further investigations.

Since most high-speed local fiber-optic communication lines employ lasers with an optical output power on the order of 10 mW, the working drive current in the structures with QDs can be within 30–50 mA. This interval definitely falls within a region where the power–current characteristic is stable. In this interval of drive currents, a thermal power does not exceed 50–70 mW and such a relatively low power can be dissipated in the module case without forced cooling. Thus, QD lasers can be employed without thermoelectric coolers, which significantly reduces the cost of a transmitter module.

Conclusion. We have obtained and characterized long-wavelength single-mode lasers based on InAs/AlGaAs/GaAs heterostructures with various numbers of QD layers. A laser employing two QD layers possesses a record minimum threshold current (1.4 mA) among ridge waveguide lasers. The values of the output power in the cw (120 mW) and pulse (280 mW) lasing regimes and the differential quantum efficiency (75%) reached with the proposed structures are also on a record level for single-mode QD lasers operating in the 1.3 μm wavelength range.

REFERENCES

1. B. Borchert, A. Y. Egorov, S. Illek, *et al.*, IEEE Photonics Technol. Lett. **12**, 597 (2000).
2. O. B. Schekin, G. Park, D. L. Huffaker, *et al.*, IEEE J. Quantum Electron. **36**, 472 (2000).
3. V. M. Ustinov, A. E. Zhukov, N. A. Maleev, *et al.*, J. Cryst. Growth **227**, 1155 (2001).
4. D. A. Livshits, A. Yu. Egorov, and H. Riechert, Electron. Lett. **36**, 1643 (2000).
5. A. R. Kovsh, N. A. Maleev, A. E. Zhukov, *et al.*, Electron. Lett. **38**, 1104 (2002).
6. T. R. Chen, B. Zhao, Y. H. Zhuang, and A. Yariv, Appl. Phys. Lett. **60**, 1782 (1992).
7. D. L. Huffaker, G. Park, Z. Zou, *et al.*, IEEE J. Sel. Top. Quantum Electron. **6**, 452 (2000).
8. A. E. Zhukov, A. R. Kovsh, D. A. Livshits, *et al.*, Semicond. Sci. Technol. **18** (2003) (in print).
9. S. S. Mikhrin, A. E. Zhukov, A. R. Kovsh, *et al.*, Fiz. Tekh. Poluprovodn. (St. Petersburg) **34**, 117 (2000) [Semiconductors **34**, 119 (2000)].

Translated by P. Pozdeev